

Synthetic Aperture Radar Interferometry

Paul A. Rosen, Scott Hensley, Ian R. Joughin, Fuk Li,
Søren N. Madsen, Ernesto Rodríguez, and R. M. Goldstein

Abstract

Synthetic aperture radar interferometry is an imaging technique for measuring the topography of a surface, its changes over time, and other changes in the detailed characteristics of the surface. By exploiting the phase of the coherent radar signal, interferometry has transformed radar remote sensing from a largely interpretive science to a quantitative tool, with applications in cartography, geodesy, land cover characterization, and natural hazards. This paper reviews the techniques of interferometry, systems and limitations, and applications in a rapidly growing area of science and engineering.

Keywords

SAR, Synthetic Aperture Radar, Interferometry, Geophysical Applications.

I. INTRODUCTION

This paper describes a remote sensing technique generally referred to as Interferometric Synthetic Aperture Radar (InSAR, sometimes termed IFSAR or ISAR). InSAR is the synthesis of conventional SAR techniques and interferometry techniques that have been developed over several decades in radio astronomy [1]. InSAR developments in recent years have addressed some of the limitations in conventional SAR systems and subsequently have opened entirely new application areas in earth system science studies.

SAR systems have been used extensively in the past two decades for fine resolution mapping and other remote sensing applications [2], [3], [4]. Operating at microwave frequencies, SAR systems provide unique images representing the electrical and geometrical properties of a surface in nearly all weather conditions. Since they provide their own illumination, SARs can image in daylight or at night. SAR data are increasingly applied to geophysical problems, either by themselves or in conjunction with data from other remote sensing instruments. Examples of such applications include polar ice research, land use mapping, vegetation and biomass measurements, and soil moisture mapping [3]. At present, a number of spaceborne SAR systems from several countries and space agencies are routinely generating data for such research [5].

Fig. 1. Typical imaging scenario for a SAR system, depicted here as a shuttle-borne radar. The platform carrying the SAR instrument follows a curvilinear track known as the “along-track,” or “azimuth,” direction. The radar antenna points to the side, imaging the terrain below. The distance from the aperture to a target on the surface in the look direction is known as the “range.” The “cross-track,” or range, direction is defined along by the range, and is terrain dependent.

A conventional SAR only measures the location of a target in a two-dimensional coordinate system, with one axis along the flight track (“along-track direction”) and the other axis defined as the range from the SAR to the target (“cross-track direction”), as illustrated in Fig. 1. The target locations in a SAR image are then distorted relative to a planimetric view, as illustrated in Fig. 2 [4]. For many applications, this altitude-dependent distortion adversely affects the interpretation of the imagery. The development of InSAR techniques has enabled measurement of the third dimension.

Rogers and Ingalls [7] reported the first application of interferometry to radar, removing the “north-south” ambiguity in range – range rate radar maps of the planet Venus made from Earth-based

antennas. They assumed that there were no topographic variations of the surface in resolving the ambiguity. Later, Zisk [8] could apply the same method to measure the topography of the Moon, where the radar antenna directivity was high so there was no ambiguity.

The first report of an InSAR system applied to Earth observation was by Graham [9]. He augmented a conventional airborne SAR system with an additional physical antenna displaced in the cross-track plane from the conventional SAR antenna, forming an imaging interferometer. By mixing the signals from the two antennas, the Graham interferometer recorded amplitude variations that represented the beat pattern of the relative phase of the signals. The relative phase changes with the topography of the surface as described below, so the fringe variations track the topographic contours.

To overcome the inherent difficulties of inverting amplitude fringes to obtain topography, subsequent InSAR systems were developed to record the complex amplitude and phase information digitally for each antenna. In this way, the relative phase of each image point could be reconstructed directly. The first demonstrations of such systems with an airborne platform were reported by Zebker and Goldstein [10], and with a spaceborne platform using SeaSAT data by Goldstein and colleagues [11], [12].

Today, over a dozen airborne interferometers exist throughout the world, spurred by commercialization of InSAR-derived digital elevation products and dedicated operational needs of governments, as well as by research. Interferometry using data from spaceborne SAR instruments is also enjoying widespread application, in large part because of the availability of suitable globally-acquired SAR data from the ERS-1 and ERS-2 satellites operated by the European Space Agency, JERS-1 operated by the National Space Development Agency of Japan, RadarSAT-1 operated by the Canadian Space Agency, and SIR-C/X-SAR operated by the United States, German, and Italian space agencies. This review is written in recognition of this explosion in popularity and utility of this method.

Fig. 2. The three-dimensional world is collapsed to two dimensions in conventional SAR imaging. After image formation, the radar return is resolved into an image in range-azimuth coordinates. This figure shows a profile of the terrain at constant azimuth, with the radar flight track into the page. The profile is cut by curves of constant range, spaced by the range resolution of radar, defined as $\Delta\rho = c/2\Delta f_{BW}$, where c is the speed of light and Δf_{BW} is the range bandwidth of the radar. The backscattered energy from all surface scatterers within a range resolution element contribute to the radar return for that element.

The paper is organized to first provide an overview of the concepts of InSAR (Sec. II), followed by more detailed discussions on InSAR theory, system issues, and examples of applications. Section III provides a consistent mathematical representation of InSAR principles, including issues that impact processing algorithms and phenomenology associated with InSAR data. Section IV describes the implementation approach for various types of InSAR systems with descriptions of some of the specific InSAR systems that are either operational or planned in the next few years. Section V provides a broad overview of the applications of InSAR, including topographic mapping, ocean current measurement, glacier motion detection, earthquake and hazard mapping, and vegetation estimation and classification. Finally, Section VI provides our outlook on the development and impact of InSAR in remote sensing. Appendix A defines some of the common concepts and vocabulary used in the field of synthetic aperture radar that appear in this paper. Table B in the Appendix lists the symbols used in the equations in this paper and their definitions.

We note that four recently published review papers are complementary resources available to the reader. Gens and Vangenderen [13] and Madsen and Zebker [14] cover general theory and applications. Bamler and Hartl [15] review SAR interferometry with an emphasis on signal theoretical aspects of InSAR, including mathematical imaging models, statistical properties of InSAR signals, and two-dimensional phase unwrapping. Massonnet and Feigl [16] give a comprehensive review of applications of interferometry to measuring changes of Earth's surface.

II. OVERVIEW OF INTERFEROMETRIC SAR

A. Interferometry for Topography

Figure 3 illustrates the InSAR system concept. While radar pulses are transmitted from the conventional SAR antenna, radar echoes are received by both the conventional and an additional SAR antenna. By coherently combining the signals from the two antennas, the interferometric phase difference between the received signals can be formed for each imaged point. In this scenario, the phase difference is essentially related to the geometric path length difference to the image point, which depends on the topography. With knowledge of the interferometer geometry, the phase difference can be converted into an altitude for each image point. In essence, the phase difference provides a third measurement, in addition to the along and cross track location of the image point, or “target,” to allow a reconstruction of the three-dimensional location of the targets.

The InSAR approach for topographic mapping is similar in principle to the conventional stereoscopic approach. In stereoscopy, a pair of images of the terrain are obtained from two displaced imaging positions. The ‘parallax’ obtained from the displacement allows the retrieval of topography because targets at different heights are displaced relative to each other in the two images by an amount related to their altitudes [17].

The major difference between the InSAR technique and stereoscopy is that, for InSAR, the ‘parallax’ measurements between the SAR images are obtained by measuring the phase difference between the signals received by two InSAR antennas. These phase differences can be used to determine the angle of the target relative to the baseline of the interferometric SAR directly. The accuracy of the InSAR parallax measurement is typically several mm to cm, being a fraction of the SAR wavelength whereas the parallax measurement accuracy of the stereoscopic approach is usually on the order of the resolution of the imagery (several m or more).

Typically, the post spacing of the InSAR topographic data are comparable to the fine spatial resolution of SAR imagery while the altitude measurement accuracy generally exceeds stereoscopic accuracy at comparable resolutions. The registration of the two SAR images for the interferometric measurement, the retrieval of the interferometric phase difference and subsequent conversion of the results into digital elevation models of the terrain can be highly automated, representing an intrinsic advantage of the InSAR approach. As discussed in the sections below, the performance of InSAR systems is largely understood both theoretically and experimentally. These developments have led to airborne and spaceborne InSAR systems for routine topographic mapping.

The InSAR technique just described, using two apertures on a single platform, is often called “cross-track interferometry” (XTI) in the literature. Other terms are “single-track” and “single-pass” interferometry.

Fig. 3. Interferometric SAR for topographic mapping uses two apertures separated by a “baseline” to image the surface. The phase difference between the apertures for each image point, along with the range and knowledge of the baseline, can be used to infer the precise shape of the imaging triangle to derive the topographic height of the image point.

B. Interferometry for Surface Change

Another interferometric SAR technique was advanced by Goldstein and Zebker [18] for measurement of surface motion by imaging the surface at multiple times (Fig. 4). The time separation between the imaging can be a fraction of a second to years. The multiple images can be thought of as “time-lapse” imagery. A target movement will be detected by comparing the images. Unlike conventional schemes in which motion is detected only when the targets move more than a significant fraction of the resolution of the imagery, this technique measures the phase differences of the pixels in each pair of the multiple SAR images. If the flight path and imaging geometries of all the SAR observations are

identical, any interferometric phase difference is due to changes over time of the SAR system clock, variable propagation delay, or surface motion in the direction of the radar line of sight.

In the first application of this technique described in the open literature, Goldstein and Zebker [18] augmented a conventional airborne SAR system with an additional aperture, separated along the length of the aircraft fuselage from the conventional SAR antenna. Given an antenna separation of roughly 20 m and an aircraft speed of about 200 m/s, the time between target observations made by the two antennas was about 100 ms. Over this time interval clock drift and propagation delay variations are negligible. Goldstein and Zebker showed that this system was capable of measuring tidal motions in the San Francisco bay area with an accuracy of several cm/s. This technique has been dubbed “along-track interferometry” (ATI) because of the arrangement of two antennas along the flight track on a single platform. In the ideal case, there is no cross-track separation of the apertures, and therefore no sensitivity to topography.

Fig. 4. An along track interferometer maintains a baseline separated along the flight track such that surface points are imaged by each aperture within one second. Motion of the surface over the elapsed time is recorded in the phase difference of the pixels.

C. General Interferometry: Topography and Change

ATI is merely a special case of “repeat-track interferometry” (RTI), which can be used to generate topography and motion. The orbits of several spaceborne SAR satellites have been controlled in such a way that they nearly retrace themselves after several days. Aircraft can also be controlled to accurately repeat flight paths. If the repeat flight paths result in a cross-track separation and the surface has not changed between observations, then the repeat-track observation pair can act as an interferometer for topography measurement. For spaceborne systems, RTI is usually termed “repeat-pass interferometry” in the literature.

If the flight track is repeated perfectly such that there is no cross-track separation, then there is no sensitivity to topography, and radial motions can be measured directly as with an ATI system. Since the temporal separation between the observations is typically hours to days, however, the ability to detect small radial velocities is substantially better than the ATI system described above. The first demonstration of repeat track interferometry for velocity mapping was a study of the Rutford ice stream in Antarctica, again by Goldstein and colleagues [19]. The radar aboard the ERS-1 satellite obtained several SAR images of the ice stream with near-perfect retracing so that there was no topographic signature in the interferometric phase. Goldstein *et al.* showed that measurements of the ice stream flow velocity of the order of 1 m/yr (or 3×10^{-8} m/s) can be obtained using observations separated by a few days.

Most commonly for repeat-track observations, the track of the sensor does not repeat itself exactly, so the interferometric time-separated measurements generally comprise the signature of topography and of radial motion or surface displacement. The approach for reducing these data into velocity or surface displacement by removing topography is generally referred to as “differential interferometric SAR.” In this approach (Fig. 5), at least three images are required to form two interferometric phase measurements: in the simplest case, one pair of images is assumed to contain the signature of topography only, while the other pair measures topography and change. Because the cross-track baseline of the two interferometric combinations are rarely the same, the sensitivity to topographic variation in the two generally differs. The phase differences in the topographic pair are scaled to match the frequency of variability in the topography-change pair. After scaling, the topographic phase differences are subtracted from the other, effectively removing the topography.

The first proof-of-concept experiment for spaceborne InSAR was conducted using SAR imagery obtained by the SeaSAT mission [11]. In the latter portion of that mission, the spacecraft was placed

into a near-repeat orbit every 3 days. Gabriel *et al.* [20], using data obtained in an agricultural region in California, USA, detected surface elevation changes in some of the agricultural fields of the order of several cm over approximately 1 month. By comparing the areas with the detected surface elevation changes with irrigation records, they concluded that these areas were irrigated in between the observations, causing small elevation changes from increased soil moisture. Gabriel *et al.* were actually looking for the deformation signature of a small earthquake, but the surface motion was too small to detect. Massonnet *et al.* [21] detected and validated a rather large earthquake signature using ERS-1 data several years later. Their work, along with the ice work by Goldstein *et al.* sparked a rapid growth in geodetic imaging techniques.

Fig. 5. A repeat track interferometer is similar to an along track interferometer. An aperture repeats its track and precisely measures motion of the surface between observations in the image phase difference. If the track does not repeat at exactly the same location, some topographic phase will also be present, which must be removed by the methods of differential interferometry to isolate the motion.

The differential interferometric SAR technique has since been applied to study minute terrain elevation changes caused by earthquakes and volcanoes. Several of the most important demonstrations will be described in a later section. A significant advantage of this remote sensing technique is that it provides a comprehensive view of the motion detected for the entire area affected. It is expected that this type of result will supplement ground-based measurements (*e.g.* GPS receivers), which are made at a limited number of locations.

This overview has described interferometric methods with reference to geophysical applications, and indeed the majority of published applications are in this area. However, fine resolution topographic and topographic change measurements have applications throughout the commercial, operational, and military sectors. Other applications include, for example, land subsidence monitoring for civic planning, slope stability and land-slide characterization, land-use classification and change monitoring for agricultural and military purposes, and exploration for geothermal regions. The differential InSAR technique has shown excellent promise to provide critical data for monitoring natural hazards, important to emergency management agencies at the regional and national levels.

III. THEORY

A. Interferometry for Topographic Mapping

The basic principles of interferometric radars have been described in detail by many sources, among these: [10], [22], [23], [15], [14]. The following sections comprise the main results in the principles and theory of interferometry compiled from these and other papers, in a notation and context we have found effective in tutorials. Appendix A describes aspects of SAR systems and image processing that are relevant to interferometry, including image compression, resolution, and pointing definitions.

The section begins with a geometric interpretation of the interferometric phase, from which we develop the equations of height mapping and sensitivity, and extend to motion mapping. We then move toward a signal theoretic interpretation of the phase to characterize the interferogram, which is the basic interferometric observable. From this we formulate the phase unwrapping and absolute phase determination problems. We finally move to a basic scattering theory formulation to discuss statistical properties of interferometric data and resulting phenomenology.

A.1 Basic Measurement Principles

A conventional SAR system resolves targets in the range direction by measuring the time it takes a radar pulse to propagate to the target and return to the radar. The along-track location is determined from the Doppler frequency shift that results whenever the relative velocity between the radar and target is not zero. Geometrically, this is the intersection of a sphere centered at the antenna with

radius equal to the radar range and a cone with generating axis along the velocity vector and cone angle proportional to the Doppler frequency as shown in Fig. 6. A target in the radar image could be located anywhere on the intersection locus, which is a circle in the plane formed by the radar line of sight to the target and vector pointing from the aircraft to nadir. To obtain 3-dimensional position information, an additional measurement of elevation angle is needed. Interferometry using two or more SAR images provides a means of determining this angle.

Fig. 6. Target location in an InSAR image is precisely determined by noting that the target location is the intersection of the range sphere, doppler cone and phase cone.

Interferometry can be understood conceptually by considering the signal return of elemental scatterers comprising each resolution element in a SAR image. A resolution element can be represented as a complex phasor of the coherent backscatter from the scattering elements on the ground and the propagation phase delay, as illustrated in Fig. 7. The backscatter phase delay is the net phase of the coherent sum of the contributions from all elemental scatterers in the resolution element, each with their individual backscatter phases and their differential path delays relative to a reference surface normal to the radar look direction. Radar images observed from two nearby antenna locations have resolution elements with nearly the same complex phasor return, but with a different propagation phase delay. In interferometry, the complex phasor information of one image is multiplied by the complex conjugate phasor information of the second image to form an “interferogram,” effectively canceling the common backscatter phase in each resolution element, but leaving a phase term proportional to the differential path delay. This is a geometric quantity directly related to the elevation angle of the resolution element. Ignoring the slight difference in backscatter phase in the two images treats each resolution element as a point scatterer. For the next few sections we will assume point scatterers to consider only geometry.

The sign of the propagation phase delay is set by the desire for consistency between the Doppler frequency, f_{Dop} and the phase history, $\varphi(t)$. Specifically,

$$f_{\text{Dop}} = -\frac{2}{\lambda} \frac{\partial \rho}{\partial t} \quad (1)$$

where λ is the radar wavelength in the reference frame of the transmitter, and ρ is the range. Note that as range decreases, the f_{Dop} is positive, implying a shortening of the wavelength, which is the physically expected result. With this definition, the sign convention for the phase, φ , is determined by integration, since $2\pi f = \partial\varphi/\partial t$:

$$\varphi(t) = -\frac{4\pi}{\lambda} \rho(t). \quad (2)$$

The sign of the differential path delay, or interferometric phase ϕ , is then set by the order of multiplication and conjugation in forming the interferogram. In this paper, we have elected the most common convention. Given two antennas, A_1 and A_2 as shown in Fig. 7, we take the signal from A_1 as the reference, and form the interferometric phase as

$$\phi = \varphi_1 - \varphi_2 = \frac{4\pi}{\lambda} (\rho_2 - \rho_1). \quad (3)$$

Fig. 7. The interferometric phase difference is mostly due to the propagation delay difference. The (nearly) identical coherent phase from the different scatterers inside a resolution cell (mostly) cancels during interferogram formation.

For cross-track interferometers, two modes of data collection are commonly used: single transmitter, or historically “standard,” mode where one antenna transmits and both interferometric antennas

receive; and dual transmitter, or “ping-pong,” mode where each antenna alternately transmits and receives its own echoes, as shown in Fig. 8. The measured phase differs by a factor of two depending on the mode as can be seen from Fig. 9.

Fig. 8. Illustration of standard *vs.* ping-pong mode of data collection. In standard mode, the radar transmits a signal out of one of the interferometric antennas only, and receives the echoes through both antennas A_1 and A_2 simultaneously. In “ping-pong” mode, the radar transmits alternatively out of the top and bottom antennas and receives the radar echo only through the same antenna. Repeat-track interferometers are inherently in ping-pong mode.

In standard mode, the phase difference obtained in the interferogram is given by

$$\phi_{\text{npp}} = -\frac{2\pi}{\lambda} (\rho_1 + \rho_1 - (\rho_2 + \rho_1)) = \frac{2\pi}{\lambda} (\rho_2 - \rho_1) \quad (4)$$

where ρ_i is the range from antenna A_i to a point on the surface. The notation “npp” is short for “not ping-pong”. In “ping-pong” mode, the phase is given by

$$\phi_{\text{pp}} = \frac{4\pi}{\lambda} (\rho_2 - \rho_1) \quad (5)$$

One way to interpret this result is that the ping-pong operation effectively implements an interferometric baseline that is twice as long as that in standard operation.

Fig. 9. SAR interferometry imaging geometry in the plane normal to the flight direction.

It is important to appreciate that only the principal values of the phase, modulo 2π , can be measured from the complex-valued resolution element. The total range difference between the two observation points that the phase represents in general can be many multiples of the radar wavelength or, expressed in terms of phase, many multiples of 2π . The typical approach for determining the unique phase that is directly proportional to the range difference is to first determine the relative phase between pixels via the so-called “phase-unwrapping” process. This connected phase field will then be adjusted by an overall constant multiple of 2π . The second step that determines this required multiple of 2π is referred to as “absolute phase determination.” Figure 10 shows the principal value of the phase, the unwrapped phase and absolute phase for a pixel.

Fig. 10. Phase in interferogram depicted as cycles of electromagnetic wave propagating a differential distance $\delta\rho$ for the case $p = 1$. Phase in the interferogram is initially known modulo 2π : $\phi_{\text{m}} = W(\phi_{\text{top}})$, where ϕ_{top} is the topographically induced phase and $W()$ is an operator that wraps phase values into the range $-\pi < \phi \leq \pi$. After unwrapping, relative phase measurements between all pixels in the interferogram are determined up to a constant multiple of 2π : $\phi_{\text{unw}} = \phi_{\text{m}} + 2\pi k_{\text{unw}}(\rho_{1,ij}, s_{1,ij})$, where k_{unw} is a spatially variable integer and $\rho_{1,ij}$ and $s_{1,ij}$ are pixel coordinates corresponding to the range and azimuth location of the pixels in the reference image, from A_1 in this case. Absolute phase determination is the process to determine the overall multiple of $2\pi k_{\text{abs}}$ that must be added to the phase measurements so that it is proportional to the range difference. The reconstructed phase is then $\phi_{\text{top}} = \phi_{\text{m}} + 2\pi k_{\text{unw}} + 2\pi k_{\text{abs}}$.

A.2 Interferometric Baseline and Height Reconstruction

In order to generate topographic maps or data for other geophysical applications using radar interferometry, we must relate the interferometric phase and other known or measurable parameters to the topographic height. It is also desirable to derive the sensitivity of the interferometrically determined

topographic measurements to the interferometric phase and other known parameters. In addition, interferometric observations have certain geometric constraints that preclude valid observations for all possible image geometries. These issues are quantified below.

The interferometric phase as previously defined is proportional to the range difference from two antenna locations to a point on the surface. This range difference can be expressed in terms of the vector separating the two antenna locations, called the interferometric baseline. The range and azimuth position of the sensor associated with imaging a given scatterer depends on the portion of the synthetic aperture used to process the image (see Appendix A). Therefore the interferometric baseline depends on the processing parameters, and is defined as the difference between the location of the two antenna phase center vectors at the time when a given scatterer is imaged.

The equation relating the scatterer position vector, \vec{T} , a reference position for the platform \vec{P} , and the look vector, \vec{l} , is

$$\vec{T} = \vec{P} + \vec{l} = \vec{P} + \rho \hat{l} \quad (6)$$

where ρ is the range to the scatterer and \hat{l} is the unit vector in the direction of \vec{l} . The position \vec{P} can be chosen arbitrarily, but is usually taken as the position of one of the interferometer antennas. Interferometric height reconstruction is the determination of a target's position vector from known platform ephemeris information, baseline information, and the interferometric phase. Assuming \vec{P} and ρ are known, interferometric height reconstruction amounts to the determination of the unit vector \hat{l} from the interferometric phase. Letting \vec{B} denote the baseline vector from antenna 1 to antenna 2, setting $\vec{P} = \vec{P}_1$ and defining

$$\vec{B} = \vec{P}_2 - \vec{P}_1 \quad B = |\vec{B}| \equiv \langle \vec{B}, \vec{B} \rangle^{1/2}, \quad (7)$$

we have the following expression for the interferometric phase

$$\phi = \frac{2\pi p}{\lambda} (\rho_2 - \rho_1) = \frac{2\pi p}{\lambda} (|\vec{l}_2| - |\vec{l}_1|) \quad (8)$$

$$= \frac{2\pi p}{\lambda} \rho_1 \left[\left(1 - \frac{2\langle \hat{l}_1, \vec{B} \rangle}{\rho_1} + \left(\frac{B}{\rho_1} \right)^2 \right)^{1/2} - 1 \right] \quad (9)$$

where $p = 2$ for “ping-pong” mode systems and $p = 1$ for standard mode systems, and the subscripts refer to the antenna number. This expression can be simplified assuming $B \ll \rho$ by Taylor-expanding Eq. 9 to first order to give

$$\phi \approx -\frac{2\pi p}{\lambda} \langle \hat{l}_1, \vec{B} \rangle \quad (10)$$

illustrating that the phase is approximately proportional to the projection of the baseline vector on the look direction, as illustrated in Fig. 11. This is the plane wave approximation of Zebker and Goldstein [10].

Fig. 11. When the plane wave approximation is valid the range difference is approximately the projection of the baseline vector onto a unit vector in the line of sight direction.

Specializing for the moment to the two dimensional case where the baseline lies entirely in the plane of the look vector and the nadir direction, we have $\vec{B} = (B \cos(\alpha), B \sin(\alpha))$, where α is the angle the baseline makes with respect to a reference horizontal plane. Then, Eq. 10 can be rewritten as

$$\phi = -\frac{2\pi p}{\lambda} B \sin(\theta - \alpha) \quad (11)$$

where θ is the look angle, the angle the line-of-sight vector makes with respect to nadir, shown in Fig. 9.

Fig. 12. (a) Radar brightness image of Mojave desert near Fort Irwin, California derived from SIR-C C-band (5.6 cm wavelength) repeat-track data. The image extends about 20 km in range and 50 km in azimuth. (b) Phase of the interferogram of the area showing intrinsic fringe variability. The spatial baseline of the observations is about 70 m perpendicular to the line-of-sight direction. (c) Flattened interferometric phase assuming a reference surface at zero elevation above a spherical earth.

Figure 12b shows an interferogram of the Fort Irwin, California, generated using data collected on two consecutive days of the SIR-C mission. In this figure, the image brightness represents the radar backscatter and the color represents the interferometric phase, with one cycle of color equal to a phase change of 2π radians, or one “fringe.” The rapid fringe variation in the cross track direction is mostly a result of the natural variation of the line-of-sight vector across the scene. The fringe variation in the interferogram is “flattened” by subtracting the expected phase from a surface of constant elevation. The resulting fringes follow the natural topography more closely. Letting \hat{l}_0 be a unit vector pointing to a surface of constant elevation, h_0 , the flattened phase, ϕ_{flat} , is given by

$$\phi_{\text{flat}} = -\frac{2\pi p}{\lambda} (\langle \hat{l}, \vec{B} \rangle - \langle \hat{l}_0, \vec{B} \rangle) \quad (12)$$

where

$$\hat{l}_0 = (\sin \theta_0, -\cos \theta_0) \quad (13)$$

and $\cos \theta_0$ is given by the law of cosines

$$\cos \theta_0 = \frac{\rho_0^2 + (r_e + h_p)^2 - (r_e + h_0)^2}{2(r_e + h_p)\rho_0} \quad (14)$$

assuming a spherical Earth with radius r_e and a slant range to the reference surface ρ_0 . The flattened fringes shown in Fig. 12c more closely mimic the topographic contours of a conventional map.

The intrinsic fringe frequency in the slant plane interferogram is given by

$$\frac{\partial \phi}{\partial \rho} = \frac{\partial \phi}{\partial \theta} \frac{\partial \theta}{\partial \rho} \quad (15)$$

$$= \frac{2\pi p}{\lambda} B \cos(\theta - \alpha) \cdot \frac{1}{\rho \sin \theta} \left[-\frac{\rho}{h_p + r_e} + \cos \theta + \frac{h_0 + r_e}{h_p + r_e} \frac{\sin \tau_c}{\sin(i - \tau_c)} \right] \quad (16)$$

where

$$\sin i = \frac{h_p + r_e}{h_0 + r_e} \sin \theta \quad (17)$$

and i is the local incidence angle relative to a spherical surface, h_p is the height of the platform, and τ_c is the surface slope angle in the cross track direction as defined in Fig. 9. From Eq. 16, the fringe frequency is proportional to the perpendicular component of the baseline, defined as

$$B_{\perp} \equiv B \cos(\theta - \alpha) \quad (18)$$

As B_{\perp} increases or as the local terrain slope approaches the look angle, the fringe frequency increases. Slope dependence of the fringe frequency can be observed in Fig. 12c where the fringe frequency typically increases on slopes facing toward the radar and is less on slopes facing away from the radar. Also from Eq. 16, the fringe frequency is inversely proportional to λ , thus longer wavelengths result in lower fringe frequencies. If the phase changes by 2π or more across the range resolution element, $\Delta\rho$,

the different contributions within the resolution cell do not add to a well defined phase resulting in what is commonly referred to as decorrelation of the interferometric signal. Thus, in interferometry, an important parameter is the critical baseline, defined as the perpendicular baseline at which the phase rate reaches 2π per range resolution element. From Eq. 16, the critical baseline satisfies the proportionality relationship

$$B_{\perp,\text{crit}} \propto \frac{\lambda}{\Delta\rho}. \quad (19)$$

This is a fundamental constraint for interferometric radar systems. Also, the difficulty in phase unwrapping increases (see Sec. III-E.1) as the fringe frequency approaches this critical value.

Full three dimensional height reconstruction is based on the observation that the target location is the intersection locus of three surfaces: the range sphere, Doppler cone, and phase cone described earlier. The cone angles are defined relative to the generating axes determined by the velocity vector for the Doppler cone and the baseline vector for the phase cone. (Actually the phase surface is a hyperboloid, however for most applications where the plane wave approximation is valid, the hyperboloid degenerates to a cone.) The intersection locus is the solution of the system equations

$$\begin{aligned} \rho &= |\vec{P} - \vec{T}| && \text{Range Sphere} \\ f &= 2\langle \vec{v}, \hat{l} \rangle / \lambda && \text{Doppler Cone} \\ \phi &= -2\pi p \langle \vec{B}, \hat{l} \rangle / \lambda && \text{Phase Cone} \end{aligned} \quad (20)$$

These equations appear to be non-linear, but by choosing an appropriate local coordinate basis, they can be readily solved for \hat{l} [48]. To illustrate, we let $\vec{P} = (y_0, h_p)$ be the platform position vector, and specialize to the two dimensional case where $\hat{l} = (\sin \theta, \cos \theta)$. Then from the basic height reconstruction equation Eq. 6,

$$\vec{T} = (y_0, h_p) + \rho (\sin \theta, -\cos \theta). \quad (21)$$

We have assumed that the Doppler frequency is zero in this illustration, so the Doppler Cone does not directly come into play. The range ρ is measured, and relates the platform position to the target (Range Sphere) through extension of the unit look vector \hat{l} . The look angle θ is resolved by using the Phase Cone equation, as simplified in Eq. 11, with measured interferometric phase

$$\theta = \sin^{-1} \left(\frac{-\lambda\phi}{2\pi p B} \right) + \alpha \quad (22)$$

With θ estimated, \vec{T} can be constructed.

It is immediate from the above expressions that reconstruction of the scatterer position vector depends on knowledge of the platform location, the interferometric baseline length, orientation angle and the interferometric phase. To generate accurate topographic maps, radar interferometry places stringent requirements on knowledge of the platform and baseline vectors. In the above discussion, atmospheric effects are neglected. Appendix B develops the correction for atmospheric refraction in an exponential, horizontally stratified atmosphere, showing that the bulk of the correction can be made by altering the effective speed of light through the refractive atmosphere. Refractivity fluctuation due to turbulence in the atmosphere is a minor effect for two-aperture single-track interferometers[24].

To illustrate these theoretical concepts in a more concrete way, we show in Fig. 13 a block diagram of the major steps in the processing data for topographic mapping applications, from raw data collection to generation of a digital topographic model. The description assumes simultaneous collection of the two interferometric channels; however, with minor modification, the procedure outlined applies to processing of repeat track data as well.

Fig. 13. Block diagram showing the major steps in interferometric processing to generate topographic maps. Data for each interferometric channel are processed to full resolution images using the platform motion information to compensate the data for perturbations from a straight line path. One of the complex images is resampled to overlay the other, and an interferogram is formed by cross-multiplying images, one of which is conjugated. The resulting interferogram is averaged to reduce noise. Then, the principal value of the phase for each complex sample is computed. To generate a continuous height map, the two-dimensional phase field must be unwrapped. After the unwrapping process, an absolute phase constant is determined. Subsequently, the three dimensional target location is performed with corrections applied to account for tropospheric effects. A relief map is generated in a natural coordinate system aligned with the flight path. Gridded products may include the target heights, the SAR image, a correlation map, and a height error map.

B. Sensitivity Equations and Accuracy

B.1 Sensitivity Equations and Error Model

In design tradeoff studies of InSAR systems, it is often convenient to know how interferometric performance varies with system parameters and noise characteristics. Sensitivity equations are derived by differentiating the basic interferometric height reconstruction equation Eq. 6 with respect to the parameters needed to determine \vec{P} , \hat{l} and ρ . Dependency of the quantities in the equation on the parameters typically measured by an interferometric radar is shown in Fig. 14. The sensitivity equations may be extended to include additional dependencies such as position and baseline metrology system parameters as needed for understanding a specific system's performance or for interferometric system calibration.

It is often useful to have explicit expressions for the various error sources in terms of the standard interferometric system parameters and these are found in the equations below. Differentiating Eq. 6 with respect to the interferometric phase ϕ , baseline length B , baseline orientation angle α , range ρ , and position \vec{P} , assuming that $B \ll \rho$, yields [24]

$$\begin{aligned} \Delta \vec{T} = & \Delta \vec{P} + \Delta \rho \hat{l} + \frac{\rho}{\langle \hat{B}, \hat{l} \times \hat{v} \rangle} \\ & \left[\left(\frac{-\lambda \Delta \phi}{2\pi B} - \langle \vec{l}, \frac{\Delta \vec{B}}{B} \rangle \right) \hat{l} \times \hat{v} \right. \\ & + \langle \hat{l}, \frac{\Delta \vec{v}}{v} \rangle \hat{l} \times \hat{B} \\ & \left. - \left(\hat{v} \times \hat{B} - \langle \hat{B}, \hat{l} \times \hat{v} \rangle \hat{l} \right) \frac{\Delta \lambda}{\lambda} \right] \end{aligned} \quad (23)$$

Observe from Eq. 23 that interferometric position determination error is directly proportional to platform position error, range errors lie on a vector parallel to the line of sight, \hat{l} , baseline and phase errors result in position errors which lie on a vector parallel to $\hat{l} \times \hat{v}$, and velocity errors result in position errors on a vector parallel to $\hat{l} \times \hat{B}$. Since the look vector \hat{l} in an interferometric mapping system has components both parallel and perpendicular to nadir, baseline and phase errors contribute simultaneously to planimetric and height errors. For broadside mapping geometries, where the look vector is orthogonal to the velocity vector, the velocity errors do not contribute to target position errors. Figure 14 graphically depicts the sensitivity dependencies, according to the geometry defined in Fig. 15.

To highlight the essential features of the interferometric sensitivity, we simplify the geometry to a flat earth, with the baseline in a plane perpendicular to the velocity vector. With this geometry the baseline and velocity vectors are given by

$$\vec{B} = (0, B \cos \alpha, B \sin \alpha) \quad (24)$$

Fig. 14. Sensitivity tree showing the sensitivity of target location to various parameters used in interferometric height reconstruction. A dotted line denotes a dependency that is processing or algorithm dependent. See Fig. 15 for definitions of angles.

Fig. 15. Baseline and look angle geometry as used in sensitivity formulas.

$$\vec{v} = (v, 0, 0) \quad (25)$$

where B is baseline length, α the baseline orientation angle, θ is the look angle, as shown in Fig. 9. These formulas are useful for assessing system performance or making trade studies. The full vector equation however is needed for use in system calibration.

The sensitivity of the target position to platform position in the along track direction s , cross track direction c , and vertical direction h is given by¹

$$\frac{\partial \vec{T}}{\partial P_s} = \begin{bmatrix} 1 \\ 0 \\ 0 \end{bmatrix}, \quad \frac{\partial \vec{T}}{\partial P_c} = \begin{bmatrix} 0 \\ 1 \\ 0 \end{bmatrix}, \quad \frac{\partial \vec{T}}{\partial P_h} = \begin{bmatrix} 0 \\ 0 \\ 1 \end{bmatrix} \quad (26)$$

Note that an error in the platform position merely translates the reconstructed position vector in the direction of the platform position error. Only platform position errors exhibit complete independence of target location within the scene.

The sensitivity of the target position to range errors is given by

$$\frac{\partial \vec{T}}{\partial \rho} = \begin{bmatrix} 0 \\ \sin \theta \\ -\cos \theta \end{bmatrix} = \hat{l}_{sch} \quad (27)$$

Note that range errors occur in the direction of the line-of-sight vector, \hat{l}_{sch} . Targets with small look angles have larger vertical than horizontal errors, whereas targets with look angles greater than 45° have larger cross track position errors than vertical errors.

The sensitivity of the target position to errors in the baseline length, and baseline roll angles are given by

$$\frac{\partial \vec{T}}{\partial B} = \frac{\rho}{B} \tan(\theta - \alpha) \begin{bmatrix} 0 \\ -\cos \theta \\ -\sin \theta \end{bmatrix} \quad (28)$$

and

$$\frac{\partial \vec{T}}{\partial \alpha} = \rho \begin{bmatrix} 0 \\ \cos \theta \\ \sin \theta \end{bmatrix}, \quad (29)$$

Note that the sensitivity to baseline roll errors is not a function of the baseline; it is strictly a function of the range and look angle to the target. This has the important implication for radar interferometric mapping systems that the only way to reduce sensitivity to baseline roll angle knowledge errors is to reduce the range to the scene being imaged. As there is only so much freedom to do this, this generally leads to stringent baseline angle metrology requirements for operational interferometric mapping systems.

¹Elsewhere in the literature, the (s, c, h) coordinate system is curvilinear [14]. The derivatives here, however, represent the sensitivity of the target position to errors in a local tangent plane with origin at the platform position. Additional correction terms are required to convert these derivatives to ones taken with respect to a curvilinear coordinate system. Naturally, these differences are most apparent for spaceborne systems.

In contrast, the sensitivity to baseline length errors does depend on the baseline. Since it is proportional to $\tan(\theta - \alpha)$, sensitivity is minimized if the baseline is oriented perpendicular to the look direction.

Sensitivity of the target location to the interferometric phase is given by

$$\frac{\partial \vec{T}}{\partial \phi} = \left(\frac{-\lambda \rho}{2p\pi B \cos(\theta - \alpha)} \right) \begin{bmatrix} 0 \\ \cos \theta \\ \sin \theta \end{bmatrix} \quad (30)$$

where p is 1 or 2 for single transmit or ping-pong modes. This is inversely proportional to the perpendicular component of the baseline, $B_{\perp} = B \cos(\theta - \alpha)$. Thus, maximizing the B_{\perp} will reduce sensitivity to phase errors. Viewed in another way, for a given elevation change, the phase change will be larger as B_{\perp} increases, implying increased sensitivity to topography.

A parameter often used in interferometric system analysis and characterization is the ambiguity height, the amount of height change that leads to a 2π change in interferometric phase. The ambiguity height, h_a , is given by

$$h_a = 2\pi \frac{\partial h}{\partial \phi} = \frac{\lambda \rho \sin \theta}{pB \cos(\theta - \alpha)} \quad (31)$$

where $\partial h / \partial \phi$ is obtained from the third component of Eq. 30.

Figure 16 represents an example of an interferometric SAR system for topographic mapping. Several parameters defining the performance sensitivity, and therefore calibration of the interferometer, relate directly to radar hardware observables:

- Baseline vector, \vec{B} , including length and attitude, for reduction of interferometric phase to height. This parameter translates to knowing the locations of the phase centers of the interferometer antennas.
- Total radar range, say ρ_1 , from one of the antennas to the targets, for geolocation. This parameter translates in hardware to knowing the time delays through the composite transmitter and receiver chain typically.
- Differential radar range, $\delta\rho$, between channels, for image registration in interferogram formation. This parameter translates to knowing the time delays through the receiver chains, τ_r^1 and τ_r^2 (the transmitter chain is typically the same for both channels).
- Differential phase, ϕ , between channels, for determination of the topography. This parameter translates to knowing the phase delays through the receiver chains, φ_1 and φ_2 . It requires knowing any variations in the phase centers of the antennas for all antenna pointing directions, and any variations of the phase with incidence angle that constitute the multipath signal, such as scattering of radiated energy off e.g. wings, fuselage, or radome in the aircraft case and booms or other structures on a specific platform.

Fig. 16. Definitions of interferometric parameters relating to a possible radar interferometer configuration. In this example, the transmitter path is common to both roundtrip signal paths. Therefore the transmitter phase and time delays cancel in the channel difference. The total delay is the sum of the antenna delay and the various receiver delays.

Table III-B.1 shows predicted interferometric height error sensitivities for the C-band TOPSAR [26] and Shuttle Radar Topography Mission (SRTM) [27] radar systems. Although these systems have different mapping resolutions, imaging geometries, and map accuracy requirements, there are some key similarities. Both of these systems require extremely accurate knowledge of the baseline length and orientation angle - millimeter or better knowledge for the baseline length and 10's of arc second for the baseline orientation angle. These requirements are typical of most InSAR systems, and generally

TABLE III-B.1: SENSITIVITY FOR TWO INTERFEROMETRIC SYSTEMS

Interferometric Parameter	TOPSAR			SRTM		
	Parameter Error	c Error	h Error	Parameter Error	c Error	h Error
Baseline Length	1.0 mm	0.2 m	0.3 m	3 mm	2.5 m	4.4 m
Baseline Angle	15.0 arcsec	0.9 m	1.5 m	9 arcsec	9.8 m	15.3 m
Random Phase	3.0°	0.8 m	1.4 m	8°	7.1 m	10.9 m
Range	0.5 m	0.8 m	0.5 m	3 m	2.5 m	1.6 m
Platform Position	1.0 m	1.0 m	1.0 m	1 m	1.0 m	1.0 m

necessitate either an extremely rigid and controlled baseline, a precise baseline metrology system, or both, and rigorous calibration procedures.

Phase accuracy requirements for interferometric systems typically range from 0.1 - 10 degrees. This imposes rather strict monitoring of phase changes not related to the imaging geometry in order to produce accurate topographic maps. Both the TOPSAR and SRTM system use a specially-designed calibration signal to remove radar electronically-induced phase delays between the interferometric channels.

C. Interferometry for Motion Mapping

The theory described above assumed that the imaged surface is stationary over time, or that the surface is imaged by the interferometer at a single instant. When there is motion of the surface between radar observations there is an additional contribution to the interferometric phase variation. Figure 17 shows the geometry when a surface displacement occurs between the observation at \vec{P}_1 (at time t_1) and the observation at \vec{P}_2 (at $t_2 > t_1$). In this case, \vec{l}_2 becomes

$$\vec{l}_2 = \vec{T} + \vec{D} - \vec{P}_2 = \vec{l}_1 + \vec{D} - \vec{B} \quad (32)$$

where \vec{D} is the displacement vector of the surface from t_1 to t_2 . The interferometric phase expressed in terms of this new vector is

$$\phi = \frac{4\pi}{\lambda} \left(\langle \vec{l}_1 + \vec{D} - \vec{B}, \vec{l}_1 + \vec{D} - \vec{B} \rangle^{1/2} - \rho_1 \right) \quad (33)$$

Assuming as above that $|\vec{B}|$, $|\vec{D}|$, and $|\langle \vec{B}, \vec{D} \rangle|$ are all much smaller than ρ_1 , the phase reduces to

$$\phi = \frac{4\pi}{\lambda} \left(-\langle \vec{l}_1, \vec{B} \rangle + \langle \vec{l}_1, \vec{D} \rangle \right) \quad (34)$$

Typically, for spaceborne geometries $B < 1$ km, and D is of order meters, while $\rho_1 \approx 600 - 800$ km. This justifies the usual formulation in the literature that

$$\phi_{\text{obs}} = \phi_{\text{topography}} + \phi_{\text{displacement}}. \quad (35)$$

In some applications, the displacement phase represents a nearly instantaneous translation of the surface resolution elements, *e.g.* earthquake deformation. In other cases, such as glacier motion, the displacement phase represents a motion tracked over the time between observations. Intermediate cases include slow and/or variable surface motions, such as volcanic inflation or surging glaciers.

Equations 34 and 35 highlight that the interferometer measures the projection of the displacement vector in the radar line-of-sight direction. To reconstruct the vector displacement, observations must be made from different aspect angles.

Fig. 17. Geometry of displacement interferometry. Surface element has moved in a coherent fashion between the observation made at time t_1 and the observation made at time t_2 . The displacement can be of any sort - continuous or instantaneous, steady or variable - but the detailed scatterer arrangement must be preserved in the interval for coherent observation.

The topographic phase term is not of interest for displacement mapping, and must be removed. Several techniques have been developed to do this. They all essentially derive the topographic phase from another data source, either a digital elevation model (DEM) or another set of interferometric data. The selection of a particular method for topography measurement depends heavily on the nature of the motion (steady or episodic), the imaging geometry (baselines and time separations), and the availability of data.

It is important to appreciate the increased precision of the interferometric displacement measurement relative to topographic mapping precision. Consider a discrete displacement event such as an earthquake where the surface moves by a fixed amount \vec{D} in a short time period. Neither a pair of observations acquired before the event (pair “a”), nor a pair after the event (pair “b”) would measure the displacement directly, but together would measure it through the change in topography. According to Eq. 33, and assuming the same imaging geometry for “a” and “b” without loss of generality, the phase difference between these two interferograms (that is the difference of phase differences) is

$$\phi = \phi_a - \phi_b \quad (36)$$

$$= \frac{4\pi}{\lambda} \left[\left(\langle \vec{l}_1 - \vec{B}, \vec{l}_1 - \vec{B} \rangle^{1/2} - \rho_1 \right) \quad (37)$$

$$- \left(\langle \vec{l}_1 + \vec{D} - \vec{B}, \vec{l}_1 + \vec{D} - \vec{B} \rangle^{1/2} \right. \\ \left. - \langle \vec{l}_1 + \vec{D}, \vec{l}_1 + \vec{D} \rangle^{1/2} \right) \Big] \\ = 0 \quad (38)$$

to first order, because \vec{D} appears in both the expression for \vec{l}_2 and \vec{l}_1 . The nature of the sensitivity difference inherent between Eqs. 34 and 38 can be seen in the “flattened” phase (see Eq. 12) of an interferogram, often written [25]

$$\phi = -\frac{4\pi}{\lambda} B \cos(\theta_0 - \alpha) \frac{z}{\rho_0 \sin \theta_0} + \frac{4\pi}{\lambda} \delta \rho_{\text{disp}} \quad (39)$$

where $\delta \rho$ is the surface displacement between imaging times in the radar line of sight direction, and z is the topographic height above the reference surface. In this formulation, the phase difference is far more sensitive to *changes* in topography (surface displacement) than to the topography itself. From Eq. 39, $\delta \rho = \lambda/2$ gives one cycle of phase difference, while z must change by a substantial amount, essentially ρ_0/B , to affect the same phase change. For example, for ERS, $\lambda = 5.6$ cm, $\rho_1 \approx 830$ km, and typically $B \leq 200$ m, implying $\delta \rho_{\text{disp}} = 2.8$ cm to generate one cycle of phase, $z \geq 450$ cm to have the same effect.

The time interval over which the displacement is measured must be matched to the geophysical signal of interest. For ocean currents the temporal baseline must be of the order of a fraction of a second because the surface changes quickly and the assumption that the backscatter phase is common to the two images could be violated. At the other extreme, temporal baselines of several years may be required to make accurate measurements of slow deformation processes such as interseismic strain.

D. The Signal History and Interferogram Definition

To characterize the phase from the time signals in a radar interferometer, consider the transmitted signal in channel i ($=1$ or 2) given by

$$p_i(t) = h_{t,i}(t) \exp(j2\pi f_0 t) \quad (40)$$

where $h_{t,i}$ is the encoded baseband waveform. After down-conversion to baseband, and assuming range compression as described in Appendix A, the received echo from a target is

$$s_i(t) = h_i(t - t_{di}) \exp(-j2\pi f_0 t_{di}), \quad (41)$$

where h_i is the impulse response of channel i . The time delay t_{di} encode the path delays described in the preceding equations.

To form an interferogram, the signals from the two channels must be shifted to coregister them, as the time delays t_{di} are generally different. For spaceborne systems with smooth flight tracks, usually one of the signals is taken as a reference, and the other signal is shifted to match it. The shift is often determined empirically by cross-correlating the image brightness in the two channels. For airborne systems with irregular motions, usually a common well-behaved track not necessarily on the exact flight track is used for forming the interferogram. Assuming this more general approach, to achieve the time coregistration each channel is shifted by $t_{di, \text{REF}} - t_{d0, \text{REF}}$, the delay difference between track i and the common track 0, assuming all targets lie in a reference elevation plane. It can be shown that a phase rotation proportional to this time shift applied to each channel has the effect of pre-flattening the interferogram, as is accomplished by the second term in Eq. 12.

The signal after the range shift and phase rotation is:

$$\begin{aligned} g_i(t) &= s_i(t + t_{di, \text{REF}} - t_{d0, \text{REF}}) \exp(j2\pi f_0(t_{di, \text{REF}} - t_{d0, \text{REF}})) \\ &= h_i(t + t_{di, \text{REF}} - t_{d0, \text{REF}} - t_{di}) \exp(j2\pi f_0(t_{di, \text{REF}} - t_{d0, \text{REF}} - t_{di})) \end{aligned} \quad (42)$$

Assuming identical transfer functions h_0 for the two channels, the interferometric correlation function, or interferogram, is:

$$\begin{aligned} c(t, f_0) &= g_1(t) g_2^*(t) \\ &= h_0(t - t_{d1} + t_{d1, \text{REF}} - t_{d0, \text{REF}}) h_0^*(t - t_{d2} + t_{d2, \text{REF}} - t_{d0, \text{REF}}) \\ &\quad \exp(-j2\pi f_0(t_{d1} - t_{d2} - (t_{d1, \text{REF}} - t_{d2, \text{REF}}))) \end{aligned} \quad (43)$$

Specifying channel 1 as the “master” image is consistent with the previously derived interferometric phase equations. The interferogram phase is proportional to the carrier frequency and the difference between the actual time delay differences and that assumed during the co-registration step. These time delay differences are the topographically induced range variations $t_{d1} - t_{d2} - (t_{d1, \text{REF}} - t_{d2, \text{REF}}) = (\delta\rho - \delta\rho_0)/c$, where $\delta\rho_0 = -\langle \hat{l}_0, \vec{B} \rangle$.

The standard method of interferogram formation for repeat-track spaceborne systems (as illustrated in Fig. 12a) assumes that channel 1 is the reference, and that an empirically derived range shift is applied to channel 2 only to adjust it to channel 1 with no phase rotation. The form of the interferogram would then be

$$c_{\text{spaceborne}}(t, f_0) = h_0(t - t_{d1}) h_0^*(t - t_{d2} + \Delta t_{d21}) \exp(-j2\pi f_0(t_{d1} - t_{d2})) \quad (44)$$

where Δt_{d21} is the estimated delay difference.

E. The Phase in Interferometry

E.1 Phase Unwrapping

The phase of the interferogram must be unwrapped to remove the modulo- 2π ambiguity before estimating topography or surface displacement. There are two main approaches to phase unwrapping. The first class of algorithms is based on the integration with branch cuts approach initially developed by Goldstein *et al.* [11]. A second class of algorithms is based on a least-squares (LS) fitting of the unwrapped solution to the gradients of the wrapped phase. The initial application of least-squares method to interferometric phase unwrapping was by Ghiglia and Romero [29], [30]. Fornaro *et al.* [31] have derived another method based on a Green's function formulation, which has been shown to be theoretically equivalent to the LS method [32]. Other unwrapping algorithms that do not fall into either of these categories have been introduced [33], [34], [35], [36], [37], [39], and several hybrid algorithms and new insights have arisen [40], [41], [42], [44], [46].

Branch-cut methods

A simple approach to phase unwrapping would be to form the first differences of the phase at each image point in either image dimension as an approximation to the derivative, and then integrate the result. Direct application of this approach, however, allows local errors due to phase noise to propagate, causing errors across the full SAR scene [11]. Branch-cut algorithms attempt to isolate sources of error prior to integration. The basic idea is to unwrap the phase by choosing only paths of integration that lead to self-consistent solutions [11]. The first step is to difference the phase so that differences are mapped into the interval $(-\pi, \pi]$. In performing this operation, it is assumed that the true (unwrapped) phase does not change by more than $\pm\pi$ between adjacent pixels. When this assumption is violated, either from statistical phase variations or rapid changes in the true intrinsic phase, inconsistencies are introduced that can lead to unwrapping errors.

The unwrapped solution should, to within a constant of integration, be independent of the path of integration. This implies that in the error-free case, the integral of the differenced phase about a closed path is zero. Phase inconsistencies are therefore indicated by non-zero results when the phase difference is summed around the closed paths formed by each mutually neighboring set of four pixels. These points, referred to as “residues” in the literature, are classified as either positively or negatively “charged,” depending on the sign of the sum (the sum is by convention performed in clockwise paths). Integration of the differenced phase about a closed path yields a value equal to the sum of the enclosed residues. As a result, paths of integration that encircle a net charge must be avoided. This is accomplished by connecting oppositely charged residues with branch cuts, which are lines the path of integration cannot cross. Figure 18 shows an example of a branch cut. As the figure illustrates, it is not possible to choose a path of integration that does not cross the cut, yet contains only a single residue. An interferogram may have a slight net charge, in which case the excess charge can be “neutralized” with a connection to the border of the interferogram. Once branch cuts have been selected, phase unwrapping is completed by integrating the differenced phase subject to the rule that paths of integration do not cross branch cuts.

Fig. 18. An example of a branch cut and allowable and forbidden paths of integration.

Fig. 19. Cut dependencies of unwrapped phase. a) shortest path cuts b) better choice of cuts.

The method for selection of branch cuts is the most difficult part of the design of any branch-cut based unwrapping algorithm and is the key distinguishing feature of members of this class of algorithms. In most cases the number of residues is such that evaluating the results of all possible solutions is

computationally intractable. Thus, branch cut selection algorithms typically employ heuristic methods to limit the search space to a reasonable number of potentially viable solutions [11], [40], [47].

Figure 19 shows a schematic example of a phase discontinuity and how different choices of cuts can affect the final result. In Fig. 19a, the shortest possible set of branch cuts is used to connect the residues. This choice of branch cuts forces the path of integration to cross a region of true phase shear, causing the phase in the shaded region to be unwrapped incorrectly and the discontinuity to be inaccurately located across the long vertical branch cut. Figure 19b shows a better set of branch cuts where the path of integration is restricted from crossing the phase shear. With these cuts, the phase is unwrapped correctly for the shaded region and the discontinuity across the branch cut closely matches the true discontinuity.

A commonly cited misconception regarding branch-cut algorithms is that operator intervention is needed to succeed [30][31]. Fully automated branch cuts algorithms have been used to select branch cuts for a wide variety of interferometric data from both airborne and spaceborne sensors.

Least-squares methods

An alternate set of phase unwrapping methods is based on a least squares approach. These algorithms minimize the difference between the gradients of the solution and the wrapped phase in a least-squares sense. Following the derivation of Ghiglia and Romero [30] the sum to be minimized is

$$\sum_{i=0}^{M-2} \sum_{j=0}^{N-1} \left(\phi_{i,j} - \phi_{i-1,j} - \Delta_{i,j}^x \right)^2 + \sum_{i=0}^{M-1} \sum_{j=0}^{N-2} \left(\phi_{i,j} - \phi_{i,j-1} - \Delta_{i,j}^y \right)^2 \quad (45)$$

where $\phi_{i,j}$ is the unwrapped solution corresponding to the wrapped values $\psi_{i,j}$ and

$$\Delta_{i,j}^x = W(\psi_{i,j} - \psi_{i-1,j}) \quad (46)$$

and

$$\Delta_{i,j}^y = W(\psi_{i,j} - \psi_{i,j-1}) \quad (47)$$

with the operator $W()$ wrapping values into the range $-\pi < \psi \leq \pi$ by an appropriate addition of $\pm 2\pi$. In this equation, N and M are the image dimensions.

The summation in Eq. 45 can be reworked so that for each set of indices i, j ,

$$\phi_{i+1,j} + \phi_{i-1,j} + \phi_{i,j+1} + \phi_{i,j-1} = \rho_{i,j}, \quad (48)$$

where

$$\rho_{i,j} = (\Delta_{i,j}^x - \Delta_{i-1,j}^x) - (\Delta_{i,j}^y - \Delta_{i,j-1}^y) \quad (49)$$

This equation represents a discretized version of Poisson's equation. The least-squares problem then may be formulated as the solution of a linear set of equations

$$A\phi = \rho \quad (50)$$

where A is an NM by NM sparse matrix and the vectors ϕ and ρ contain the phase values on the left and right hand sides of Eq. 49, respectively. For typical image dimensions, the matrix A is too large to obtain a solution by direct matrix inversion. A computationally fast and efficient solution, however, can be obtained using an FFT based algorithm [30].

The unweighted LS solution is sensitive to inconsistencies in the wrapped phase (i.e., residues), leading to significant errors in the unwrapped phase. A potentially more robust approach is to use a weighted LS solution. In this case, an iterative computational scheme (based on the FFT algorithm) is necessary to solve Eq. 50, leading to significant increases in computation time. Other computational techniques have been used to further improve throughput performance [41], [42].

Branch-cut vs. least-squares methods

The performance of least-squares and branch-cut algorithms differ in several important ways. Branch-cut algorithms tend to "wall-off" areas with high residue density (for example a lake in a repeat-pass interferogram where the correlation is zero) so that holes exist in the unwrapped solution. In contrast, LS algorithms provide continuous solutions even where the phase noise is high. This can be considered both a strength and a weakness of the LS approach since on one hand LS leaves no holes but on the other hand it may provide erroneous data in these areas.

Errors in a branch cut solution are always integer multiples of 2π (i.e, when the unwrapped solution is rewrapped it equals the original wrapped phase). These errors are localized in the sense that the result consists of two types of regions: those that are unwrapped correctly and those that have error that is an integer multiple of 2π . In contrast, LS algorithms yield errors that are continuous and distributed over the entire solution. Large-scale errors can be introduced during LS unwrapping. For example, unweighted LS squares solutions have been shown to be biased estimators of slope [44]. Whether slope biases are introduced for weighted LS depends on the particular implementation of the weighting scheme, and on whether steps are taken to compensate, as by iteration or initial slope removal with a low resolution DEM [45].

Phase unwrapping using branch cuts is a well established and mature method for interferometric phase unwrapping. It has been applied to a large volume of interferometric data and will be used as the algorithm for the Shuttle Radar Topography Mission data processor (see below). Unweighted LS algorithms are not sufficiently robust for most practical applications [30], [41]. While weighted LS can yield improved results, the results are highly dependent on the selection of weighting coefficients. The selection of these weights is a problem of similar complexity to that of selecting branch cuts.

Other methods

Recently, other promising methods have been developed that cannot be classified as either branch cut or least-squares methods. Costantini [38], [39] developed a method that minimizes the weighted absolute value of the gradient differences (L_1 norm) instead of the squared values as in Eq.45. Like the branch cut method, this solution differs from the wrapped phase by integer multiples of 2π , and can be roughly interpreted as a global solution for the branch cut method. The global solution is achieved by equating the problem to a minimum cost flow problem on a network, for which efficient algorithms exist. A similar solution was proposed by Flynn [37].

The possibility of using other error minimization criteria, in general the norm L_p with $0 \leq p \leq 2$ was considered by Ghiglia and Romero [43]. Xu and Cumming [34] used a region growing approach with quality measures to unwrap along paths with the highest reliability. A method utilizing a Kalman filter is described by Kramer and Loffeld [35]. Ferretti *et al.* [36] developed a solution that relies on several wrapped phase data sets of the same area to help resolve the phase ambiguities.

E.2 Absolute Phase

Successful phase unwrapping will establish the correct phase differences between neighboring pixels. The phase value required to make a geophysical measurement is that which is proportional to range delay. This phase is called the "absolute phase." Usually the unwrapped phase will differ from the absolute phase by an integer multiple of 2π , as illustrated in Fig. 10 (and possibly a calibration phase factor which we will ignore here). Assuming that the phases are unwrapped correctly, this integer is a single constant throughout a given interferometric image set. There are a number of ways to determine the absolute phase. In topographic mapping situations the elevation of a reference point in the scene might be known and given the mapping geometry, including the baseline, one can calculate the absolute phase, *e.g.* from Eqs. 21 and 22, solving for θ , then ϕ . However, in the absence of any reference, it may be desirable to determine the absolute phase from the radar data. Two methods proposed to determine the absolute phase automatically, without using reference target information

[48], [49]. The interferogram phase, defined in Eq. 43, is proportional to the carrier frequency and the difference between the actual time delay differences and that assumed during the co-registration step. Absolute phase methods exploit these relationships.

The “split-spectrum” estimation algorithm, divides the available RF-bandwidth in two or more separate subbands. A differential interferogram formed from two subbanded interferograms, with carrier frequencies f_+ and f_- , has the phase

$$\phi_{\pm}(t) = -2\pi(f_+ - f_-)(t_{d1} - t_{d2} - (t_{d1,\text{REF}} - t_{d2,\text{REF}})) \quad (51)$$

This shows that the phase of the differential interferogram is equivalent to that of an interferogram with a carrier which is the difference of the carrier frequencies of the two interferograms used. The difference $f_+ - f_-$ should be chosen such that the differential phase is always in the range $[-\pi, \pi]$, making the differential phase unambiguous. Thus, from the phase term in Eq. 43 and Eq. 51, a relationship between the original and differential interferometric phase is established:

$$\phi(t) = \phi_{\pm}(t) \frac{f_0}{f_+ - f_-} \quad (52)$$

The noise in the differential interferogram is comparable to that of the “standard” interferogram, but typically larger by a factor of two. After scaling the differential absolute phase value, the noise at the actual RF carrier phase is typically much larger than 2π . Instead, we can use that after phase unwrapping,

$$\phi_{\text{unw}}(t) = \phi(t) - n2\pi \quad (53)$$

which leads us to an estimator for the integer multiple of

$$n = \frac{1}{2\pi} \left(\phi_{\pm}(t) \frac{f_0}{f_+ - f_-} - \phi_{\text{unw}}(t) \right) \quad (54)$$

This estimate can be averaged over all points in the interferogram allowing significant noise reduction.

The “residual delay” estimation technique is based on the observation that the absolute phase is proportional to the signal delay. The basis of SAR interferometry is that the phase measurement is the most accurate measure of delay. The signal delay measured directly from the full signal (e.g. by correlation analysis or modified versions thereof) is an unambiguous determination of the delay, but to determine the channel-to-channel delay accurately, a large correlation basis is required. For such a large estimation area, however, the inherent channel signal delay difference is seldom constant because of parallax effects, and so delay estimates from direct image correlation can rarely attain the required accuracy.

The unwrapped phase can be used to mitigate this problem. As the unwrapped phase is an estimate of the channel to channel delay difference, the unwrapped phase is a measure of the spatially varying delay shift required to interpolate one image to have the same delay as the other channel. If the unwrapped phase is identical to the absolute phase, the two image delays will be identical (except for noise) after the interpolation. If on the other hand the unwrapped and the absolute phases differ by an integer number of 2π then the delay difference between the two channels will be offset by this same integer number of RF-cycles. This delay is constant throughout the image, and can thus be estimated over large image areas.

From Eqs. 43 and 53, we have:

$$\phi_{\text{unw}}(t) = -2\pi f_0(t_{d1} - t_{d2} - (t_{d1,\text{REF}} - t_{d2,\text{REF}})) + \frac{n}{f_0} \quad (55)$$

where n is unknown. Using $\phi_{\text{unw}}(t)$ we can resample and phase shift channel j :

$$\begin{aligned} g_2^S(t) &= g_2\left(t - \frac{\phi_{\text{unw}}}{-2\pi f_0}\right) \exp(j\phi_{\text{unw}}) \\ &= h_2\left(t - t_{d1} + t_{d1,\text{REF}} - t_{d0,\text{REF}} - \frac{n}{f_0}\right) \exp(j2\pi f_0(-t_{d1} + t_{d1,\text{REF}} - t_{d0,\text{REF}})) \end{aligned} \quad (56)$$

Thus if $h_1(t) = h_2(t)$ then $g_2^S(t) = g_1(t - n/f_0)$. For a given data set, after resampling and phase shifting one of the complex images, the two images will be identical with the exception of a time delay difference (= two times the range shift divided by the speed of light) which is: 1) constant over the image processed; and 2) proportional to n , the number of cycles by which the unwrapped phase differs from the absolute phase. The residual integer multiple of 2π can thus be estimated from precision delay estimation methods.

For this procedure to work the channel delay difference must be measured to hundredths or even thousandths of a pixel in range (significantly better than the ratio of λ/p to the resolution cell size) and very accurate algorithms for both interpolation and delay estimation are required. Even small errors are of concern. Thermal noise is one error source, but due to its zero mean character, it is generally not the key limitation [50]. Systematic errors are of much larger concern. For example, if the interpolations in the SAR processor are not implemented carefully, they will modify the transfer functions and introduce systematic errors in the absolute phase estimate. For the residual delay approach, even small differences in the interpolator's impulse response function will bias the correlation, which is a critical concern when accuracies on the order of a thousandth of a pixel are needed. Ideally the *system* transfer functions $h_{01}(t)$ and $h_{02}(t)$ should be identical as well. However, when the transfer functions of the two channels are different and perhaps varying across the swath, it is very difficult to estimate the absolute phase accurately. A particularly troubling error source is multipath contamination, as it will cause phase and impulse response errors which are varying over the swath [51].

Small transfer function differences will have a significant impact on the absolute phase estimated using the split-spectrum method as well, due to the very large multiplier involved ($f_0/(f_+ - f_-)$).

F. Interferometric Correlation and Phenomenology

The discussion in the preceding sections implicitly assumed that the interferometric return could be regarded as being due to a point scatterer. For most situations, this will not be the case: scattering from natural terrain is generally considered as the coherent sum of returns from many individual scatterers within any given resolution cell. This concept applies in cases where the surface is rough compared to the radar wavelength. This coherent addition of returns from many scatterers gives rise to "speckle" [52]. For cases where there are many scatterers, the coherent summation of the scatterers' responses will obey circular-Gaussian statistics [52]. The relationship between the scattered fields at the interferometric receivers after image formation is then determined by the statistics at each individual receiver, and by the complex correlation function, γ , defined as

$$\gamma = \frac{\langle g_1 g_2^* \rangle}{\sqrt{\langle |g_1|^2 \rangle \langle |g_2|^2 \rangle}} \quad (57)$$

where g_i represents the SAR return at the i antenna, and angular brackets denote averaging over the ensemble of speckle realizations. For completely coherent scatterers such as point scatterers, we have that $\gamma = 1$, while $\gamma = 0$ when the scattered fields at the antennas are independent. The magnitude of the correlation $|\gamma|$ is sometimes referred to as the "coherence" in recent literature.²

²Several authors distinguish between the "coherence" properties of fields and the correlation functions that characterize them, *e.g.* Born and Wolf [53], whereas others do not make a distinction.

The decorrelation due to speckle, or “baseline decorrelation,” can be understood in terms of the van Cittert–Zernike theorem [52]. In its traditional form, the theorem states that the correlation function of the field due to scatterers located on a plane perpendicular to the look direction is proportional to the Fourier transform of the scatterer intensity, provided the scatterers can be regarded as independent from point to point. The van Cittert–Zernike theorem was extended to the InSAR geometry [12], and was subsequently expanded to include volume scattering [23], and to include arbitrary point target responses [58]. Further contributions [59] showed that part of the decorrelation effect could be removed if slightly different radar frequencies were used for each interferometric channel, so that the component of the incident wavenumbers projected on the scatterer plane from both antennas is identical.

Physically, speckle decorrelation is due to the fact that, after removing the phase contribution from the center of the resolution cell, the phases from the scatterers located away from the center are slightly different at each antenna (see Fig. 7). The degree of decorrelation can then be estimated from the differential phase of two points located at the edges of the area obtained by projecting the resolution cell phase from each scatterer within the resolution cell, as shown in Fig. 7. Using this simple model, one can estimate that the null-to-null angular width of the correlation function, $\Delta\theta$, is given by

$$\Delta\theta \approx \frac{B_{\perp}}{\rho} \approx \frac{\lambda}{\Delta\rho_l} \quad (58)$$

where B_{\perp} is the projection of the interferometric baseline onto the direction perpendicular to the look direction, and $\Delta\rho_l$ is the projection of the ground resolution cell along the same direction, as illustrated in Fig. 20.

Fig. 20. A view of baseline decorrelation showing the effective beam pattern of a ground resolution element “radiating” to space. The mutual coherence field propagates with radiation beamwidth in elevation of $\Delta\theta \approx \lambda/\Delta\rho_l$. These quantities are defined in the figure.

This relationship can also be understood in a complementary manner if one considers the interferometric fringes due to two point sources located at the extremes of the projected resolution cell. From elementary optics [52], the nulls in the interference fringe pattern occur at an angular extent $\Delta\theta$ where the phase difference, $\phi \approx 2\pi B_{\perp} \Delta\theta / \lambda \approx 2\pi B_{\perp} \Delta\rho_l / \lambda \rho$, is a multiple of 2π . Rearranging terms, and comparing against (58), one sees that complete decorrelation occurs when the interferometric phase varies by one full cycle across the range resolution cell. In general, due to the Fourier transform relation between illuminated area and correlation distance, the longer the interferometric baseline (or, conversely, the larger the resolution cell size), the lower the correlation between the two interferometric channels.

A more general calculation results in the following expression for the interferometric field correlation:

$$\gamma = \gamma_G \gamma_Z \quad (59)$$

where γ_G is the geometric (baseline) correlation and γ_Z is the volume correlation. The geometric correlation term is present for all scattering situations, depends on the system parameters and the observation geometry, and is given by

$$\gamma_G = \frac{\int ds d\rho W_1(\rho, s) W_2^*(\rho + \delta\rho, s + \delta s) \exp[j\rho(p\kappa_\rho + 2\delta k)] \exp[j \tan \tau_s \kappa_z s]}{\int ds d\rho W_1(\rho, s) W_2^*(\rho, s)} \quad (60)$$

where $k \equiv 2\pi/\lambda$ is the wavenumber; δk represents the shift in the wavenumber corresponding to any difference in the center frequencies between the two interferometric channels; $\delta\rho$ and δs are the misregistration between the two interferometric channels in the range (ρ) and azimuth (s) directions,

respectively; $W_i(\rho, s)$ is the SAR point target response in the range and azimuth directions; and τ_s is the surface slope angle in the azimuth direction. In Eq. 60, κ_ρ and κ_z are the interferometric fringe wavenumbers in the range and vertical directions, respectively. They are given by

$$\kappa_\rho = \frac{kB_\perp}{\rho \tan(\theta - \tau_c)} \quad (61)$$

$$\kappa_z = \frac{kB_\perp \cos \tau_c}{\rho \sin(\theta - \tau_c)} = \kappa_\rho \frac{\cos \tau_c}{\cos(\theta - \tau_c)}. \quad (62)$$

Equation 60 shows explicitly the Fourier transform relation between the SAR point target response function (the equivalent of the illumination in the van Cittert-Zernicke theorem) and the geometric correlation. It follows from this equation that by applying different weightings to the SAR transmit chirp spectrum, thus modifying $W(r, s)$, one can change the shape of the correlation function to reduce phase noise. Figure 21 shows the form of γ_G , for a variety of impulse responses, as a function of the baseline normalized by the critical baseline, which the baseline for which correlation vanishes ($\rho\lambda/\Delta\rho_\perp$ from (58)).

Fig. 21. Baseline decorrelation for various point target response functions. The solid line is for standard sinc response with no weighting. The dashed, dot-dashed, dotted, and triangled lines are weightings of half-cosine, Hanning, Hamming, and optimized cosine, respectively.

As Gatelli *et al.* noted, if $2\delta k = -\kappa_\rho$, one obtains $\gamma_G = 1$ [59]. In practice, this can be done by bandpass filtering the signals from both channels so that they have slightly different center frequencies. This relationship depends on the look angle and surface slope, so that adaptive iterative processing is required in order to implement the approach exactly.

The second contribution to the correlation in Eq. 59, γ_Z , is due to volume scattering. The effect of scattering from a volume on the correlation function can be understood based on our previous discussion of the van Cittert-Zernicke theorem. From Fig. 22, one sees that the effect of a scattering layer is to increase the size projected range cell, which, according to (58), will result in a decrease of the correlation distance. If the range resolution is given by a delta function, the volume decorrelation effect can be understood as being due to the geometric decorrelation from a plane cutting through the scattering volume perpendicular to the look direction.

Fig. 22. A view of volumetric decorrelation in terms of the effective radiating ground resolution element, showing the increase in the size of the projected range resolution cell $\Delta\rho_l$ (shaded boxes) as scattering from the volume contributes within a resolution cell.

It was shown in [23] that γ_Z can be written as

$$\gamma_Z(\kappa_z) = \int dz f(z) \exp[-j\kappa_z z] \quad (63)$$

provided the scattering volume could be regarded as homogeneous in the range direction over a distance defined by the range resolution. The function $f(z)$, the “effective scatterer probability density function (pdf)”, is given by

$$f(z) = \frac{\sigma(z)}{\int dz \sigma(z)} \quad (64)$$

where $\sigma(z)$ is the effective normalized backscatter cross section per unit height. The term “effective” is used to indicate that $\sigma(z)$ is the intrinsic cross section of the medium attenuated by all propagation losses through the medium. The specific form for $\sigma(z)$ depends on the scattering medium. Models for

this term, and its use in the remote sensing of vegetation height, will be discussed in the applications section of this paper.

In repeat-pass systems, there is another source of decorrelation. Temporal decorrelation, γ_T , occurs when the surface changes between the times when the images forming an interferogram are acquired [58]. As scatterers become randomly rearranged over time, the detailed speckle patterns of the image resolution elements differ from one image to the other, so the images no longer correlate. This can often be a strong limitation on the accuracy of repeat-pass data. It can also be a means for understanding the nature of the surface.

In addition to these field correlations, thermal noise in the interferometric channels also introduces phase noise in the interferometric measurement. Since the noise is also circular-Gaussian and independent in each channel, one can show that γ_N , the correlation due to thermal noise alone, can be written as

$$\gamma_N = \frac{1}{\sqrt{1 + \text{SNR}_1^{-1}} \sqrt{1 + \text{SNR}_2^{-1}}} \quad (65)$$

where SNR_i denotes the signal-to-noise ratio for the i channel. In addition to thermal noise, which is additive, SAR returns also have other noise components, due to, for example, range and Doppler ambiguities. An expression for the decorrelation due to this source of error can only be obtained for homogeneous scenes, since, in general, the noise contribution is scene dependent. Typically for simplicity these ambiguities are treated as additive noise as part of the overall system noise floor.

In general, the full correlation will comprise contribution from all these effects:

$$\gamma = \gamma_N \gamma_G \gamma_Z \gamma_T \quad (66)$$

Figure 23 illustrates many of the decorrelation effects just described. The area imaged has a combination of steep topography, water, agriculture, and sand dunes. In Figs. 23a and 23b, the correlation is shown for images acquired one day and five months apart, respectively. Decorrelation in the Salton Sea is complete in both images. Some agricultural fields decorrelate over one day, probably due to active cultivation or watering. Some amount of decorrelation in these fields may be volumetric, depending on the crop. The mountain peaks are more highly correlated in the five-month map because the baseline of this interferometric pair is smaller by about a factor of 2 ($B = 50$ m) than the one day pair. Thus, these regions do not temporally decorrelate, but slope-induced baseline decorrelation is the dominant effect. Note that active, unvegetated dunes complete decorrelate after five months (though not in one day), but that partially vegetated dunes remain correlated. Thus the correlation can provide insight into the surface type.

Fig. 23. (a) Correlation image in radar coordinates of Algodones Dunefield, CA, measuring the sameness of the two images acquired one day apart used to form an ERS-1/2 radar interferogram. Blue color denotes low correlation, purple moderate correlation, and yellow-green high correlation. Salton Sea decorrelates because water changes from one second to the next. Some agricultural fields and dune areas decorrelate from over the one day period. Mountains decorrelate from baseline decorrelation effects on high slopes rather than temporal effects. Dunes remain well correlated in general over one day. (b) five month correlation map showing large decorrelation in the unvegetated Algodones dunes but significantly less in much of the vegetated area to the west (in box) (c) Ground photo of vegetated dune area in box.

The effect of decorrelation is the apparent increase in noise of the estimated interferometric phase. The actual dependence of the phase variance on the correlation and the number of independent estimates used to derive the phase was characterized by Monte Carlo simulation [12]. Rodríguez and Martin [23] presented the analytic expression for the Cramer-Rao bound [54] on the phase variance

$$\sigma_\phi^2 = \frac{1}{2N_L} \frac{1 - \gamma^2}{\gamma^2} \quad (67)$$

The variable N_L is the number of independent estimates used to derive the phase, and is usually referred to as the “number of looks.” The actual phase variance approaches the limit Eq. 67 as the number of looks increases, and is a reasonable approximation when the number of looks is greater than four. An exact expression for the phase variance can be obtained starting from the probability density function for the phase when $N_L = 1$, and then extended for an arbitrary number of looks [52], [55], [56], [57]. The expressions, however, are quite complicated and must be evaluated numerically in practice.

IV. INTERFEROMETRIC SAR IMPLEMENTATION

This section is intended to familiarize the reader with some of the trade-offs that must be considered in implementing an interferometer for specific applications. The discussion is not exhaustive, but treats the most common issues that face the system engineer. Several airborne and spaceborne implementations are described to illustrate the concepts.

A. *Spaceborne vs. Airborne systems*

The following is a comparison of key attributes of spaceborne and airborne interferometric SARs with regard to various applications.

A.1 Coverage

Spaceborne platforms have the advantage of global and rapid coverage and accessibility. The difference in velocity between airborne systems (≈ 200 m/s) and spaceborne platforms (> 7000 m/s) is roughly a factor of 30. A spaceborne interferometric map product that takes on the order of a month to derive would take several years in an aircraft with comparable swath. Airspace restrictions can also make aircraft operation difficult in certain parts of the world. In addition, for mapping of changes, where revisitation of globally distributed sites is crucial to understanding dynamic processes such as ice motion or volcanic deformation, regularly repeating satellite acquisitions are in general more effective.

The role of airborne sensors lies in regional mapping at fine resolution, for a host of applications such as earth sciences, urban planning, and military maneuver planning. The flexibility in scheduling airborne acquisitions, in acquiring data from a variety of orientations, and in configuring a variety of radar modes are key assets of airborne systems that will ensure their usefulness well into the future. The proliferation of airborne interferometers around the world is evidence of this.

A.2 Repeat Observation Flexibility

To construct useful temporal separation in interferometry, it is desirable to have control over the interval between repeat coverage of a site. An observing scenario may involve monitoring an area monthly, until it becomes necessary to track a rapidly evolving phenomenon such as a landslide or flood. Suddenly, an intensive campaign of observations may be needed twice a day for an extended period. This kind of flexibility in the repeat period of a platform is quite difficult to obtain with a spaceborne platform. The repeat period must be chosen to accommodate the fastest motion that must be tracked. Thus in the example above, the repeat period must be set to twice per day even though the nominal repeat observation may be one month. The separation of nadir tracks on the ground is inversely proportional to the repeat period. As the satellite ground tracks become more widely spaced it becomes more and more difficult to target all areas between tracks. In any mission design, this trade between rapid repeat observation and global accessibility must be made.

A.3 Track Repeatability

While aircraft do not suffer as much from temporal observation constraints, most airborne platforms are limited in their ability to repeat their flight track spatially with sufficient control. For a given image resolution and wavelength, the critical baseline for spaceborne platforms is longer than airborne

platforms by the ratio of their target ranges, typically a factor in the range of 20-100. For example, a radar operating at C-band at 40 MHz range bandwidth looking at 35 degrees from an airborne altitude of 10 km has a critical baseline of 65 m. Thus, the aircraft must repeat this flight track with a separation distance of fewer than about 30 m to maintain adequate interferometric correlation. The same radar configuration at an 800 km spaceborne altitude has a 5 km critical baseline.

The ability to repeat the flight track depends on both flight track knowledge and track control. GPS technology allows real-time measurement of platform positions at the meter level, but few aircraft can use this accurate information for track control automatically. The only system known to control the flight track directly with inputs from an onboard GPS unit is the Danish EMISAR. Campaigns with this system show track repeatability of better than 10 m [51].

Despite the typically longer critical baseline from space, spaceborne orbit control is complicated by several factors. Fuel conservation for long duration missions can limit the number of trajectory correction maneuvers if fine control is required. An applied maneuver requires detailed computation because drag and gravitational forces perturb the orbital elements dynamically, making the process of control somewhat iterative. The ERS satellite orbits, for example, are maintained to better than 1 km.

GPS receivers on spaceborne platforms are allowing kinematic orbit solutions accurate to several tens of meters in real-time. With this knowledge, rapid accurate trajectory corrections will become available, either on the ground or onboard. The TOPEX mission carries a prototype GPS receiver as an experiment in precision orbit determination. Recently, an autonomous orbit control experiment using this instrument was conducted. In this experiment, GPS data are sent to the ground for processing, a correction maneuver is computed (then verified by conventional means), and the correction is uplinked to the satellite. The TOPEX team has been able to "autonomously" control the orbit to within 1 km (P. Vaze, personal communication, 1998). This technique may be applied extensively to future spaceborne InSAR missions.

A.4 Motion Compensation

Motion compensation is needed in SAR processing when the platform motion deviates from the prescribed, idealized path assumed (see Fig. 24). The process of motion compensation is usually carried out in two stages. First, the data are resampled or presumed along track, usually after range compression. This stage corrects for timing offsets or velocity differences between the antennas, or simply resamples data that are regularly spaced in time to some other reference grid such as along-track distance. The second stage of motion compensation amounts to a pulse by pulse range-dependent range resampling and phase correction to align pulses over a synthetic aperture in the cross track dimension as though they were collected on an idealized flight track [4], [48], [60].

Figure 24 shows one possible stage 2 compensation strategy known as the single, or common, reference track approach. Other approaches exist [61]. Let $s_{ps}(\rho_m)$ denote the range-compressed presumed signal data for a pulse, with ρ_m the sampled range for integer m . The motion compensated signal is given by

$$s_{mc}(\tilde{\rho}) = \left[\sum_{m=1}^{F_e} f_m(\rho_m - \tilde{\rho}) s_{ps}(\rho_m) \right] e^{-j4\pi\delta\rho_{mc}/\lambda} \quad (68)$$

where f_m are the resampling filter coefficients and $\delta\rho_{mc}$ is the range component of the displacement from the reference path to the actual antenna location. This is denoted $\delta\rho_1$ and $\delta\rho_2$ in Fig. 24 for the two interferometric antennas, and is given by

$$\delta\rho_i = \vec{d}_i \cdot \hat{l}(\tilde{\rho}, h_{\text{ref}}), \quad i = 1, 2 \quad (69)$$

where \vec{d}_i is the displacement vector, \hat{l} is the unit vector pointing from the reference track to a point on the reference surface of height h_{ref} at a range $\tilde{\rho}$. There are several interesting points here:

- This definition of motion compensation in interferometric systems involves a range shift and phase rotation proportional to the range shift. This is equivalent to the interferogram formation equation Eq. 43, but here we explicitly call out the required interpolation.
- Phase corrections to the data that are applied in motion compensation must be catalogued and replaced before height reconstruction as described here.
- The range dependent phase rotation corresponds to range spectral shift needed to eliminate baseline decorrelation as described in Sec. III-F for a flat surface.

If motion compensation is not applied, processed images will be defocused and the image will exhibit distortions of scatterer positions relative to their true planimetric positions. In interferometry, this has two primary consequences: 1) the along-track variations of the scatterer locations in range imply that the two images forming an interferogram will not, in general, be well registered, leading to decorrelation and slope-dependent phase errors [48]. 2) defocused imagery implies lower SNR in the interferometric phase measurement. The resulting topographic or displacement map will have a higher level of noise. Since the adjacent image pixels of a defocused radar image are typically correlated, averaging samples to reduce noise will also not be as beneficial.

Accurate airborne interferometric SARs require motion compensation. Over the length of a synthetic aperture, flight path deviations from a linear track can be several meters. This is often the size of a range resolution cell. Platform rotations can be several milliradians. For single-pass systems, the antennas move together except for rotations of the aircraft, so the image mis-alignment problem is limited to correcting for these rotations. Compensation to a linear flight line is still required to improve focusing. In repeat-pass airborne applications, the aperture paths are independent, so misalignment can be quite severe without proper motion compensation. Here, velocity differences between repeat paths lead to a stage 1 along-track compensation correction.

Fig. 24. Single reference track motion compensation geometry illustrated for interferometry. Two wandering flight paths with motion into the paper are depicted schematically as shaded circles of possible antenna positions, with the antennas at a particular instant shown as small white circles. In the single reference track approach, an idealized reference track, chosen here as the centroid of the possible positions of Antenna 1 (but not restricted so), is defined. For an assumed reference height, a range correction for each antenna can be assigned as in the figure at each time instant to compensate for the motion.

Since scene target heights are not known *a priori*, phase errors are introduced into the motion compensation process, which in turn induce height errors. These phase errors are proportional to \vec{d}_i . The amount of height error is given by [61]

$$dh = \frac{\lambda^2 \rho \vec{d}_i \cdot \hat{l}_\perp \cos \theta}{24pL^2 B \cos(\theta - \alpha)} + \begin{cases} \frac{\lambda^2 \rho \cos \theta}{48pL^2} & \text{common track} \\ 0 & \text{dual track} \end{cases} \quad (70)$$

where \hat{l}_\perp is a vector perpendicular to \hat{l} and L is the along-track antenna length (a measure of the integration time). For example, an X-band (3 cm wavelength) system with $L = 1.5$ m, operating with $30^\circ < \theta < 60^\circ$ at an altitude of 10,000 m, and with $|d| = 5$ m would have height errors of 1 cm with parallel track compensation and 2.5 m with the common track approach. On the other hand, P-band (75 cm wavelength) system with similar operating parameters would have several orders of magnitude worse performance. Thus, there is often a desire to minimize $|d|$.

A.5 Propagation Effects

The atmosphere and ionosphere introduce propagation phase and group delays to the SAR signal. Airborne InSAR platforms travel below the ionosphere so they are insensitive to ionospheric effects. Spaceborne platforms travel in or above the ionosphere. Both airborne and spaceborne InSARs are effected by the dry and wet components of the troposphere.

Signals from single-track InSAR antennas traverse basically the same propagation path, as described previously. The common range delay comprises the bulk of the range error introduced. There is an additional small differential phase correction arising from aperture separation. For the troposphere, both terms introduce sub-meter level errors in reconstructed topography (see App. B). For the spaceborne systems with an ionospheric contribution, there may be a sufficiently large random component to the phase to cause image defocussing, degrading performance in that way.

In repeat-track systems, the propagation effects can be more severe. The refractive indices of the atmosphere and ionosphere are not homogeneous in space or time. For a spaceborne SAR, the path delays can be very large, depending on the frequency of the radar (e.g. greater than 50 m ionospheric path delay at L-band), and can be quite substantial in the differenced phase that comprises the interferogram (many cm differential tropospheric delay, and meter-level ionospheric contributions at low frequencies). These effects in repeat-track interferograms were first identified by Massonnet *et al.* [21] and later by others [62], [63], [64], [25], [65]. Ionospheric delays are dispersive, so frequency-diverse measurements can potentially help mitigate the effect, as with two-frequency GPS systems. Tropospheric delays are non-dispersive, and mimic topographic or surface displacement effects. There is no means of removing them without supplementary data. Schemes for distinguishing tropospheric effects from other effects have been proposed [63], and of averaging interferograms to reduce atmospheric noise have been introduced [65], [66], but no systematic correction approach currently exists.

PLATFORM INTERFEROMETRIC CHARACTERISTICS

CHARACTERISTIC	SPACEBORNE	AIRBORNE
Coverage	Global	Regional
Fine Resolution	Costly	Affordable
Repeat Flexibility	Difficult	Natural
Track Repeatability	Difficult/Costly	Difficult/Costly
Motion Compensation	Benign	Necessary
Atmospheric Propagation Effects		
Two-Aperture	Benign	Benign
Repeat Track	Problematic	Problematic
Ionospheric Propagation Effects		Not Applicable
Two-Aperture	Benign [†]	
Repeat Track	Problematic	
Multi-frequency	Helpful	
Frequency Selection	Application dependent (see text)	

[†] Image defocussing may occur at low frequencies.

A.6 Frequency selection for interferometry

The choice of frequency of an InSAR is usually determined by the electromagnetic phenomena of interest. Electromagnetic energy scatters most strongly from objects matched roughly to the size of the wavelength. Therefore for the varied terrain characteristics on Earth, including leaves high above the soil surface, woody vegetation, very rough lava surfaces, smooth lakes with capillary waves, etc., no single wavelength is able to satisfy all observing desires.

International regulations on frequency allocations also can restrict the choice of frequency. If a particularly wide bandwidth is needed for fine resolution mapping, certain frequency bands may be difficult to use. Other practical matters also determine the frequency, including available transmitter power, allowable antenna size, and cost.

For topographic mapping, where temporal decorrelation is negligible, frequencies can be chosen to image the topography near a desired canopy height. Generally, higher frequencies interact with the

leafy crowns and smaller branches strongly, so the inferred interferometric height is near the top of the vegetation canopy. Lower frequencies propagate through the leafy crowns of trees and scatter from larger structures such as branches or ground-trunk junctures, so the inferred height more closely follows the soil surface. This is illustrated in Fig. 25, where the difference in inferred height between C- and L-band TOPSAR data is plotted in image and profile format.

Fig. 25. a) Image of height difference between C- and L-band in Iron Mountain, California. b) Profiles as indicated going from bare fields to forested regions.

For repeat pass interferometry, the frequency selection considerations are complicated. For ice and other relatively smooth surfaces, a shorter wavelength is usually desired because the signal level is generally higher. However, shorter wavelengths tend to interact with vegetation and other small scatterers, which have a greater tendency for movement and changes between observations [25].

B. Airborne Interferometric SAR Systems

Airborne Interferometric SAR systems have been implemented with single-pass across-track and along-track interferometric capabilities as well as for repeat-pass interferometry. The technology for airborne interferometric systems is in most respects identical to the technology applied in standard non-interferometric SAR systems. The needs for accurate frequency and phase tracking and stability of the channels combined interferometrically are largely identical to the requirements for high-performance image formation in any SAR system combined with the channel tracking required of *e.g.* polarimetric SAR systems.

Accurate motion and attitude measurements are of key importance in airborne InSAR applications. To avoid significant decorrelation, the two images forming an interferogram must be co-registered with errors that are no more than a small fraction of the resolution cell size. This is generally difficult to achieve in aircraft repeat-pass situations with long flight paths. In the single-pass situation a significant fraction of the motion will be common to both antennas, which reduces motion compensation requirements significantly. To determine the location of the individual image points in across-track InSAR systems, both the aircraft location and the baseline orientation must be known with great accuracy. Today Global Positioning Systems (GPS) operated in kinematic modes can provide absolute platform locations with decimeter accuracy, and high-performance inertial navigation systems (INS) can measure high-frequency motion required for motion compensation. A significant advance in the critical determination of the baseline has been made possible by tightly coupling the INS and GPS. Absolute angle determination with an accuracy of approximately a few thousandths of a degree is off-the-shelf technology today.

In addition to the baseline orientation, the baseline length needs to be known. Most single-pass systems developed to date utilize antennas rigidly mounted on the aircraft fuselage. In the recent development of the IFSARE system [67], two antennas were mounted at the ends of an invar frame. Requiring a rigid and stable frame for a two antenna system will, however, severely limit the baseline that can be implemented on an aircraft system. This problem is especially important when a low frequency single-pass interferometer is required. GeoSAR, a system presently being developed by JPL includes a low-frequency interferometer centered at 350 MHz. To achieve a sufficiently long baseline on the Gulfstream G-2 platform, the antennas are mounted in wing tip-tanks. It is expected that, due to the motion of the wings during flight, the baseline is constantly varying. To reduce the collected SAR data to elevation maps the dynamically varying baseline is measured with a laser-based metrology system, which determines the baseline with sub-millimeter accuracy.

For multiple pass airborne systems to be useful it is important that the flight pass geometry be controlled with precision. Typically, baselines in the range of 10 to 100 m are desired, and it is also important that the baselines are parallel. Standard flight management systems do not support such

accuracies. This was first demonstrated and validated with the Canadian Centre for Remote Sensing airborne C-band radar [60]. One system which has been specifically modified to support aircraft repeat pass interferometry is the Danish EMISAR system, which is operated on a Royal Danish Air Force Gulfstream G-3. In this system the radar controls the flight-path via the aircraft's Instrument Landing System (ILS) interface. Using P-code GPS as the primary position source, this systems allows a desired flight-path to be flown with an accuracy of typically 10 m or better.

C. Spaceborne Interferometric SAR Experiments

As mentioned in the Introduction, several proof-of-concept demonstration experiments of spaceborne interferometric SAR were performed using the repeat-track approach. Li and Goldstein first reported such an experiment using the SEASAT SAR system. While this approach does suffer from the uncertainties due to changes in the surface, and propagation delay effects between the observations and the difficulties of obtaining baseline determination results with precision required for topography mapping, it clearly has the advantage that only one SAR system need to be operating at a time. To demonstrate the capability of this approach on a global scale, the European Space Agency has operated the ERS-1 and ERS-2 satellites in a so-called "tandem mission" approach. The two spacecraft obtained SAR measurements for a significant fraction of the earth's surface with measurements from one spacecraft 1 day after those from the other, with the two spacecraft in a nearly repeat ground track orbital configuration. The 1 day separation in the observations was chosen to minimize the changes mentioned above. A report with examples of the interferometric SAR measurements has been issued [68]. The detailed quantitative evaluation of this data set has yet to be carried out. However, from some of the preliminary results, one can observe temporal decorrelation in certain regions of the world, especially in heavily vegetated areas, even with the relatively short time separation of 1 day. In areas where such temporal decorrelation is not significant, it is important to perform an assessment of the quantitative accuracy of the topography data which can be generated with this extensive data set.

To avoid some of the limitations of the repeat-track interferometric SAR experiments, the National Space and Aeronautic Administration, in conjunction with the National Imagery and Mapping Agency, of the US are developing a Shuttle Radar Topography Mission (SRTM). The payload of this mission is based on the SIR-C/X-SAR system which was flown on the shuttle twice in 1994 [69]. This system is currently being augmented by an additional set of C- and X-band antennas which will be deployed by an extendible mast from the shuttle once the system is in orbit. Figure 26 shows the deployed system configuration. The SIR-C/X-SAR radar system inside the shuttle bay and the radar antennas and electronics systems attached to the end of the deployed mast will act as an interferometric SAR system. The length of the mast after deployment, which corresponds approximately to the interferometric SAR baseline, is about 60 meters. The goal of SRTM is to completely map the topography of the global land mass which is accessible from the shuttle orbit configuration (approximately covering 56 degrees South to 60 degrees North) in an 11-day shuttle mission. The C-band system will operate in a ScanSAR mode much as the Magellan Venus radar mapper, but interferometrically for SRTM [70] (see also [71]), obtaining topographic data over an instantaneous swath of about 225 Km. The radar system is based on the SIR-C system with modifications to allow data captured by both interferometric antennas and with simultaneous operation of both a horizontally polarized antenna beam and a vertically polarized antenna beams. By operating the two antenna beams concurrently, it increases the data accuracy and coverage. By combining the data from both ascending and descending orbits, the topography data with a post spacing of about 30 m data expected to have an absolute height measurement accuracy of about 10-15 meters.

A key feature of SRTM is an onboard metrology system to determine the baseline length and orientation between the antenna inside the shuttle bay and the antenna at the tip of the deployed mast. This metrology system is designed to obtain the baseline measurements with accuracies which can meet the absolute topography measurement requirements listed above. As with the two previous

Fig. 26. The Shuttle Radar Topography Mission flight system configuration. The SIR-C/X-SAR L, C, and X-band antennas reside in the shuttle's cargo bay. The C and X band radar systems are augmented by receive-only antennas deployed at the end of a 60 m long boom. Interferometric baseline length and attitude measurement devices are mounted on a plate attached to the main L-band antenna structure. During mapping operations, the shuttle is oriented so that the boom is 45 degrees from the horizontal.

flights, the data collected in the mission are stored on onboard tape recorders and upon landing, the more than 100 tapes of SAR data would then be transferred to a data processing system for global topography generation. It is expected that the data processing will take about 1 year to generate the final topography maps. The X-SAR system will also operate in conjunction with the additional X-Band antenna as an interferometric SAR. The instantaneous swath of the X-band system is about 55 Km. While in some areas of the globe, the X-band system will not provide complete coverage, it is expected that the resolution and accuracy of the topography data obtained will be better than those obtained with the C-band system. The results from both systems can be used to enhance the accuracy and/or coverage of the topography results and to study the effects of vegetation on the topography measurements across the two frequencies. At present, this mission is planned to be launched in January, 2000.

The use of spaceborne SAR data for repeat track interferometric surface deformation studies is becoming widespread in the geophysical community [16]. While this approach has uncertainties caused by path delay variability in the atmosphere or ionosphere, it provides the truly unique capability to map small topography changes over large areas. ERS-1 and ERS-2 data are currently routinely used by researchers to conduct specific regional studies. RADARSAT has been shown to be useful for interferometric studies, particularly using its fine beam mode, but much of the data is limited by relatively large baselines. JERS [5] also has been used to image several important deforming areas. We expect that in the near future, repeat pass interferometry will be possible on a more operational basis using a SAR system dedicated for this purpose.

V. APPLICATIONS

A. Topographic mapping

Radar interferometry is expanding the field of topographic mapping [72], [73], [74], [75], [76], [77], [51], [78], [79], [80]. Airborne optical cameras continue to generate extremely fine resolution (often sub-meter) imagery without the troublesome layover and shadow problems of radar. However, radar interferometers are proving to be a cost-effective method for wide area, rapid mapping applications, and do not require extensive hand-editing and tiepointing. Additionally, these systems can be operated at night in congested air-traffic corridors that are often difficult to image photogrammetrically, and at high altitudes in tropical regions that are often cloud-covered.

A.1 Topographic Strip Mapping

Typical strip-mode imaging radars generate data on long paths with swaths between 6-20 km for airborne systems and 80-100 km for spaceborne systems. These strip digital elevation models can be used without further processing to great advantage. Figure 27 shows a digital elevation model (DEM) of Mount St. Helens imaged by the NASA/JPL TOPSAR C-band interferometer in 1992, years after the eruption that blew away a large part of the mountain (prominently displayed in the figure), and destroyed much of the area. This strip map was generated automatically with an operational InSAR processor. Such rapidly generated topographic data can be used to assess the amount of damage to an area by measuring the change in volume of the mountain from before to after the eruption (assuming a DEM is available before the eruption).

Another example of a strip DEM, generated by the EMISAR system of Denmark is shown in Fig. 28.

Fig. 27. DEM of Mount Saint Helens generated in 1992 with the TOPSAR C-band interferometer. Area covered is roughly 6 km across track by 20 km along track.

DEMs such as these are providing the first detailed topographic data base for the polar regions. Because image contrast is low in snow-covered regions, optical stereo mapping can encounter difficulties. A radar interferometer, on the other hand, relies on the same arrangement of the scatterers that comprise the natural imaging surface, and so is quite successful in these regions. However, since radar signals penetrate dry snow and ice readily, the imaged surface does not always lie at the snow-air interface.

Fig. 28. DEM of Askja, Northern volcanic zone, Iceland derived from the C-band EMISAR topographic mapping system. The color variation in the image is derived from L-band EMISAR polarimetry.

Slope estimates such as illustrated in Fig. 29 are useful for hydrological studies and slope hazard analysis. Special care must be taken in computing the slopes from interferometric DEMs because the point-to-point height noise can be comparable to the post spacing. Studies have shown that when this is taken into account, radar-derived DEMs improve classification of areas of landslide-induced seismic risk [80].

Fig. 29. Height (above) and slope (below) maps of Mount Sonoma, CA. This information has been used to assess the risk of earthquake damage induced by landslides. Processing courtesy E. Chapin, JPL.

Figure 30 illustrates a continental scale topographic strip map. This DEM was generated from the SIR-C L-band system, during the SIR-C/X-SAR mission phase when the Shuttle was operating as a repeat-track interferometer. While the accuracy of repeat-track DEMs is limited by propagation path delay artifacts, this figure illustrates the feasibility of spaceborne global-scale topographic mapping. Figures 31 and 32 illustrate topographic products from ERS and JERS repeat-track interferometry.

Fig. 30. Strip of Topography generated from the SIR-C L-band radar data by repeat track interferometry. The DEM extends from the Oregon/California border through California to Mexico, roughly 1600 km.

A.2 Topographic Mosaics

For many wide-area mapping applications, strip DEMs provide insufficient coverage, so it is often necessary to combine, or “mosaic,” strips of data together. In addition to increasing contiguously mapped area, the mosaicking process can enhance the individual strips by filling in gaps due to layover or shadow present in one strip but not in an overlapping strip.

The accuracy of the mosaic and the ease with which it is generated rely on the initial strip accuracies, available ground control, and the mosaicking strategy. Traditional radar mosaicking methods are two-dimensional, assuming no height information. For radar-derived DEMs, a mosaicking scheme that allows for distortions in three dimensions described by an affine transformation, including scale, skew, rotation, and translation, is usually necessary to adjust all data sets to a limited set of ground control points. If the interferometric results are sufficiently accurate to begin with, such as is planned for the Shuttle Radar Topography Mission, mosaicking the data involves interpolating data sets contributing to an area to a common grid and performing an average weighted by the height noise variance.

Figure 33 shows a mosaic of NASA/JPL TOPSAR C-band data acquired over Long Valley, California. The mosaic is posted at 10 m with a spatial resolution of 15 m, and representing the most accurate DEM available of this region. The height accuracy is 3-4 m. Long Valley is volcanically

Fig. 31. DEM of Mount Etna, Italy generated by ERS repeat track interferometry. Actually 10 images were combined to make this DEM.

Fig. 32. DEM of Mount Unzen, Japan generated by JERS repeat track interferometry.

active, and is an area of intense survey and interest. This mosaic is both a reference to track future large scale changes in the shape of the caldera, and a reference with which to generate synthetic fringes for deformation studies.

Fig. 33. Long Valley mosaic of TOPSAR C-band interferometric data. Processing courtesy E. Chapin, JPL.

A.3 Accuracy Assessments

One of the most important aspects of interferometry is in the assessment of DEM errors. Accuracy can be defined in both an absolute and relative sense. The absolute error of a DEM can be defined as the root-mean-square of the difference between the measured DEM and a noise-free reference DEM.

$$\sigma_{h,abs} = \sqrt{\frac{1}{N_{\text{"DEM"}}} \sum_{\text{"DEM"}} (z - z_{\text{ref}})^2} \quad (71)$$

The summation is taken over the DEM extent of interest ($N_{\text{"DEM"}}$ points), so the error can be dependent on the size of the DEM, especially if systematic errors in system parameters are present. For example, an error in the assumed baseline tilt angle can induce a cross track slope error, causing the absolute error to change across the swath.

The relative error can be defined as the standard deviation of the height relative to a noise-free reference DEM.

$$\sigma_{h,rel} = \sqrt{\frac{1}{N_{\text{"box"}}} \sum_{\text{"box"}} (z - z_{\text{ref}} - \langle z - z_{\text{ref}} \rangle)^2} \quad (72)$$

Note that this definition of the relative error matches the locally scaled interferometric phase noise, given by

$$\sigma_h = \frac{\partial T_h}{\partial \phi} \sigma_\phi \quad (73)$$

where σ_ϕ in the limit of many looks is given by Eq. 67, when the summation box size is sufficiently small. As the area size increases other systematic effects enter into the relative error estimate. Other definitions of relative height error are possible, specifically designed to blend the statistical point-to-point error and systematic error components over larger areas. In this paper, we exclusively use Eq. 72.

Figure 34 illustrates one of the first comparisons of radar data to a reference DEM [26]. The difference between the TOPSAR C-band data and that produced photogrammetrically at finer resolution and accuracy by the Army Topographic Engineering Center (TEC) shows a relative height accuracy of 2.2 m over the TEC DEM. No absolute accuracy assessment was made, and the two DEMs were pre-registered using correlation techniques.

Figure 35 compares a SIR-C repeat-pass spaceborne-derived DEM to a TOPSAR mosaic. Errors in this scene are a combination of statistical phase noise-induced height errors, and those due to variability of the tropospheric water vapor through the scene between passes. In fact the major contribution to the 8 m height standard deviation attained for this region (computed using Eq. 72 over the entire

Fig. 34. Difference image between TOPSAR C-band derived DEM and a TEC photogrammetrically-generated reference DEM.

scene) was likely to be caused by water vapor contamination. This contrasts with the predicted 2-3 m relative height error obtained from Eq. 73.

Fig. 35. Difference image between SIR-C C-band derived DEM and a TOPSAR mosaic used as a reference DEM.

Figure 36 illustrates an approach to DEM accuracy assessment using kinematic GPS data. A GPS receiver mounted on a vehicle drove along a radar-identifiable road within the DEM. The trace of the GPS points was cross-correlated with the TOPSAR image to register the kinematic data to the DEM. Measured and predicted relative height errors are shown in the figure [81]. A similar approach is planned for assessing the absolute errors of the SRTM global DEM, using kinematic surveys of several thousand km around the world.

Fig. 36. Illustration of the use of kinematic GPS surveys in determining the absolute and relative error of a radar-derived DEM. Curve shows the standard deviation of the radar height relative to the GPS, and its predicted value. Statistical height error estimates derived from the correlation track the measured local statistical height errors extremely well.

B. Crustal Dynamics Applications

Differential Interferometry has generated excitement in the Earth science community in applications to the study of fault mechanics, long period seismology, and volcanic processes. The surface displacements measured by differential interferometry are uniquely synoptic, capturing subtle features of change on the Earth that are distributed over wide areas. There is a growing literature on the subject, which recently received a comprehensive review [16].

Gabriel *et al.* first demonstrated the method showed centimetric swelling of irrigated fields in Imperial Valley, California [20], using data acquired by the L-band SAR aboard SEASAT compared to ground watering models. This work illustrated the power of the method and predicted many of the applications that have developed since. It did not receive much attention, however, until the ERS C-band SAR captured the displacement field of the Landers M=7.2 earthquake of 1992. The broad and intricate fringe patterns of this large earthquake representing the net motion of the Earth's surface from before to after the earthquake graced the cover of *Nature* [21]. Massonnet and colleagues in this paper compared for the first time the InSAR measurements to independent geodetic data and elastic deformation models, obtaining centimetric agreement and setting the stage for rapid expansion of applications of the method. Since the *Nature* article, differential interferometry has been applied to coseismic [82], [83], [84], [86], [85], [87], [88], [89], [90], [91], postseismic [93], [92] and aseismic tectonic events [94], volcanic deflation and uplift [95], [25], [96], [97], [98], [66], [99], ground subsidence and uplift from fluid pumping or geothermal activity [100], [101], [102], landslide and local motion tracking [103], [104], [105], and effects of sea-floor spreading [106], [107]. The most important contributions by differential interferometry lie in areas where conventional geodetic measurements are limited. Associated with surface deformation, the correlation measurements have been used to characterize zones where surface disruption was too great for interferometry to produce a meaningful displacement estimate [108]. In addition to demonstration of science possibilities, the relatively large volume of data acquired by ERS-1, ERS-2, JERS-1, SIR-C/X-SAR, and RADARSAT has allowed for a fairly complete assessment of interferometric potential for these applications.

Coseismic displacements, i.e. those due to the main shock of an earthquake, are generally well understood mechanically in the far field away from the faults by seismologists. The far-field signature

of the Landers coseismic displacements mapped by ERS matched well with a model calculation based on elastic deformation of multiple faceted plate dislocations embedded in an infinite half space [21]. The GPS network at Landers was dense enough to capture this far field pattern, so in that sense the radar measurements were not essential to understanding the coseismic signature of the earthquake. However, the radar data showed more than simply the far-field displacements. What appears to be severe cracking of the surface into tilted facets was reported by Peltzer *et al.* [84] and Zebker *et al.* [82]. The surface properties of these tilted features remained intact spanning the deformation event. Thus their fringe pattern changed relative to their surroundings, but they remained correlated. Peltzer explained the tilted patches near the main Landers ruptures as due to shear rotation of the sideward slipping plates, or grinding of the surface at the plate interface. The cracked area farther from the rupture zone [82], also seen in interferometrically derived strain maps [91], has not been explained in terms of a detailed model of deformation.

The M=6.3 Eureka Valley, CA Earthquake in 1993 is an example of an application of interferometry to a locally uninstrumented site where important science insight can be derived. Two groups have studied this earthquake, each taking a different approach. Peltzer and Rosen [85] chose to utilize all available data to construct a geophysically consistent model that explained all the observations. Those observations included the differential interferogram, the seismic record, which included an estimate of fault plane orientation and depth of the slip, field observations, and geologic context provided by fault maps of eastern California. The seismic record predicted a fault plane orientation relative to North, known as “strike”, that was aligned with faulting history for normal faults (i.e. faults whose motion is principally due to separation of two crustal regions) in the area. Without further data, no further insight into the fault mechanism would be possible. However, Fig. 37 shows that the NNW orientation of the subsidence ellipse measured in the interferogram is not consistent with the simple strike mechanism oriented NNE according to the seismic record. Peltzer resolved the conflict by allowing for a spatially variable distribution of slip on the fault plane, originating at depth to the north and rising on the fault plane to break the surface in the south. Fresh, small surface breaks in the south were observed in the field.

Fig. 37. Subsidence caused to an M=6.3 earthquake along a normal fault in Eureka Valley, California imaged interferometrically by ERS-1. The interferometric signature combined with the seismic record suggested an interpretation of variable slip along the fault. Figure courtesy of Gilles Peltzer, JPL.

Massonnet and Feigl [63] chose to invert the Eureka Valley radar measurements unconstrained by the seismic record, and with a single uniformly slipping fault model. The inferred model did indeed match the observations well, predicting a shallow depth and an orientation of slip that was different from the seismic record but within expected error bounds. These authors argue that the surface breaks may be the result of shallow aftershocks. The different solutions found by the two approaches highlight that despite the non-uniqueness of surface geodetic measurements, the radar data contribute strongly to any interpretation in an area poor in *in situ* geodetic measurements. Much of the world falls in this category.

Postseismic activity following an earthquake is measured conventionally by seismicity and displacement fields inferred from sparse geodetic measurements. The postseismic signature at Landers was studied by two groups using interferometry [93], [92]. Peltzer *et al.* [93] formed differential interferograms over a broad area at Landers, capturing the continued slip of the fault in the same characteristic pattern as the coseismic signal, as well as localized but strong deformation patterns where the Landers fault system was disjoint. Peltzer interpreted these signals, which decreased in a predictable way with time from the coseismic event, as due to pore fluid transfer in regions that had either been compressed or rarefied by the sheer motion on disjoint faults. Material compressed in the earthquake has a fluid surfeit compared to its surrounding immediately after the event, so fluids tend to diffuse outward from

the compressed region in the postseismic period. Conversely, at pull-apart regions, a fluid deficit is compensated postseismically by transfer into the region. Thus the compressed region deflates, and the pull-apart inflates, as observed.

Fig. 38. Illustration of postseismic deformation following the M=7.2 Landers earthquake in 1992. In addition to the deformation features described in the text that are well-modeled by poro-elastic flow in the pull aparts, several other deformation processes can be seen. Figure courtesy of Gilles Peltzer, JPL.

GPS measurements of postseismic activity at Landers were too sparse to detect these local signals, and seismometers cannot measure slow deformation of this nature. This is prime example of geophysical insight into the nature of lubrication at strike-slip faults that eluded conventional measurement methods.

Aseismic displacements, i.e. slips along faults that do not generate detectable seismic waves, have been measured on numerous occasions in the Landers area, and elsewhere in the Southern California San Andreas shear zone. Sharp displacement discontinuities in interferograms indicate shallow creep signatures along such faults (Fig. 39). Creeping faults may be relieving stress in the region, and understanding their time evolution is important to understanding seismic risk.

Another location where aseismic slip has been measured is along the San Andreas fault. At Parkfield, California, a segment of the San Andreas Fault is slipping all the way to the surface, moving at the rate at which the North American and Pacific tectonic plates themselves move. To the north and south of the slipping zone, the fault is locked. The transition zone between locked and free segments is just northwest of Parkfield, and the accumulating strain, coupled with nearly regular earthquakes spanning over 100 years, has led many to believe that an earthquake is imminent. Understanding the slip distribution at Parkfield, particularly in the transition zone where the surface deformation will exhibit variable properties, can lead to better models of the locking / slipping mechanisms. New work with ERS data, shown in Fig. 39, has demonstrated the existence of slip [94] but the data are not sufficiently constrained to model the mechanisms.

Fig. 39. Aseismic slip along the San Andreas Fault near Parkfield, California, imaged interferometrically by ERS-1.

Interseismic displacements, occurring between earthquakes, have never been measured to have local transient signatures near faults. The sensitivity of the required measurement, and the variety of spatial scales that need to be examined are ideally suited to a properly designed InSAR system. The expectation is that interferometry will provide the measurements over time and space that are required to map interseismic strain accumulation associated with earthquakes.

Active volcanic processes have been measured through deflation measurements and through decorrelation of disrupted surfaces. While Massonnet *et al.* [95] showed up to 12 cm of deflation at Mount Etna over a 3 year period, Rosen *et al.* [25] demonstrated over 10 cm in 6 months at an active lava vent on Kilauea volcano in Hawaii. Zebker *et al.* [108] showed that lava breakouts away from the vent itself decorrelated the surface, and from the size of the decorrelated area, an estimate of the lava volume could be obtained.

Decorrelation processes may also be useful as disaster diagnostics. Figure 40 shows the signature of decorrelation due to the Kobe earthquake as measured by the JERS-1 radar. Field analysis of the decorrelated regions shows that areas where buildings were located on landfill collapsed, whereas other areas that did not decorrelate were stable. Vegetation is also partially decorrelated in this image, and an operational monitoring system would need to distinguish expected temporal decorrelation, as in trees, from disaster related events.

Fig. 40. Decorrelation in the destroyed areas of Kobe city due to the 1995 M=6.8 earthquake. Areas where structures were firmly connected to bedrock remained correlated, while structures on sandy areas of liquefaction were destroyed and decorrelated in the imagery.

C. Glaciers

The ice sheets of Greenland and Antarctica play an important role in the earth's climatic balance. Of particular importance is the possibility of a significant rise in sea level brought on by a change in the mass balance of, or collapse of, a large ice sheet [110]. An understanding of the processes that could lead to such change is hindered by the inability to measure even the current state of the ice sheets.

Topographic data are useful for mapping and detecting changes in the boundaries of the individual drainage basins that make up an ice sheet [111]. Short-scale (i.e., a few ice thicknesses) undulations in the topography are caused by obstructions to flow created by the basal topography [111], [112]. Therefore, surface topography can be used to help infer conditions at the bed [113] and high resolution DEMs are important for modeling glacier dynamics. Although radar altimeters have been used to measure absolute elevations for ice sheets, they do not have sufficient resolution to measure short-scale topography. As a result, there is little detailed topographic data for the majority of the Greenland and Antarctic ice sheets.

Fig. 41. Ice velocity map draped on topography of Storstrømmen Glacier in Greenland. Both velocity and topography were generated by ERS interferometry. Ice velocity vectors show that the outlet of the glacier is blocked from flow. In addition to aiding visualization of the ice flow, topographic maps such as this are an important measurement constraint on the mass balance, as changes in topographic height relate to the flow rate of ice from the glacier to the sea.

Ice-flow velocity controls the rate at which ice is transported from regions of accumulation to regions of ablation. Thus, knowledge of the velocity and strain rate (i.e., velocity gradient) are important in assessing mass balance and in understanding the flow dynamics of ice sheets. Ground-based measurements of ice-sheet velocities are scarce because of logistical difficulties in collecting such data. Ice-flow velocity has been measured from the displacement of features observed in sequential pairs of visible [114], [115] or SAR images [116], but these methods do not work well for the large, featureless areas that comprise much of the ice sheets. Interferometric SAR provides a means to measure both detailed topography and flow velocity.

Fig. 42. Horizontal velocity field plotted over the SAR amplitude image of the Ryder Glacier. Contour interval is 20 m/yr (cyan) for velocity less than 200 m/yr and is 100 m/yr (blue) for values greater than 200 m/yr. Red arrows indicate flow direction and have length proportional to speed.

C.1 Ice Topography Measurement

The topography of ice sheets is characterized by minor undulations with small surface slopes, which is well suited to interferometric measurement. While the absolute accuracy of interferometric ice-sheet topography measurements is generally poorer than that of radar (for flat areas) or laser altimeters, an interferometer is capable of sampling the ice sheet surface in much greater detail. While not useful for direct evaluation of ice sheet thickening or thinning, such densely sampled DEMs are useful for studying many aspects of ice sheet dynamics and mass balance.

The Canadian Center for Remote Sensing has used its airborne SAR to map glacier topography on Bylot Island in the Canadian Arctic [117]. The NASA/JPL TOPSAR interferometer was deployed

over Greenland in the May 1995 to measure ice-sheet topography.

Repeat-pass estimation of ice-sheet topography is slightly more difficult as the motion and topographic fringes must first be separated. Kwok and Fahnestock [79] demonstrated that this separation can be accomplished as a special case of the three-pass approach. For most areas on an ice sheet, ice flow is steady enough so that it yields effectively the same set of motion-induced fringes in two interferograms with equal temporal baselines. As a result, two such interferograms can be differenced to cancel motion, yielding a topography-only interferogram that can be used to create a DEM of the ice-sheet surface. Joughin *et al.* [47], [118] applied this technique to an area in western Greenland and obtained relative agreement with airborne laser altimeter data of 2.6 m.

With topography isolated by double differencing, the motion-topography separation can be completed with an additional differencing using the topography-only interferogram and either of the original interferograms to obtain a motion-only interferogram.

C.2 Ice Velocity Measurement

Goldstein *et al.* [19] were the first to apply repeat-pass interferometry to the measurement of ice motion when they used a pair of ERS-1 images to map ice flow on the Rutford Ice Stream, Antarctica. With the availability of ERS data, the ability to interferometrically measure ice-sheet motion is maturing rapidly as indicated by a number of recent publications. Joughin *et al.* [119] and Rignot *et al.* [120] studied ice-sheet interferograms created from long strips of imagery from the west coast of Greenland sheet that exhibited complex phase patterns due to ice motion. Hartl *et al.* [127] observed tidal variations in interferograms of the Hemmen Ice Rise on the Filchner-Ronne Ice Shelf. Kwok and Fahnestock [79] measured relative motion on an ice stream in northeast Greenland. The topography and dynamics of the Austofonna Ice Cap, Svalbards has been studied using interferometry by Unwin and Wingham [132].

Without accurate baseline estimates and knowledge of the constant associated with phase unwrapping, velocity estimates are only relative and are subject to tilt errors. To make absolute velocity estimates and improve accuracy, ground-control points are needed to accurately determine the baseline and unknown phase constant. In Greenland the ice sheet is surrounded by mountains so that is often possible to estimate the baseline using ground-control points from stationary ice-free areas. When the baseline is fairly short (i.e., < 50 m), baseline estimates are relatively insensitive to the ground-control height error, allowing accurate velocity estimates even with somewhat poor ground-control [121]. For regions deep in the interior of Greenland and for most of Antarctica, which has a much smaller proportion of ice-free area, ground-control points often must be located on the ice sheet where the velocity of the points must also be known. While such in situ measurements are difficult to make, four such points yield a velocity map covering tens of thousands of square kilometers.

Interferograms acquired along a single-track are sensitive only to the radar line-of-sight component of the ice-flow velocity vector. If the vertical component is ignored or at least partially compensated for using surface-slope information [121], then one component of the horizontal velocity vector can be measured. If flow direction can be determined the full flow vector can be determined. Over limited areas flow direction can be inferred from features visible in the SAR imagery such as shear margins. Flow direction can also be estimated from the direction of maximum averaged (i.e., over scales of a several kilometers) downhill slope [111]. Either of these estimates of flow direction have poor spatial resolution. Even when the flow direction is well known, accuracy of the resulting velocity estimate is poor when the flow direction is close to that of the along-track direction where there is no sensitivity to displacement. As a result, the ability to determine the full three-component flow vector from data acquired along a single satellite track is limited.

In principle, direct measurement of the full three-component velocity vector requires data collected along three different satellite track headings. These observations could be acquired with a SAR that can image from either side (i.e., a north/south looking instrument). Current spaceborne SARs, however,

acquire interferometric data typically from a north-looking configuration, with the exception of a short duration south-looking phase for RADARSAT. Except for this brief episode, it is not possible to obtain north- and south-looking coverage at high latitudes (above 80 degrees) so that direct comprehensive measurement is not possible over large parts of Antarctica.

With the assumption that ice flow is parallel to the ice-sheet surface, it is possible to determine the full three-component velocity vector using data acquired from only two directions and knowledge of the surface topography. Such acquisitions are easily obtained using descending and ascending satellite passes. This technique has been applied by Joughin et al. to the Ryder Glacier Greenland [122] (see Fig. 42). Mohr et al. [126] have also applied the surface-parallel flow assumption to derive a detailed three-component velocity map of Storstrommen Glacier in northeastern Greenland.

With the surface-parallel flow assumption, small deviations from surface-parallel flow (i.e., the submergence and emergence velocity) are ignored without consequence for many glaciological studies. These variations from surface parallel flow, however, do contain information on local thickening and thinning rates. Thus, for some ice sheet studies it is important to collect data from three directions where feasible.

C.3 Glaciological Applications

As measurement techniques mature, interferometry is transitioning from a stage of technique development to one where it is a method routinely applied for ice-sheet research. One useful interferometry application is in monitoring outlet glacier discharge. A substantial portion of the mass loss of the Greenland and Antarctic ice sheets results from discharge of ice through outlet glaciers. Rignot [128] used estimates ice thickness at the grounding line and interferometric velocity estimates to determine discharge for several glaciers in northern Greenland. Joughin et al. [130] have measured discharge on the Humboldt and Petermann Glaciers in Greenland by combining interferometrically measured velocity data with ice thicknesses measured with the University of Kansas airborne radar depth sounder.

Because the ice sheets have low surface slopes, grounding line positions, the boundaries where an ice sheet meets the ocean and begins to float, are highly sensitive to thickness change. Thus, changes in grounding line position should provide early indicators of any thickening or thinning caused by global or local climate shifts. Goldstein et al. mapped the location of the grounding line of the Rutford Ice Stream using a single interferometric pair. Rignot [124] developed a three-pass approach that improves location accuracy to a few tens of meters. He has applied this technique to locate grounding lines for several outlet glaciers in Northern Greenland.

Fig. 43. Grounding line time series (Courtesy: E. Rignot; Copyright *Science*), illustrating the retreat of Pine Island Glacier.

Little is known about the variability of flow speed of large outlet glaciers and ice streams. Using ERS-1 tandem data, Joughin et al. [123] observed a mini-surge on the Ryder Glacier, Greenland. They determined that speed on parts of the glacier of glacier increased by a factor of three or more and then returned to normal over a period of less than seven weeks. Mohr *et al.* [126] have observed a dramatic decrease in velocity on Storstrommen glacier, Greenland after a surge.

C.4 Temperate Glaciers

Repeat-pass interferometric measurements of temperate glaciers can be far more challenging than those of ice sheets. Temperate glaciers are typically much smaller and steeper, making them more difficult to work with interferometrically. Furthermore, many temperate glaciers are influenced strongly by maritime climates resulting in high accumulation rates, frequent storms, and higher temperatures that make it difficult to obtain good correlation. Nevertheless measurements have been made on temperate glaciers. Rignot used repeat-pass SIR-C interferometry to study topography and ice motion

on the San Rafael Glacier, Chile [125]. Mattar *et al.* [131] obtained good agreement between their interferometric velocity estimates and in situ measurements.

D. Ocean Mapping

The along-track interferometric (ATI) SAR approach can be used to measure motion of targets within the SAR imagery. The first application of this technique was a proof-of-concept experiment in the mapping of tidal ocean surface current over the San Francisco Bay using an airborne ATI SAR ([18]. In that experiment, interferometric SAR signals were obtained from two antennas which were attached near the fore and the aft portions of the NASA DC-8 aircraft fuselage. While one of the antennas was used for radar signal transmission, both of the antennas were used for echo reception. Interferometric measurements were obtained by combining the signals from the fore and the aft antennas by 'shifting', in the along-track dimension, the signals from the two antennas such that the signals were overlaid when the two antennas were at approximately the same along-track path location. For the DC-8 aircraft flight speed and the spatial separation of the fore and aft antennas, the aft antenna data were obtained about 0.1 sec after the fore antenna. The measured interferometric phase signals correspond to the movement in the ocean surface between the 0.1 sec interval. Adjustments in the data processing were also made to remove effects due to random aircraft motion and aircraft attitude deviations from a chosen reference. The interferometric phase signals were then averaged over large areas. The resulting average phase measurements were shown to correspond well to those expected due to tidal motion in the ocean surface during the experiment. The tidal motion detected was about 1 m/s, which was consistent with the in situ tidal data available and the ATI SAR measurement accuracy, after the large area averaging, was in the range of 10 cm/s. Figure 44 shows results from a similar ATI experiment conducted at Mission Bay, San Diego, California [136]. The flight tracks were oriented in several directions, to measure different components for the velocity field (the ATI instrument measures only the radial component of motion). In particular note that in Fig. 44a, the wave patterns are clearly visible because the waves are propagating away from the radar toward the shore. In Fig. 44b on the other hand, the waves are propagating orthogonal to the radar look direction, so only the turbulent breaking waves contribute to the radial velocity.

Fig. 44. Example of ocean currents measured by along-track SAR interferometry. Flight direction of the radar is from left to right in each image, so panels a-d show different look aspects of the wave patterns propagating to shore.

Goldstein *et al.* [18] applied this technique to derive direct, calibrated measurements of ocean wind wave directional spectrum. This proof-of-concept experiment was performed in conjunction with the Surface Wave Process Program experiment. Instead of averaging the phase measurements over large areas, the phase measurements obtained for the intrinsic SAR resolution elements were used to measure the displacement of the ocean surface. Typically, this displacement is the algebraic sum of the small displacements of the Bragg waves, such as the phase velocity of the Bragg waves themselves, the orbital velocity associated with the swell upon which they ride, and any underlying surface current that may be present. In this experiment, the orbiting motion components due to the wind waves are separated from the Bragg phase velocity and the ocean currents on the basis of the spatial frequencies. The Bragg and the ocean current velocities are usually steady over large areas, whereas the swell is composed of higher spatial frequencies than are of interest in the ocean wave spectra measurements. It should be noted that the Bragg waves are not imaged directly as waves, rather they are the scatterers providing the radar return. Because the interferometer measures directly the line-of-sight velocity, independent of such variables as radar power, antenna gain, surface reflectivity, etc. it enables the determination of the actual height of the ocean waves via linear wave theory. Goldstein *et al.* compared the ocean wave spectra results from the interferometric SAR approach to other conventional in situ measurements and obtained reasonable agreements. Unfortunately, the data set reported was limited

to one oceanic condition and more extensive data sets are required to ascertain the effectiveness of this remote sensing technique for ocean wave spectra measurements. Other applications of the ATI technique can be found in the literature [133], [134], [135].

E. Vegetation Algorithms

The use of interferometry for surface characterization and classification is a rapidly growing area of research. While not as well validated by the community as topography and deformation observations, recent results, some shown here, have much promise.

Vegetation canopies have two effects on interferometric signals: first, the mean height reported will lie somewhere between the top of the canopy and the ground; second, the interferometric correlation coefficient will decrease due to the presence of volume scattering. The first effect is of great importance to the use of InSAR data for topographic mapping since, for many applications, the bare-earth heights are desired. It is expected that the reported height depends on the penetration characteristics into the canopy, which, in turn, depends on the canopy type, the radar frequency, and the incidence angle.

The first reported values of the effective tree height for interferometry was made by Askne *et al.* [137] [138], using ERS-1 C-band repeat-pass interferometry over boreal forests in northern Sweden. For very dense pine forests, whose average height was approximately 16 m, the authors observed effective tree heights varying between 3.4 m and 7.4 m. For mixed Norway Spruce (average height 13 m) and Pine/Birch (average height 10 m) forests, the authors observed effective heights varying between 0 m and 6 m. The bulk of the measurements were not very dependent on the interferometric baseline, although the lowest measurements were obtained for the case with the lowest correlation, indicating that the effect of temporal decorrelation could have affected the reported height: the reported height will be due to the scatterers which do not change between passes, such as trunks and large branches or ground return.

To separate the effect due to penetration into the canopy and temporal decorrelation, it is necessary to examine data collected using cross-track interferometry, that is using two or more apertures on a single platform. Rodríguez *et al.* [139] collected simultaneous InSAR and laser altimeter data over mixed coniferous forests in southern Washington State, using the JPL TOPSAR interferometer and the NASA GSFC laser profilometer, respectively. Figure 45 shows the laser determined canopy top and bottom together with the InSAR estimated height over a region containing mature stands as well as clear-cuts exhibiting various stages of regrowth. As can be seen from this figure, even for mature forest stands, the InSAR height is approximately half-way between the canopy top and the ground, consistent with the results obtained by Askne *et al.* This indicates that the observed effects are largely due to penetration into the canopy, and not due to temporal decorrelation. Rather, Rodríguez *et al.* propose that the bulk of the penetration occurs through gaps in the canopy, a result which is consistent with the decorrelation signature presented below. The results of both Askne *et al.* and Rodríguez *et al.* show that penetration into boreal or mixed coniferous forests is significantly higher than that expected using laboratory/field measurements of attenuation from individual tree components, leading to the conclusion that the canopy gap structure (or the area fill factor) plays a leading role in determining the degree of penetration.

Fig. 45. Profiles of canopy extent as measured by the Goddard Space Flight Center Airborne Laser Altimeter, compared with JPL TOPSAR (C-band) elevation estimates along the same profiles. A clear distinction is seen between the laser-derived canopy extents and the interferometer height, which generally lies midway in the canopy, but varies depending on canopy thickness and gap structure.

The effect of volumetric scattering on the correlation coefficient was also examined by Askne *et al.*, and a simple electromagnetic model assuming a homogeneous cloud scatterer model and an area fill factor was presented. Using this model, attenuation and area fill parameters could be adjusted to

make the model agree with the effective tree height. However, the predicted decorrelation could not be compared against measurements due to the contribution of temporal decorrelation.

Treuhaft et al. [141] used a similar parametric single layer homogeneous canopy model (not including area fill factors) to invert for tree height and ground elevation using cross-track interferometric data over a boreal forest in Alaska. The number of model parameters was greater than the number of available observations, so assumptions had to be made about the medium dielectric constant. While measurements were made during thaw conditions, it was observed that better agreement with ground truth was obtained if the frozen dielectric constant (resulting in smaller attenuation) was used in the model. The results for the inversion of tree height are shown in Fig. 46. In general, good agreement is observed if the frozen conditions dielectric constant is used, but the heights are overestimated if the thawed dielectric constant is used. This difference may indicate the need for an area fill factor or canopy gap structure, as advocated by Askne *et al.* and Rodríguez *et al.*, or the inclusion into the model of ground trunk interactions (Treuhaft, private communication, 1997), which would lower the canopy phase center.

Fig. 46. Inversion of interferometric data from JPL TOPSAR for tree height. After Treuhaft, 1997.

In an attempt to overcome what are potentially oversimplifying assumptions about the vegetation canopy, Rodríguez et al. [139] introduced a non-parametric method of estimating the effective scatterer standard deviation using the volumetric decorrelation measurement. They showed that the effective scatterer variance (i.e., the normalized standard deviation of the radar backscatter, including variations due to intrinsic brightness and attenuation, as a function of height), σ_Z^2 , could be estimated from the volumetric correlation γ_Z , given by Eq. 63, by means of the simple formula

$$\sigma_Z^2 = \frac{2(1 - \gamma_Z)}{\kappa_Z^2} \quad (74)$$

Rodríguez et al. hypothesized that if, at high frequencies, the dominant scattering mechanism into the canopy was geometric (i.e., canopy gaps), this quantity should be very similar to the equivalent quantity derived for optical scattering measurements, since in both cases the cross section is proportional to the geometric cross section, and the gap penetration is frequency independent. In fact, Figure 45 shows that this is observed for the laser and InSAR data collected over Washington State. Rodríguez et al. speculated that a simple scaling of the estimated scatterer standard deviation might provide a robust estimate of tree height. That this is in fact the case is shown in Figure 47, where measured tree heights are compared against estimated tree heights.

Fig. 47. Estimated scatterer standard deviation compared to tree height deviation derived by laser altimeter. Scatter plot shows relatively modest correlation, an indication of the limited ability to discriminate the volumetric decorrelation term from other decorrelation effects, such as thermal, processor, and ambiguity noise. Many of these limitations can be controlled by proper system design.

Summarizing, it is clear that significant penetration into forest canopies is observed in InSAR data, and it is speculated that the dominant mechanism is due to penetration through gaps in the canopy, although other mechanisms, such as ground-trunk interactions, may also play a significant role. Current research focuses on the evaluation of penetration characteristics over other vegetation types, the study of the frequency dependence of penetration, and the improvement of inversion techniques for canopy parameter estimation.

F. Terrain Classification Using InSAR Data

The use of interferometric data for terrain classification is relatively new. Two basic approaches have been used for terrain classification using InSAR: 1) classification using multi-temporal repeat-pass interferometric data; and, 2) classification using simultaneous collection of both InSAR channels (cross-track interferometry). The idea of using multi-temporal repeat-pass data is to make use of the fact, first documented by Zebker and Villasenor [58], that different types of terrains have different temporal correlation properties due to a varying degree of change of the scatterer characteristics (position and electrical) between data takes. Zebker and Villasenor found, using SEASAT data over Oregon and California, that vegetated terrain, in particular, exhibited an interferometric correlation which decreased almost linearly with the temporal separation between the interferometric passes. These authors, however, did not use this result to perform a formal terrain classification.

A more systematic study of the temporal correlation properties of forests was presented by Wegmuller and Werner [142], using ERS-1 repeat-pass data. By examining a variety of sites, they found that urban areas, agriculture, bushes, and forest had different correlation characteristics, with urban areas showing the highest correlation between passes and forests the lowest (water shows no correlation between passes). When joint correlation and brightness results are plotted for each class (see Fig. 48), the different classes tend to cluster, although some variation between data at different times is observed.

Fig. 48. Classification space showing image brightness vs. interferometric correlation. Terrain types cluster as indicated.

Based on their 1995 work, Wegmuller and Werner [143] presented a formal classification scheme based on the interferometric correlation, the backscatter intensity, the backscatter intensity change, and a texture parameter. A simple classifier based on setting characteristic independent intervals for each of the classification features was used. The typical class threshold settings were determined empirically using ground truth data. Classification results for a test site containing the city of Bern, Switzerland, were presented (see Figure 49) and accuracies on the order of 90% were observed for the class confusion matrix.

Fig. 49. Classification of Bern, Switzerland using ERS interferometric time series data to distinguish features.

The use of cross-track InSAR data for classification was presented in Rodríguez et al. [140], using the C-band JPL TOPSAR instrument over a variety of sites. Unlike multi-temporal data, cross-track InSAR data does not show temporal decorrelation and the feature vectors used for classification must be different. To differentiate between forested and non-forested terrain, these authors estimated the volumetric decorrelation coefficient, γ_Z , presented above to estimate scatterer standard deviations to be used as a classification feature. In addition, the radar backscatter, the rms surface slope, and the brightness texture were used in a Bayesian classification scheme which used mixtures of Gaussians to characterize the feature vector multi-dimensional distributions. Four basic classes (water, fields, forests, and urban) were used for the classification, and an evaluation based on multiple test sites in California and Oregon was presented. An example of the results for the San Francisco area are shown in Figure 50.

Fig. 50. Classification of San Francisco using JPL TOPSAR (C-band) image brightness, interferometric correlation, and topographic height and slope.

Rodríguez *et al.* found that classification accuracies in the 90% level were generally obtained, although significant ambiguities could be observed under certain conditions. Specifically, two problems

were observed in the proposed classifications scheme: 1) sensitivity to absolute calibration errors between sites; and, 2) ambiguities due to changes in backscatter characteristics as a function of incidence angle. The effects of the first problem were apparent in the fact that same-site classification always yielded much higher classification accuracies than classification collected for similar sites at different times, probably due to changes in the instrument absolute calibration. The second problem is more fundamental: for small incidence angles (up to about 25°) water can be just as bright as fields, exhibits similar texture and no penetration, causing systematic confusion between the two classes. However, if the angular range is restricted to be greater than 30° , this ambiguity is significantly reduced due to the rapid drop-off of the water backscatter cross section with incidence angle.

Based on these early results, we conclude that InSAR data, although quite different in nature from optical imagery and polarimetric SAR data, shows potential to be used for terrain classification using both multi-temporal and cross-track data. More work is needed, however, to fully assess the ultimate accuracy and potential of this technique to separate classes. Improvement in classification accuracy may also arise in systems that are simultaneously interferometric and polarimetric. Cloude and Papathanassiou [144] showed that polarimetric decompositions of repeat-pass interferometric data acquired by SIR-C carry additional information about the scattering height. These improvements may extend to cross-track polarimetric interferometers.

VI. OUTLOOK

Over the past 2 decades, there has been a continuous maturing of the technology for interferometric SAR systems, with an associated impressive expansion of the potential applications of this remote sensing technique. One major area of advance is the overall understanding of the system design issues and the contribution of the various sources of uncertainties to the final geophysical parameter measured by an interferometric SAR. These improvements allow systematic approaches to the design, simulation and verification of the performance of interferometric SAR systems. We witnessed the changes from analog signal processing techniques to automated digital approaches, which significantly enhanced the utility of the data products as well as improved on the accuracy and repeatability of the results. Several airborne interferometric SAR systems are currently routinely deployed to provide high resolution topography measurements as well as other data products for geophysical studies. Finally, the spectrum of applications of the interferometric SAR data to multiple scientific disciplines has continued to broaden with an expanding publication of the results from proof-of-concept experiments across these disciplines.

With these advances, the use of spaceborne interferometric SAR systems will be the “approach of choice” for high resolution topography mapping on a regional as well as a global scale. The continuing improvements in the technologies for spaceborne radar systems and the associated data processors will make such an approach more affordable and efficient. We speculate that in the next decade there will be additional spaceborne missions which will provide higher resolution and better height accuracy topography data than those expected for the SRTM mission. Obviously, the key issue of the influence of surface cover, such as vegetation, on the topography results from SARs should be pursued further to allow a better understanding of the relation of the results to the topography of the bare earth.

Airborne interferometric SARs are expected to play an increasing role supplying digital topographic data to a variety of users requiring regional scale topographic measurements. The relatively quick processing of InSAR data compared to optical stereo processing makes InSAR attractive from both schedule and cost considerations. More advanced systems are expected to increase the accuracy and utility of airborne InSAR systems by increasing the bandwidth to achieve higher resolution, moving to lower frequencies, as with the GeoSAR system being developed at JPL for sub-canopy mapping, and to systems which are both fully polarimetric and interferometric to exploit the differential scattering mechanisms exhibited by different polarizations [144].

We also speculate that the use of repeat-track observations of interferometric SAR for minute surface

deformation will become an operational tool for researchers as well as other civilian users to study geophysical phenomena associated with earthquakes, volcanoes, etc. We expect that the results from long term studies using this tool will lead to a significantly better understanding of these phenomena. This improvement will have a strong impact on earth science modeling and the forecasting of natural hazards. As described in Section IV-A.5, the changes in the atmosphere (and the ionosphere) will continue to affect the interpretation of the results. However, by combining data from long time series, it is expected that these effects will be minimized. In fact, we speculate that, once these effects can be isolated from long duration observations, the changes in the atmospheric and ionosphere conditions can become geophysical observations themselves. These subtle changes can be measured with spatial resolutions currently unavailable from on-going spaceborne sensors, and they, in turn, can be valuable input to atmospheric and ionospheric studies.

Future SAR missions optimized for repeat-pass interferometry should allow mapping of surface topography and velocity over entire Greenland and Antarctic ice sheets providing data vital to improving our understanding of dynamics that could lead to ice-sheet instabilities and to determining the current mass balance of the ice sheets. We expect these applications to become routine for glaciology studies.

While large scale application of InSAR data to the areas described above has been hampered by the lack of optimized interferometric data to the science community, we expect this situation to improve significantly in the upcoming decade with the advent of spaceborne SAR systems with inherently phase stable designs, and equipped with GPS receivers for precise orbit and baseline determination. Dramatic improvements in throughput and quality of SAR data processing, both at centers and by individual investigators through research and commercial software packages, will increase accessibility of the data and methods to the community, allowing routine exploitation and exploration of new application areas across Earth science disciplines. Several missions with repeat-track interferometric capability are under development, including ENVISAT in Europe, ALOS in Japan, RadarSAT 2 in Canada, and LightSAR in the United States.

There are also clear applications of InSAR data from these missions in the commercial sector, in areas such as urban planning, hazard assessment and mitigation, and resource management. In addition to the already commercially-viable topographic mapping applications, urban planners may take advantage of subsidence maps to choose or modify pipe-line placements, or monitor fluid withdrawal to ensure no structural damage. Emergency managers may in the future use InSAR derived damage maps, as crudely illustrated in Fig. 40, to assess damage after a disaster synoptically, day or night, and through cloud or smoke cover. Agricultural companies and government agencies may use classification maps such as Fig. 49 to monitor crop growth and field usage, supplementing existing optical remote sensing techniques with sensitive change maps. This is already becoming popular in Europe. These potential commercial and operational applications in turn may provide the drive for more InSAR missions.

Finally, we speculate that this technique will be used beyond the mapping of the earth. It is quite possible to apply this technique to topography mapping in many planetary bodies in the solar system. Although the complexity of the radar systems, the data rates and the required processing power are very challenging, we believe that as we continue to improve radar technology, it will be possible to utilize this technique for detailed studies of planetary surfaces. In fact, it is conceivable that the use of the differential interferometric SAR technique will also allow us to investigate the presence of subtle surface changes and probe into the mysteries of the inner workings of these bodies.

Acknowledgments

We are grateful to the research and management staff at the Jet Propulsion Laboratory for encouraging us to work on this review, and to those who supplied figures and reviewed the first drafts, including, Elaine Chapin, Tom Farr, Gilles Peltzer, and Eric Rignot. We thank the IEEE Proceeding editor, Jim Calder, for accommodating us. We are also extremely grateful to the four reviewers who gave their time to help us to fashion a balanced review. The European Space Agency and the National

Space Development Agency of Japan have generously supported several of the authors with ERS-1/2 and JERS-1 data, respectively, through research initiatives. This paper was written at the Jet Propulsion Laboratory, California Institute of Technology, under contract with the National Aeronautics and Space Administration, with sponsorship from the National Imagery and Mapping Agency, the Defense Advanced Research Projects Agency, and the Solid Earth and Natural Hazards Program Office at NASA.

APPENDIX

I. SAR PROCESSING CONCEPTS FOR INTERFEROMETRY

The precise definition of interferometric baseline and phase, and consequently the topographic mapping process, depends on how the SAR data comprising the interferometer are processed. Consequently a brief overview of the salient aspects of SAR processing is in order.

Processed data from SAR systems are sampled images. Each sample, or pixel, represents some aspect of the physical process of radar backscatter. A resolution element of the imagery is defined by the spectral content of the SAR system. Fine resolution in the range direction is achieved typically by transmitting pulses of either short time duration with high peak power, or of a longer time duration with a wide, coded signal bandwidth at lower peak transmit power. Resolution in range is inversely proportional to this bandwidth. In both cases, the received echo for each pulse is sampled at the required radar signal bandwidth.

Fig. 51. The radar emits a sequence of pulses separated in time. The time duration between pulses is called the inter pulse period (IPP) and the associated pulse frequency is called the pulse repetition frequency (PRF=1/IPP). The pulse duration is denoted τ .

For ultra-narrow pulsing schemes, the pulse width is chosen at the desired range resolution, and no further data manipulation is required. For coded pulses, the received echoes are typically processed with a matched filter technique to achieve the desired range resolution. Most spaceborne platforms use chirp-encoding to attain the desired bandwidth and consequent range resolution, where the frequency is linearly changed across the pulse as illustrated in Fig. 51.

Resolution in the azimuth, or along-track, direction, parallel to the direction of motion, is achieved by synthesizing a large antenna from the echoes received from the sequence of pulses illuminating a target. The pulses in the synthetic aperture contain an unfocussed record of the target's amplitude and phase history. To focus the image in azimuth, a digital "lens" that mimics the imaging process is constructed, and is applied by matched filtering. Azimuth resolution is limited by the size of the synthetic aperture, which is governed by the amount of time a target remains in the radar beam. The azimuth beamwidth of an antenna is given by $\theta_{bw} \equiv k\lambda/L$, where λ is the wavelength, L is the antenna length, and k is a constant that depends on the antenna ($k = 1$ is assumed in this paper). The size of the antenna footprint on the ground in the azimuth direction is approximately given by

$$l_{az} = \rho\theta_{bw} = \rho\frac{\lambda}{L} \quad (75)$$

where ρ is the range to a point in the footprint as depicted in Fig. 52.

Fig. 52. The antenna footprint size in the azimuth direction depends on the range and the antenna beamwidth in the azimuth direction. Figure shows forward-squinted beam footprint.

During the time a target is in the beam, the range and angular direction to the target are changing from pulse to pulse, as shown in Fig. 53. To generate a SAR image, a unique range or angle must be selected from the family of ranges and angles to use as a reference for focussing the image. Once selected, the target's azimuth and range position in the processed image is uniquely established. Specifying an angle for processing is equivalent to choosing a reference Doppler frequency. The bold dashed line from pulse N-2 to the target in Fig. 53 indicates the desired angle or Doppler frequency at which the target will be imaged. This selection implicitly specifies the time of imaging, and therefore the location of the radar antenna. This is an important and often ignored consideration in defining the interferometric baseline. The baseline is the vector connecting the locations of the radar antennas

forming the interferometer; since these locations depend on the choice of processing parameters, so does the baseline. For two-aperture cross track interferometers, this is a subtle point, however for repeat track geometries where the antenna pointing can be different from track to track, careful attention to the baseline model is essential for accurate mapping performance.

Fig. 53. A sensor imaging a fixed point on the ground from a number of pulses in a synthetic aperture. The range at which a target appears in an synthetic aperture image depends on the processing parameters and algorithm used to generate the image. For standard range-Doppler processing the range is fixed by choosing the pulse which has a user defined fixed angle between the velocity vector and the line-of-sight vector to the target. This is equivalent to picking the Doppler frequency.

II. ATMOSPHERIC EFFECTS

For interferometric SAR systems that obtain measurements at two apertures nearly simultaneously, propagation through the atmosphere has two effects which influence interferometric height recovery: 1) delay of the radar signal; and, 2) bending of the propagation path away from a straight line. In practice, for medium resolution InSAR systems, the first effect dominates.

The atmospheric index of refraction can be written as

$$n(z) = 1 + \delta(z) \quad (76)$$

where z is the height above sea level, and $\delta(z)$ represents the variation of the index of refraction as a function of height, and is typically of the order of 10^{-4} . Commonly, an exponential reference atmosphere $\delta(z) = a \exp[-z/H]$ is used as a model. Typical values of a and H are 3.13×10^{-4} and 6.949 km, respectively.

Rodríguez et al. [24] showed that the relationship between the geometric range ρ and the path distance $\check{\rho}$ is

$$\check{\rho} = \rho \left[1 + \bar{\delta} - \frac{1}{2} \sigma_{\delta}^2 \left[\left(\frac{\rho}{\Delta h} \right)^2 - 1 \right] \right] \quad (77)$$

where $\bar{\delta}$ and σ_{δ}^2 correspond to the height-dependent mean and variance of the variations of the index of refraction, respectively. These two quantities are functions of the height difference between the scatterer and the receiver, Δh , and the height of the scatterer above sea level, h_0 . Using the exponential reference model, it is easily seen that the bulk of the effect is dominated by $\bar{\delta}$, i.e., by the mean speed of light in the medium, and produces a fractional error in the range on the order of 10^{-4} if left uncorrected. Corrections based on simple models, such as an exponential atmosphere, can account for most of the effect and are straightforward to implement.

In a similar way, the interferometric phase can be approximated by

$$\phi \approx -k \Delta \rho (1 + \bar{\delta}) + k \rho (\delta(h) - \bar{\delta}) \frac{\delta h}{\Delta h} \quad (78)$$

where $\Delta \rho$ is the geometric range difference in the path lengths to the InSAR antennas, and δh is the height separation between the two antennas. At first sight, it might seem as if the last term can be neglected. However, this is not always the case since it is multiplied by the range, which is a large factor.

The results above show that, if one accounts for the mean speed of light of the atmosphere, atmospheric effects will be largely accounted for in single-pass interferometry. This is not the case for repeat-pass interferometry since the atmospheric delays can be different for each pass, and the phase can be dominated by tropospheric variations.

TABLE B-1: SYMBOLS

Symbol	Definition
--------	------------

f_{Dop}	Doppler frequency
λ	Radar wavelength
$\rho, (\rho_i)$	Radar range, (with subscript from i th antenna phase center to a target)
$\varphi, (\varphi_i)$	Propagation phase, (with subscript for i th propagation path)
ϕ_{npp}	Phase difference between radar channels in standard, or “non-ping-pong” measurement mode
ϕ_{pp}	Phase difference between radar channels in “ping-pong” measurement mode
p	1 for standard mode, 2 for ping-pong mode
ϕ_{m}	Measured (wrapped) phase difference between radar channels
ϕ_{top}	Phase difference resulting from surface topography
ϕ_{unw}	Unwrapped phase difference
k_{unw}	Integer function multiplying 2π needed to unwrap the phase
k_{abs}	Integer constant multiplying 2π needed to set the absolute phase
$\delta\rho$	Small range distance
\vec{T}	Target position vector from arbitrary reference
\vec{l}_i	Look vector, measured from i th platform position reference to target
\hat{l}_i	Unit look vector
\vec{P}_i	Position vector of i th platform reference, such as antenna phase centers or airframe center of mass
\vec{B}	Baseline vector, from phase center of one interferometric aperture to another
\hat{B}	Unit vector in direction of baseline
B	Magnitude of the baseline vector
ϕ	general interferometric phase difference between radar channels
α	baseline angle measured counterclockwise from a horizontal reference
θ	Look angle measured counterclockwise from nadir
h_0	Surface of constant elevation
\hat{l}_0	Unit look vector to a point on constant height reference surface
θ_0	Look angle to a point on constant height reference surface
ρ_0	Radar range to a point on constant height reference surface
ϕ_{flat}	Interferometric phase with phase of constant reference surface removed
h_p	Platform height above Earth r_e
r_e	Earth radius
τ_c	Local terrain slope in cross track direction
i	Local radar incidence angle relative to a spherical Earth
B_{\perp}	Perpendicular baseline
$\Delta\rho$	Range resolution
$\Delta\rho_l$	Range resolution projected perpendicular to look direction
$B_{\perp,\text{crit}}$	Critical perpendicular baseline, beyond which complete decorrelation
f	Radar frequency
y_0	Cross-track platform ground coordinate
\vec{v}	Platform velocity
\hat{v}	Unit vector in direction of platform velocity
v	Magnitude of platform velocity

TABLE B-2: SYMBOLS

Symbol	Definition
s	Along-track, or azimuth, coordinate position
c	Across-track coordinate position
h	Vertical coordinate position
Δ	Differential operator applied in sensitivity analysis
h_a	Ambiguity height
τ_r^k	Total time delay through receiver k
τ_i	Delay in the i th filter/amplifier in receiver
ω_i	Frequency of the i th mixer in receiver
τ_{A_k}	Delay associated with antenna k amplifier electronics
\vec{D}	Surface displacement vector
t_i	Time instant i
z	Topographic height above the reference surface
$\delta\rho$	Surface displacement in range between imaging times
$p_i(t)$	Transmitted pulse from channel i
$h_i(t)$	Baseband transmitted waveform
f_0	Carrier frequency in Hertz
ω_0	Radian carrier frequency
t	Time variable
t_{di}	Round-trip propagaion time delay of radar signal from antenna i to target to antenna i
t_{d0}	Round-trip propagaion time delay of radar signal from antenna i to target to reference track
$s_i(t)$	Received signal of channel i
$t_{di,\text{REF}}$	Round-trip propagation time delay of radar signal from antenna i to reference elevation h_0 associated with target, then to antenna i
$t_{d0,\text{REF}}$	Round-trip propagation time delay of radar signal from antenna i to reference elevation h_0 associated with target, then to reference track
$g_i(t)$	Received signal of channel i resampled to reference track
$c(t, f_0)$	Interferometric correlation function
$c_{\text{spaceborne}}$	Typical spaceborne interferogram
Δt_{d21}	Time delay difference between channel 2 and 1
$\mathbf{W}()$	Phase wrapping operator
$\psi_{i,j}$	Wrapped interferometric phase
$\Delta_{i,j}^{x,y}$	Wrapped difference of wrapped phase
$\rho_{i,j}^{x,y}$	Source function consisting of wrapped phase differences
f_+	Upper sub-band carrier frequency
f_-	Lower sub-band carrier frequency
Δf	Sub-band carrier frequency difference
$\phi_{\pm}(t)$	Phase difference of sub-band interferograms
$\phi_{\text{unw}}(t)$	Unwrapped phase on correct absolute ambiguity
n	number of cycles to add to adjust to absolute phase
$g_j^S(t)$	Received signal of channel j resampled using unwrapped phase to adjust for topographic time delay variability
γ	Interferometric correlation
γ_N	Thermal noise correlation contribution
γ_G	Geometric correlation contribution
γ_Z	Volumetric correlation contribution
γ_T	Temporal correlation contribution
σ_{ϕ}^2	Interferometric phase variance

TABLE B-3: SYMBOLS

Symbol	Definition
N_L	Number of independent radar looks
SNR_i	Signal to noise ratio of i th radar channel
W_i	Impulse response of i th radar channel
k	Radar wavenumber
δk	Wavenumber shift
δ_ρ	Range error in interferometric image registration
δ_s	Azimuth error in interferometric image registration
τ_s	Terrain slope in azimuth direction
κ_ρ	Interferometric fringe wavenumber projected in range
κ_z	Interferometric fringe wavenumber projected in vertical direction
$f(z)$	Effective scatterer probability density function
$\sigma(z)$	Effective normalized backscatter cross-section per unit height
$s_{ps}(\rho_m)$	Range-compressed presumed pulse
s_{mc}	Motion compensated pulse
f_m	Resampling filter coefficients
ρ_m	Range at discrete locations for resampling
$\tilde{\rho}$	Range values of motion compensated pulse
$\delta\rho_{mc}$	Range component of motion-induced displacement
\vec{d}_i	Displacement vector from actual track to reference track
dh	Error in interferometrically derived height
\hat{l}_\perp	Perpendicular component of unit look vector
L	Antenna length along track
$N_{\text{"box"}}$	Pixel count in an averaging window for statistics computations
$N_{\text{"DEM"}}$	Pixel count in a DEM
z_{ref}	Topographic height from a reference DEM
σ_h	Height noise standard deviation
PRF	Radar Pulse Repetition Frequency
IPP	Radar Inter-Pulse Period
RF	Radio Frequency
L	Radar antenna length in the along track direction
θ_{bw}	Radar azimuth beamwidth
$n(z)$	Refractive index of atmosphere
$\delta(z)$	Variation in refractive index of atmosphere
a	Reference atmosphere refractivity at the surface of the Earth
H	Reference atmosphere scale height
$\tilde{\rho}$	Range path length
$\bar{\delta}$	Mean of refractivity variations
σ_δ^2	Variance of refractivity variations
Δh	Height difference between target and antenna
δh	Height difference between two antennas

REFERENCES

- [1] A. R. Thompson, J. M. Moran, and G. W. Swenson, *Interferometry and Synthesis in Radio Astronomy*, Wiley Interscience, 1986.
- [2] J. Kovaly. *Synthetic Aperture Radar*, Artech House Inc. 1976.
- [3] C. Elachi *Spaceborne Radar Remote Sensing: Applications and Techniques*, IEEE Press, New York, 1988.
- [4] J. C. Curlander and R. N. McDonough *Synthetic Aperture Radar Systems and Signal Processing*, Wiley-Interscience 1991.
- [5] F. Li and R. K. Raney, ed. "Special Section on Spaceborne Radars for Earth and Planetary Observations," *Proc. IEEE*, vol. 91.
- [6] R. K. Raney, "Synthetic aperture imaging radar and moving targets," *IEEE Trans. Aero. and Elect. Sys.*, vol. AE S-7, no. 3, 499-505, May 1971.
- [7] A. E. E. Rogers and R. P. Ingalls, "Venus: Mapping the surface reflectivity by radar interferometry," *Science*, vol. 165, 797-799, 1969.
- [8] S. H. Zisk, "A new Earth-based radar technique for the measurement of lunar topography," *Moon*, vol. 4, 296-300, 1972.
- [9] L. C. Graham, "Synthetic Interferometric Radar for Topographic Mapping," *Proc. IEEE*, vol. 62, no. 6, 763-768, June 1974.
- [10] H. A. Zebker and R. M. Goldstein, "Topographic mapping from interferometric SAR observations," *J. Geophys. Res.*, vol. 91, 4993-4999, 1986.
- [11] R. M. Goldstein, H. A. Zebker, and C. L. Werner, "Satellite radar interferometry: two-dimensional phase unwrapping," *Radio Science*, vol. 23, no. 4, 713-720, July-August 1988.
- [12] F. Li and R. M. Goldstein, "Studies of multibaseline spaceborne interferometric synthetic aperture radars," *IEEE Trans. Geosci. Rem. Sens.*, vol. 28, 88-97, 1990.
- [13] R. Gens and J. L. Vangenderen, "SAR interferometry - issues, techniques, applications," *Intl. J. Rem. Sens.*, vol. 17, no. 10, 1803-1835, 1996.
- [14] S. N. Madsen and H. A. Zebker, "Synthetic Aperture Radar Interferometry: Principles and Applications," Chapter 6 in *Manual of Remote Sensing*, vol. 3, Artech House, 1999.
- [15] R. Bamler and P. Hartl, "Synthetic Aperture Radar Interferometry," *Inverse Problems*, vol. 14, R1-54, 1998.
- [16] D. Massonnet and K. L. Feigl, "Radar interferometry and its application to changes in the earth's surface," *Rev. Geophys.*, vol. 36, no. 4, 441-500.
- [17] F. W. Leberl, "Radargrammetric Image Processing" Artech House 1990.
- [18] R. M. Goldstein and H. A. Zebker, "Interferometric radar measurement of ocean surface currents," *Nature*, vol. 328, 707-709 1987.
- [19] R. M. Goldstein, H. Engelhardt, B. Kamb, and R. M. Frolich, "Satellite radar interferometry for monitoring ice sheet motion: Application to an antarctic ice stream," *Science* vol. 262, 1525-1530, 1993.
- [20] A. K. Gabriel, R. M. Goldstein, and H. A. Zebker, "Mapping small elevation changes over large areas: Differential radar interferometry," *J. Geophys. Res.*, vol. 94, 9183-9191, 1989.
- [21] D. Massonnet, M. Rossi, C. Carmona, F. Adragna, G. Peltzer, K. Fiegl, and T. Rabaute, "The displacement field of the Landers earthquake mapped by radar interferometry," *Nature*, vol. 364, 138-142, 1993.
- [22] C. Prati, F. Rocca, A. Guarnieri, and E. Damonti, "Seismic migration for SAR focusing: interferometric applications," *IEEE Trans. Geosci. Rem. Sens.*, vol. 28, 627-640, 1990.
- [23] E. Rodríguez and J. M. Martin, "Theory and design of interferometric synthetic-aperture radars," *Proc. IEE*, vol. 139, no. 2, 147-159, 1992.
- [24] E. Rodríguez, D. Imel, and S. N. Madsen, "The accuracy of airborne interferometric SAR's," Originally submitted to *IEEE Trans. Aerospace Electron. Syst.*, 1993, lost (sic), then resubmitted 1998.
- [25] P. A. Rosen, S. Hensley, H. A. Zebker, F. H. Webb, and E. J. Fielding, "Surface deformation and coherence measurements of Kilauea Volcano, Hawaii, from SIR-C radar interferometry," *J. Geophys. Res.* vol. 268, 1333-1336, 1996.
- [26] S. N. Madsen, J. M. Martin, and H. A. Zebker, "Analysis and evaluation of the NASA/JPL TOPSAR across-track interferometric SAR system," *IEEE Trans. Geosci. Rem. Sens.*, vol. 33, no. 2, 383-391.
- [27] Shuttle Radar Topography Mission System Functional Requirements Document.
- [28] D. C. Ghiglia and M. D. Pritt, "Two-dimensional phase unwrapping: theory, algorithms, and software," *Wiley-Interscience*, 1998.
- [29] D. C. Ghiglia and L.A. Romero, "Direct phase estimation from phase differences using fast elliptic partial differential equation solvers," *Opt. Lett.* vol. 15, 1107-1109, 1989.
- [30] D. C. Ghiglia and L. A. Romero, "Robust two-dimensional weighted and unweighted phase unwrapping that uses fast transforms and iterative methods," *J. Opt. Soc. Amer. A*, vol. 11, no. 1, 107-117, 1994.
- [31] G. Fornaro, G. Franceschetti, and R. Lanari, "Interferometric SAR phase unwrapping using Green's Formulation," *IEEE Trans. Geosci. Rem. Sen.*, vol. 34, no. 3. 720-727, 1996.
- [32] G. Fornaro, G. Franceschetti, and R. Lanari, "Interferometric SAR phase unwrapping techniques - a comparison," *J. Opt. Soc. Amer. A*, vol. 13, no. 12, 2355-2366, 1996.
- [33] Q. Lin, J. F. Vesecy, and H. A. Zebker, "New approaches to SAR interferometric processing," *IEEE Trans. Geosci. Rem. Sen.*, vol. 30, no. 3, 560-567, May 1992.
- [34] W. Xu and I. Cumming, "A region growing algorithm for InSAR phase unwrapping," *IEEE Trans. Geosci. Rem. Sens.*, vol 37, no. 1, 1999.
- [35] R. Kramer and O. Loffeld, "Presentation of an improved phase unwrapping algorithm based on Kalman filters combined with local slope estimation", *Fringe '96 ESA Workshop on Applications of ERS SAR Interferometry*, Zurich, 1996.
- [36] A. Ferretti, C. Prati, F. Rocca, and A. Monti Guarnieri, "Multibaseline SAR interferometry for automatic DEM reconstruction," *3rd ERS Symposium*, Florence, 1997.
- [37] T. J. Flynn, "Two-dimensional phase unwrapping with minimum weighted discontinuity," *J. Opt. Soc. Am.*, vol. 14, no. 10, 2692-2701, 1997.

- [38] M. Costantini, "A phase unwrapping method based on network programming," *Proc. Fringe '96 Workshop*, Zurich, Switzerland, pp 261-272, (www.fringe.geo.unizh.ch/frl/fringe96/papers/costantini), 1996.
- [39] M. Costantini, "A novel phase unwrapping method based on network programming," *IEEE Trans. Geosci. Rem. Sens.*, vol. 36, no. 3, 813-821, 1998.
- [40] C. Prati, M. Giani, and N. Leuratti, "SAR Interferometry: a 2-D phase unwrapping technique based on phase and absolute values informations," *Proc. of IGARRS 92*, 2043-2046, Washington, D.C.,
- [41] M. D. Pritt, "Phase unwrapping by means of multigrid techniques for interferometric SAR," *IEEE Trans. Geosci. Rem. Sens.*, vol. 34, no. 3, 728-738, 1996.
- [42] G. Fornaro, G. Franceschetti, R. Lanari, D. Rossi, and M. Tesauro, "Interferometric SAR phase unwrapping via the finite element method," *Proc. IEEE - Radar, Sonar, and Navigation*, in press.
- [43] D. C. Ghiglia and L. A. Romero, "Minimum L(p)-norm 2-dimensional phase unwrapping," *J. Opt. Soc. Am., Opt. Image Sci. Vis.*, vol. 13, no. 10, 1999-2013, 1996.
- [44] R. Bamler, N. Adam, and G. W. Davidson, "Noise-induced slope distortion in 2-D phase unwrapping by linear estimators with application to SAR interferometry," *IEEE Trans. Geosci. Rem. Sens.*, vol. 36, no. 3, 913-921, 1998.
- [45] G. W. Davidson and R. Bamler, "Multi-resolution phase unwrapping for SAR interferometry," *IEEE Trans. Geosci. Rem. Sens.*, vol. 37, 163-174, 1999.
- [46] H. A. Zebker, Y. P. Lu, "Phase unwrapping algorithms for radar interferometry - residue-cut, least-squares, and synthesis algorithms," *J. Opt. Soc. Am.*, vol. 15, no. 3, 586-598, 1998.
- [47] I. Joughin, D. Winebrenner, M. Fahnestock, R. Kwok, and W. Krabill, "Measurement of ice-sheet topography using satellite radar interferometry," *Journal of Glaciology*, vol. 42, no. 140, 1996.
- [48] S. N. Madsen, H. A. Zebker, and J. Martin, "Topographic Mapping Using Radar Interferometry: Processing Techniques", *IEEE Trans. Geosci. and Rem. Sens.*, vol. 31, no. 1, January 1993, 246-256.
- [49] S. N. Madsen, "On Absolute Phases Determination Techniques in SAR Interferometry", in *Algorithms for Synthetic Aperture Radar Imagery II*, Proc. SPIE 2487, 19-21 April 1995, Orlando, Florida, 393-401.
- [50] D. A. Imel, "Accuracy of the residual-delay absolute-phase algorithm," *IEEE Trans. Geosci. Rem. Sens.*, vol. 36, no. 1, 322-324, 1998.
- [51] S. N. Madsen, N. Skou, J. Granholm, K.W. Woelders, and E. L. Christensen, "A system for airborne SAR interferometry," *Intl. J. Elect. Comm.*, vol. 50(2) 106-111, 1996.
- [52] J. W. Goodman, *Statistical Optics*, Wiley-Interscience, 1985.
- [53] E. Born and E. Wolf, *Principles of Optics, Sixth Edition*, Pergamon Press, 1989.
- [54] H. Sorenson, *Parameter Estimation*, Marcel Dekker, Inc. 1980.
- [55] I. Joughin, D. P. Winebrenner, and D. B. Percival, "Probability density functions for multi-look polarimetric signatures," *IEEE Trans. Geosci. Rem. Sens.*, vol. 32, 562-574, 1994.
- [56] J.-S. Lee, K. W. Hoppel, S. A. Mango, and A. R. Miller, "Intensity and phase statistics of multilook polarimetric and interferometric SAR imagery," *IEEE Trans. Geosci. Rem. Sens.*, vol. 32, 1017-1028, 1992.
- [57] R. Touzi and A. Lopes, "Statistics of the Stokes parameters and the complex coherence parameters in one-look and multilook speckle fields," *IEEE Trans. Geosci. Rem. Sens.*, vol. 34, 519-531, 1996.
- [58] H. A. Zebker and J. Villasenor, "Decorrelation in interferometric radar echoes," *IEEE Trans. Geosci. Rem. Sens.*, vol. 30, 950-959, 1992.
- [59] F. Gatelli, A. M. Guarnieri, F. Parizzi, P. Pasquali, and C. Prati, *et al.*, "The wave-number shift in SAR interferometry," *IEEE Trans. Geosci. Rem. Sens.*, vol. 32, no. 4, 855-865, 1994.
- [60] A. L. Gray and P. J. Farris-Manning, "Repeat-pass interferometry with an airborne synthetic aperture radar," *IEEE Trans. Geosci. Rem. Sens.*, vol. 31, no. 1, 180-191, 1993.
- [61] D. R. Stevens, I. G. Cumming, and A. L. Gray, "Options for airborne interferometric SAR motion compensation," *IEEE Trans. Geosci. Rem. Sens.*, vol. 33, no. 2, 409-420, 1995.
- [62] R. M. Goldstein, "Atmospheric limitations to repeat-track radar interferometry," *Geophys. Res. Lett.*, vol. 22, 2517-2520, 1995.
- [63] D. Massonnet and K. L. Feigl, "Discrimination of geophysical phenomena in satellite radar interferograms," *Geophys. Res. Lett.*, vol. 22, no. 12, 1537-1540, 1995.
- [64] H. Tarayre, D. Massonnet, "Atmospheric propagation heterogeneities revealed by ERS-1 interferometry," *Geophys. Res. Lett.*, vol. 23, no. 9, 989-992, 1996.
- [65] H. A. Zebker, P. A. Rosen, and S. Hensley, "Atmospheric effects in interferometric synthetic aperture radar surface deformation and topographic maps," *J. Geophys. Res.*, vol. 102, 7547-7563, 1997.
- [66] S. Fujiwara, P.A. Rosen, M. Tobita, and M. Murakami, "Crustal deformation measurements using repeat-pass JERS-1 Synthetic Aperture Radar interferometry near the Izu peninsula, Japan" *J. Geophys. Res. Solid Earth*, vol. 103, no. B2, 2411-2426, 1998.
- [67] R. J. Bullock, R. Voles, A. Currie, H. D. Griffiths, and P.V. Brennan, "Two-look method for correction of roll errors in aircraft-borne interferometric SAR," *Electronics Letters*, vol. 33, no. 18, 1581-1583, 1997.
- [68] G. Solaas, F. Gatelli, and G. Campbell, "Initial testing of ERS tandem data quality for InSAR applications," *WWW address: <http://gds.esrin.esa.it/earthres1>*, 1996.
- [69] D. L. Evans, J. J. Plaut, and E. R. Stofan, "Overview of the Spaceborne Imaging Radar-C/X-Band Synthetic- Aperture Radar (SIR-C/X-SAR) missions," *Rem. Sens. Env.*, vol. 59, no. 2, 135-140, 1997.
- [70] R. Lanari, S. Hensley, and P. A. Rosen, "Chirp-Z transform based SPECAN approach for phase-preserving ScanSAR image generation," *IEE Proc. Radar, Sonar, Navig.*, vol. 145, no. 5, 1998.
- [71] A. Monti-Guarnieri and C. Prati, "ScanSAR focusing and interferometry," *IEEE Trans. Geosci. Rem. Sens.*, vol. 34, 1029-1038, 1996.
- [72] H. A. Zebker, S. N. Madsen, J. Martin, K. B. Wheeler, T. Miller, Y. Lou, G. Alberti, S. Vetrilla, and A. Cucci, "The TOPSAR interferometric radar topographic mapping instrument," *IEEE Trans. Geosci. Rem. Sens.*, vol. 30, 933-940, 1992.

- [73] P. J. Mougini-Mark and H. Garbeil, "Digital topography of volcanos from radar interferometry - an example from Mt. Vesuvius, Italy," *Bull. OF Volcanology*, vol. 55, no. 8, 566-570, 1993.
- [74] H. A. Zebker, T. G. Farr, R. P. Salazar, and T. H. Dixon, "Mapping the world's topography using radar interferometry - the TOPSAT mission," *Proc. IEEE*, vol. 82, no. 12, 1774-1786, 1994.
- [75] H. A. Zebker, C. L. Werner, P. A. Rosen, and S. Hensley, "Accuracy of topographic maps derived from ERS-1 interferometric radar," *IEEE Trans. Geosci. Rem. Sens.*, vol. 32, 823-836, 1994.
- [76] N. Marechal, "Tomographic formulation of interferometric SAR for terrain elevation mapping," *IEEE Trans. Geosci. Rem. Sens.*, vol. 33, no. 3, 726-739, 1995.
- [77] R. Lanari, G. Fornaro, D. Riccio, M. Migliaccio, and K. P. Papathanassiou, *et al.*, "Generation of digital elevation models by using SIR-C/X-SAR multifrequency two-pass interferometry - the Etna case study," *IEEE Trans. Geosci. Rem. Sens.*, vol. 34, no. 5, 1097-1114, 1996.
- [78] N. R. Izenberg, R. E. Arvidson, R. A. Brackett, S. S. Saatchi, G. R. Osburn, *et al.*, "Erosional and depositional patterns associated with the 1993 Missouri river floods inferred from SIR-C and TOPSAR radar data," *J. Geophys. Res. Planets*, vol. 101, no. E10, 23149-23167, 1996.
- [79] R. Kwok and M. A. Fahnestock, "Ice sheet motion and topography from radar interferometry," *IEEE Trans. Geosci. Rem. Sens.*, vol. 34, no. 1, 1996.
- [80] C. Real, R. I. Wilson, and T. P. McCrirk, "Suitability of airborne-radar topographic data for evaluating earthquake-induced ground failure hazards," *12th Int. Conf. on Appl. Geol. Rem. Sens.* Denver, CO, 1997.
- [81] S. Hensley and F. H. Webb, "Comparison of Long Valley TOPSAR data with Kinematic GPS measurements," *IGARSS Proceedings*, Pasadena, 1994.
- [82] H. A. Zebker, P. A. Rosen, R. M. Goldstein, A. Gabriel, and C. L. Werner, "On the derivation of coseismic displacement fields using differential radar interferometry: The Landers earthquake," *J. Geophys. Res.*, vol. 99, 19617-19634, 1994.
- [83] D. Massonnet, K. Feigl, M. Rossi, and F. Adragna, "Radar interferometric mapping of deformation in the year after the Landers earthquake," *Nature*, vol. 369, no. 6477, 227-230, 1994.
- [84] G. Peltzer, K. Hudnut, and K. Fiegl, "Analysis of coseismic surface displacement gradients using radar interferometry: new insights into the Landers earthquake," *J. Geophys. Res.*, vol. 99, 21971-21981, 1994.
- [85] G. Peltzer and P. Rosen, "Surface displacement of the 17 May 1993 Eureka Valley, California, earthquake observed by SAR interferometry," *Science*, vol. 268, 1333-1336, 1995.
- [86] D. Massonnet and K. Feigl, "Satellite radar interferometric map of the coseismic deformation field of the M=6.1 Eureka Valley, CA earthquake of May 17, 1993," *Geophys. Res. Lett.*, vol. 22, 1541-1544, 1995.
- [87] D. Massonnet, K.L. Feigl, H. Vadon, and M. Rossi, "Coseismic deformation field of the M=6.7 Northridge, California earthquake of January 17, 1994 recorded by 2 radar satellites using interferometry," *Geophys. Res. Lett.*, vol. 23, no. 9, 969-972, 1996.
- [88] B. Meyer, R. Armijo, D. Massonnet, J. B. Dechabalier, C. Delacourt, *et al.*, "The 1995 Grevena (northern Greece) earthquake - fault model constrained with tectonic observations and SAR interferometry," *Geophys. Res. Lett.*, vol. 23, no. 19, 2677-2680, 1996.
- [89] P. J. Clarke, D. Paradissis, P. Briole, P. C. England, B. E. Parsons, *et al.*, "Geodetic investigation of the 13 May 1995 Kozani-Grevena (Greece) earthquake," *Geophys. Res. Lett.*, vol. 24, no. 6, 707-710, 1997.
- [90] S. Ozawa, M. Murakami, S. Fujiwara, and M. Tobita, "Synthetic aperture radar interferogram of the 1995 Kobe earthquake and its geodetic inversion," *Geophys. Res. Lett.*, vol. 24, no. 18, 2327-2330, 1997.
- [91] E. J. Price and D. T. Sandwell, "Small-scale deformations associated with the 1992, Landers, California, earthquake mapped by synthetic aperture radar interferometry phase gradients," *J. Geophys. Res.* vol. 103, 27,001-27,016, 1998.
- [92] D. Massonnet, W. Thatcher and H. Vadon, "Detection of postseismic fault-zone collapse following the Landers earthquake," *Nature*, vol. 382, no. 6592, 612-616, 1996.
- [93] G. Peltzer, P. Rosen, F. Rogez, and K. Hudnut, "Postseismic rebound in fault step-overs caused by pore fluid flow," *Science*, vol. 273, 1202-1204, 1996.
- [94] P. Rosen, C. Werner, E. Fielding, S. Hensley, S. Buckley, and P. Vincent, "Aseismic creep along the San Andreas Fault northwest of Parkfield, California, measured by radar interferometry," *Geophys. Res. Lett.*, 25, no. 6, 825-828, 1998.
- [95] D. Massonnet, P. Briole, and A. Arnaud, "Deflation of Mount Etna monitored by spaceborne radar interferometry," *Nature*, vol. 375, 567-570, 1995b.
- [96] P. Briole, D. Massonnet, and C. Delacourt, "Postruptive deformation associated with the 1986-87 and 1989 lava flows of Etna detected by radar interferometry," *Geophys. Res. Lett.*, vol. 24, no. 1, 37-40, 1997.
- [97] Z. Lu, R. Fatland, M. Wyss, S. Li, J. Eichelberger, *et al.*, "Deformation of New-Trident volcano measured by ERS-1 SAR interferometry, Katmai-National-Park, Alaska," *Geophys. Res. Lett.*, vol. 24, no. 6, 695-698, 1997.
- [98] W. Thatcher and D. Massonnet, "Crustal deformation at Long Valley caldera, eastern California, 1992-1996 inferred from satellite radar interferometry," *Geophys. Res. Lett.*, vol. 24, no. 20, 2519-2522, 1997.
- [99] R. Lanari, P. Lundgren, and E. Sansosti, "Dynamic deformation of Etna volcano observed by satellite radar interferometry," *Geophys. Res. Lett.*, vol. 25, no. 10, 1541-1543, 1998.
- [100] D. Massonnet, T. Holzer, and H. Vadon, "Land subsidence caused by the East Mesa geothermal field, California, observed using SAR interferometry," *Geophys. Res. Lett.*, vol. 24, no. 8, 901-904, 1997.
- [101] D. L. Galloway, K. W. Hudnut, S. E. Ingebritsen, S. P. Phillips, G. Peltzer, F. Rogez, and P. A. Rosen, "Detection of aquifer system compaction and land subsidence using interferometric synthetic aperture radar, Antelope Valley, Mojave Desert, California," *Water Resources Res.*, vol. 34, no. 10, 2573-2585, 1998.
- [102] S. Jonsson, N. Adam, and H. Bjornsson, "Effects of subglacial geothermal activity observed by satellite radar interferometry," *Geophys. Res. Lett.*, vol. 25, no. 7, 1059-1062, 1998.
- [103] B. Fruneau, J. Achache, and C. Delacourt, "Observation and modeling of the Saint-Etienne de Tinee landslide using SAR interferometry," *Tectonophysics*, vol. 265, no. 3-4, 181-190, 1996.
- [104] F. Mantovani, R. Soeters, and C. J. Vanwesten, "Remote-sensing techniques for landslide studies and hazard zonation in Europe," *Geomorph.*, vol. 15, no. 3-4, 213-225, 1996.

- [105] C. Carnec, D. Massonnet, and C. King, "Two examples of the use of SAR interferometry on displacement- fields of small spatial extent," *Geophys. Res. Lett.*, vol. 23, no. 24, 3579-3582, 1996.
- [106] F. Sigmundsson, H. Vadon, and D. Massonnet, "Readjustment of the Krafla spreading segment to crustal rifting measured by satellite radar interferometry," *Geophys. Res. Lett.*, vol. 24, no. 15, 1843-1846, 1997.
- [107] H. Vadon and F. Sigmundsson, "Crustal deformation from 1992 to 1995 at the mid-atlantic ridge, southwest Iceland, mapped by satellite radar interferometry," *Science*, vol. 275, no. 5297, 193-197, 1997.
- [108] H. A. Zebker, P. A. Rosen, S. Hensley, and P. Mouganis-Mark, "Analysis of active lava flows on Kilauea volcano, Hawaii, using SIR-C radar correlation measurements," *Geology*, vol. 24, 495-498, 1996.
- [109] T. P. Yunck, "Coping with the atmosphere and ionosphere in precise satellite and ground positioning," Environmental effects on Spacecraft Positioning and Trajectories, *Geophysical Monograph 73, IUGG* vol. 13, 1-16, 1995.
- [110] R. A. Bindschadler (Ed.), *West Antarctic Ice Sheet Initiative, Vol. 1 Science and Impact Plan*, NASA Conf. Pub. 3115, 1991.
- [111] W. S. B. Paterson, *The Physics of Glaciers, 3rd Ed.* Oxford: Pergamon Press, 1994.
- [112] T. Johannesson, *Landscape of temperate ice caps*, Ph. D. Thesis, University of Washington, 1992.
- [113] R. H. Thomas, R. A. Bindschadler, R. L. Cameron, F. D. Carsey, B. Holt, T. J. Hughes, C. W. M. Swithinbank, I. M. Whillans, and H. J. Zwally, *Satellite remote sensing for ice sheet research*, NASA Tech. Memo. 86233, 32 pp, 1985.
- [114] T. A. Scambos, M. J. Dutkiewicz, J. C. Wilson, and R. A. Bindschadler, "Application of image cross-correlation to the measurement of glacier velocity using satellite image data," *Remote Sensing of the Environment*, vol. 42, 177-186, 1992.
- [115] J. G. Ferrigno, B. K. Lucchitta, K. F. Mullins, A. L. Allison, R. J. Allen, and W. G. Gould, "Velocity measurement and changes in position of Thwaites Glacier/iceberg tongue from aerial photography, Landsat images and NOAA AVHRR data," *Annals of Glaciology*, vol. 17, 239-244, 1993.
- [116] M. Fahnestock, R. Bindschadler, R. Kwok, and K. Jezek, "Greenland ice sheet surface properties and ice dynamics from ERS-1 SAR imagery," *Science*, vol. 262, 1530-1534, Dec. 3, 1993.
- [117] K. E. Mattar, A. L. Gray, M. van der Kooij, and P. J. Farris-Manning, "Airborne interferometric SAR results from mountainous and glacial terrain," *Proc. of IGARRS '94*, Pasadena, CA.
- [118] I. R. Joughin, *Estimation of Ice Sheet Topography and Motion Using Interferometric Synthetic Aperture Radar*, Ph. D. Thesis, University of Washington, 1995.
- [119] I. R. Joughin, D. P. Winebrenner, and M. A. Fahnestock, "Observations of ice-sheet motion in Greenland using satellite radar interferometry," *Geophysical Research Letters*, vol. 22, no. 5, 571-574, 1995.
- [120] E. Rignot, K. C. Jezek, and H. G. Sohn, "Ice flow dynamics of the Greenland ice sheet from SAR interferometry," *Geophysical Research Letters*, vol. 22, no. 5, 575-578, 1995.
- [121] I. Joughin, R. Kwok, and M. Fahnestock, "Estimation of Ice Sheet Motion Using Satellite Radar Interferometry: Method and Error Analysis with Application to the Humboldt Glacier, Greenland," *Journal of Glaciology*, vol. 42, no. 142, 1996.
- [122] I. Joughin, R. Kwok, M. Fahnestock. "Interferometric estimation of the three-Dimensional Ice-Flow Velocity Vector Using Ascending and Descending Passes," Submitted to *IEEE Trans. Geosci. Rem. Sens.*, October 1996.
- [123] I. Joughin, S. Tulaczyk, M. Fahnestock, and R. Kwok. "A Mini-Surge on the Ryder Glacier, Greenland Observed via Satellite Radar Interferometry," *Science*, vol. 274, 228-230, 1996.
- [124] E. Rignot, "Tidal motion, ice velocity, and melt rate of Petermann Gletscher, Greenland, measured from radar interferometry," *Journal of Glaciology*, vol. 42, no. 142, 1996.
- [125] E. Rignot, "Interferometric observations of Glaciar San Rafael, Chile," *Journal of Glaciology*, vol. 42, no. 141, 1996.
- [126] J. J. Mohr, N. Reeh, and S. N. Madsen, "Three-dimensional glacial flow and surface elevation measured with radar interferometry," *Nature*, vol. 391, no. 6664, 273-276, 1998.
- [127] P. Hartl, K. H. Thiel, X. Wu, C. Doake, and J. Sievers, "Application of SAR interferometry with ERS-1 in the Antarctic," *Earth Observation Quarterly*, no. 43, 1-4, 1994.
- [128] E. Rignot, S. P. Gogineni, W. B. Krabill, and S. Ekholm, "North and northeast Greenland ice discharge from satellite radar interferometry," *Science*, vol. 276, no. 5314, 934-937, 1997.
- [129] E. Rignot, "Fast recession of a west Antarctic glacier," *Science*, vol. 281, 549-551, 1998.
- [130] I. Joughin, M. Fahnestock, R. Kwok, P. Gogineni, and C. Allen, "Ice flow of Humboldt, Petermann, and Ryder Gletscher, northern Greenland," *J. Glaciology*, vol. 45, no. 150, 231-241, 1999.
- [131] K. E. Mattar, P. W. Vachon, D. Geudtner, A. L. Gray, and I. G. Cumming, "Validation of alpine glacier velocity-measurements using ERS tandem-mission SAR data," *IEEE Trans. Geosci. Rem. Sens.*, vol. 36, no. 3, 974-984, 1998.
- [132] B. Unwin and D. Wingham, "Topography and dynamics of Austofana, Nordaustlandet, from SAR interferometry," *Annals of Glaciology*, 24 (in press).
- [133] D. R. Thompson and J. R. Jensen, "Synthetic aperture radar interferometry applied to ship-generated internal waves in the 1989 Loch Linnhe experiment," *J. Geophys. Res. Oceans*, vol. 98, no. C6, 10259-10269, 1993.
- [134] H. C. Graber, D. R. Thompson, and R. E. Carande, "Ocean surface features and currents measured with synthetic aperture radar interferometry and HF radar," *J. Geophys. Res. Oceans*, vol. 101, no. C11, 25813-25832, 1996.
- [135] M. Bao, C. Brünig, and W. Alpers, "Simulation of ocean waves imaging by an along-track interferometric synthetic aperture radar," *IEEE Trans. Geosci. Rem. Sens.*, vol. 35, 618-631, 1997.
- [136] R. M. Goldstein, T. P. Barnett, and H. A. Zebker, "Remote Sensing of Ocean Currents," *Science*, 1282-1285, 1989.
- [137] J. I. H. Askne, P. B. G. Dammert, L. M. H. Ulander, and G. Smith, "C-band repeat-pass interferometric SAR observations of the forest," *IEEE Trans. Geosci. Rem. Sens.*, vol. 35, no. 1, 25-35, 1997.
- [138] J. O. Hagberg, L. M. H. Ulander, and J. Askne, "Repeat-pass SAR interferometry over forested terrain," *IEEE Trans. Geosci. Rem. Sens.*, vol. 33, no. 2, 331-340, 1995.
- [139] E. Rodríguez, T. Michel, D. Harding, and J. M. Martin, "Comparison of airborne InSAR-derived heights and laser altimetry," *Radio Science*, in press, 1999.
- [140] E. Rodríguez, J. M. Martin, T. Michel, "Classification studies using Interferometry," *Radio Science*, in press, 1999.
- [141] R. N. Treuhaft, S. N. Madsen, M. Moghaddam, J. J. van Zyl, "Vegetation characteristics and underlying topography from interferometric radar," *Radio Science*, vol. 31, 1449-1485, 1997.

- [142] U. Wegmuller and C. L. Werner, "SAR interferometric signatures of forest," *IEEE Trans. Geosci. Rem. Sens.*, vol. 33, no. 5, 1153-1161, 1995.
- [143] U. Wegmuller and C. L. Werner, "Retrieval of vegetation parameters with SAR interferometry," *IEEE Trans. Geosci. Rem. Sens.*, vol. 35, no. 1, 18-24, 1997.
- [144] S. R. Cloude and K. P. Papathanassiou, "Polarimetric optimization in radar interferometry," *Electronics Letters*, vol. 33, no. 13, 1176-1178, 1997.

Additional References

General

- [145] R. Bindshadler, "Monitoring ice-sheet behavior from space," *Reviews of Geophysics*, vol. 36, no. 1, 79-104, 1998.
- [146] A. Freeman, D. L. Evans, J. J. van Zyl, "SAR applications in the 21st-century," *Int. J. Electr. Comm.*, vol. 50, no. 2, 79-84, 1996.
- [147] D. Massonnet and T. Rabaute, "Radar interferometry - Limits and potential," *IEEE Trans. Geosci. Rem. Sens.*, vol. 31, no. 2, 455-464, 1993.
- [148] D. Massonnet, "Application of remote-sensing data in earthquake monitoring," *Adv. Space Res.*, vol. 15, no. 11, 37-44, 1995.
- [149] D. Massonnet, "Tracking the Earth's surface at the centimeter level - an introduction to radar interferometry," *Nature and Resources*, vol. 32, no. 4, 20-29, 1996.
- [150] D. Massonnet, "Satellite radar interferometry," *Scientific American*, vol. 276, no. 2, 46-53, 1997.
- [151] C. Meade and D. T. Sandwell, "Synthetic aperture radar for geodesy," *Science*, vol. 273, no. 5279, 1181-1182, 1996.
- [152] H. Ohkura, "Application of SAR data to monitoring earth surface changes and displacement," *Adv. in Space Res.*, vol. 21, no. 3, 485-492, 1998.

Theory

- [153] R. K. Goyal and A. K. Verma, "Mathematical formulation for estimation of base-line in synthetic-aperture radar interferometry," *Sadhana Academy Proc. Eng. Sci.*, vol. 21, 511-522, 1996.
- [154] L. Guerriero, G. Nico, G. Pasquariello, and S. Stramaglia, "New regularization scheme for phase unwrapping," *Applied Optics*, vol. 37, no. 14, 3053-3058, 1998.
- [155] D. Just and R. Bamler, "Phase statistics of interferograms with applications to synthetic aperture radar," *Appl. Opt.*, vol. 33, no. 20, 4361-4368, 1994.
- [156] R. Kramer and O. Loffeld, "A novel procedure for cutline detection," *Intl. J. Elect. Comm.*, vol. 50, no. 2, 112-116, 1996.
- [157] J. L. Marroquin, M. Tapia, R. Rodriguezvera, and M. Servin, "Parallel algorithms for phase unwrapping based on Markov random-field models," *J. Opt. Soc. Amer. A*, vol. 12, no. 12, 2578-2585, 1995.
- [158] J. L. Marroquin and M. Rivera, "Quadratic regularization functionals for phase unwrapping," *J. Opt. Soc. Amer. A*, vol. 12, no. 11, 2393-2400, 1995.
- [159] K. A. Stetson, J. Wahid, and P. Gauthier, "Noise-immune phase unwrapping by use of calculated wrap regions," *Appl. Opt.*, vol. 36, no. 20, 4830-4838, 1997.
- [160] M. Facchini and P. Zanetta, "Derivatives of displacement obtained by direct manipulation of phase-shifted interferograms," *Appl. Opt.*, vol. 34, no. 31, 7202-7206, 1995.

Systems and Techniques

- [161] R. Bamler and M. Eineder, "SCANSAR processing using standard high-precision SAR algorithms," *IEEE Trans. Geosci. Rem. Sens.*, vol. 34, no. 1, 212-218, 1996.
- [162] C. Cafforio, C. Prati, and F. Rocca, "SAR focussing using seismic migration techniques," *IEEE Trans. Aero. Elec. Sys.*, vol. 27, 194-207, 1991.
- [163] S. L. Durden and C. L. Werner, "Application of an interferometric phase unwrapping technique to dealiasing of weather radar velocity-fields," *J. Atm. Ocean. Tech.*, vol. 13, no. 5, 1107-1109, 1996.
- [164] G. Fornaro and G. Franceschetti, "Image registration in interferometric SAR processing," *IEE Proc. Radar Sonar and Nav.*, vol. 142, no. 6, 313-320, 1995.
- [165] G. Fornaro, V. Pascazio, and G. Schirinzi, "Synthetic-aperture radar interferometry using one bit coded raw and reference signals," *IEEE Trans. Geosci. Rem. Sens.*, vol. 35, no. 5, 1245-1253, 1997.
- [166] G. Franceschetti, A. Iodice, M. Migliaccio, and D. Riccio, "A novel across-track SAR interferometry simulator," *IEEE Trans. Geosci. Rem. Sens.*, vol. 36, no. 3, 950-962, 1998.
- [167] A. M. Guarnieri and C. Prati, "SCANSAR focusing and interferometry," *IEEE Trans. Geosci. Rem. Sens.*, vol. 3, no. 4, 1029-1038, 1996.
- [168] R. M. Goldstein and C. L. Werner, "Radar interferogram filtering for geophysical applications," *Geophys. Res. Lett.*, vol. 25, no. 21, 4035-4038, 1998.
- [169] A. M. Guarnieri and C. Prati, "SAR interferometry - a quick and dirty coherence estimator for data browsing," *IEEE Trans. Geosci. Rem. Sens.*, vol. 35, no. 3, 660-669, 1997.
- [170] C. Ichoku, A. Karnieli, Y. Arkin, J. Chorowicz, T. Fleury, et al., "Exploring the utility potential of SAR interferometric coherence images," *Intl. J. Rem. Sens.*, vol. 19, no. 6, 1147-1160, 1998.
- [171] D. Massonnet and H. Vadon, "ERS-1 internal clock drift measured by interferometry," *IEEE Trans. Geosci. Rem. Sens.*, vol. 33, no. 2, 401-408, 1995.
- [172] D. Massonnet, H. Vadon, and M. Rossi, "Reduction of the need for phase unwrapping in radar interferometry," *IEEE Trans. Geosci. Rem. Sens.*, vol. 34, no. 2, 489-497, 1996.
- [173] I. H. Mcleod, I. G. Cumming, and M. S. Seymour, "ENVISAT ASAR data reduction - impact on SAR interferometry," *IEEE Trans. Geosci. Rem. Sens.*, vol. 36, no. 2, 589-602, 1998.
- [174] A. Moccia, M. Derrico, and S. Vetrella, "Space station based tethered interferometer for natural disaster monitoring," *J. Spacecraft Rockets*, vol. 33, no. 5, 700-706, 1996.
- [175] C. Prati and F. Rocca, "Improving slant range resolution with multiple SAR surveys," *IEEE Trans. Aerospace Elec. Sys.*, vol. 29, 135-143, 1993.
- [176] M. Rossi, B. Rogron, and D. Massonnet, "JERS-1 SAR image quality and interferometric potential," *IEEE Trans. Geosci. Rem. Sens.*, vol. 34, no. 3, 824-827, 1996.

- [177] K. Sarabandi, "Delta-k-radar equivalent of interferometric SARs - A theoretical-study for determination of vegetation height," *IEEE Trans. Geosci. Rem. Sens.*, vol. 35, no. 5, 1267-1276, 1997.
- [178] D. L. Schuler, J. S. Lee, and G. Degrandi, "Measurement of topography using polarimetric SAR images," *IEEE Trans. Geosci. Rem. Sens.*, vol. 34, no. 5, 1266-1277, 1996.
- [179] E. R. Stofan, D. L. Evans, C. Schmullius, B. Holt, and J. J. Plaut, *et al.*, "Overview of results of Spaceborne Imaging Radar-C, X-Band Synthetic Aperture Radar (SIR-C/X-SAR)," *IEEE Trans. Geosci. Rem. Sens.*, vol. 33, no. 4, 817-828, 1995.
- [180] E. Trouve, M. Caramma, and H. Maitre, "Fringe detection in noisy complex interferograms," *Appl. Opt.*, vol. 35, no. 20, 3799-3806, 1996.

Applications

- [181] M. Coltelli, G. Fornaro, G. Franceschetti, R. Lanari, M. Migliaccio, *et al.*, "SIR-C/X-SAR multifrequency multipass interferometry - a new tool for geological interpretation," *J. Geophys. Res. Planets*, vol. 101, no. E10, 23127-23148, 1996.
- [182] M. Derrico, A. Moccia, and S. Vetrella, "High-frequency observation of natural disasters by SAR interferometry," *Phot. Eng. Rem. Sens.*, vol. 61, no. 7, 891-898, 1995.
- [183] S. Ekholm, "A full coverage, high-resolution, topographic model of Greenland computed from a variety of digital elevation data," *J. Geophys. Res. Solid Earth*, vol. 101 no. B10, 21961-21972, 1996.
- [184] L. V. Elizavetin and E. A. Ksenofontov, "Feasibility of precision-measurement of the earth's surface- relief using SAR interferometry data," *Earth Obs. Rem. Sens.*, vol. 14, no. 1, 101-121, 1996.
- [185] J. Goldhirsh and J. R. Rowland, "A tutorial assessment of atmospheric height uncertainties for high-precision satellite altimeter missions to monitor ocean currents," *IEEE Geosci. Rem. Sens.* vol. 20, 418-434, 1982.
- [186] B. Hernandez, F. Cotton, M. Campillo, and D. Massonnet, "A comparison between short-term (coseismic) and long-term (one-year) slip for the Landers earthquake - measurements from strong-motion and SAR interferometry," *Geophys. Res. Lett.*, vol. 24, no. 13, 1579-1582, 1997.
- [187] S. S. Li, C. Benson, L. Shapiro, and K. Dean, "Aufeis in the Ivishak river, Alaska, mapped from satellite radar interferometry," *Rem. Sens. Env.*, vol. 60, no. 2, 131-139, 1997.
- [188] J. Moreira, M. Schwabisch, G. Fornaro, R. Lanari, and R. Bamler *et al.*, "X-SAR interferometry - first results," *IEEE Trans. Geosci. Rem. Sens.*, vol. 33, no. 4, 950-956, 1995.
- [189] P. J. Mouginiis-Mark, "Volcanic hazards revealed by radar interferometry," *Geotimes*, vol. 39, no. 7, 11-13, 1994.
- [190] H. Rott, M. Stuefer, A. Siegel, P. Skvarca, and A. Eckstaller, "Mass fluxes and dynamics of Moreno glacier, southern Patagonia icefield," *Geophys. Res. Lett.*, vol. 25, no. 9, 1407-1410, 1998.
- [191] S. K. Rowland, "Slopes, lava flow volumes, and vent distributions on Volcan- Fernandina, Galapagos-Islands," *J. Geophys. Res. Solid Earth*, vol. 101, no. B12, 27657-27672, 1996.

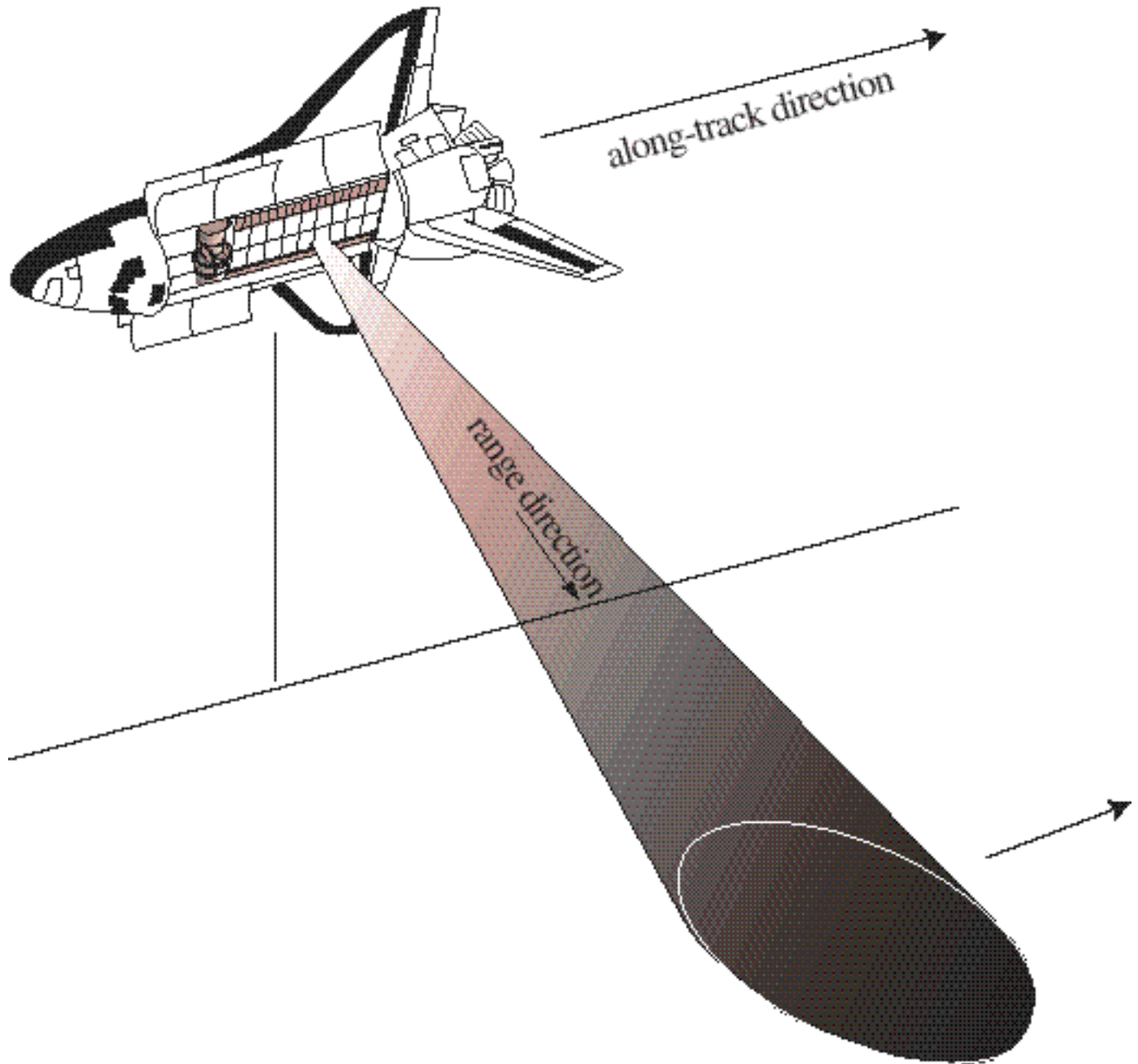


Figure 1: Typical imaging scenario for a SAR system, depicted here as a shuttle-borne radar. The platform carrying the SAR instrument follows a curvilinear track known as the “along-track,” or “azimuth,” direction. The radar antenna points to the side, imaging the terrain below. The distance from the aperture to a target on the surface in the look direction is known as the “range.” The “cross-track,” or range, direction is defined along by the range, and is terrain dependent.

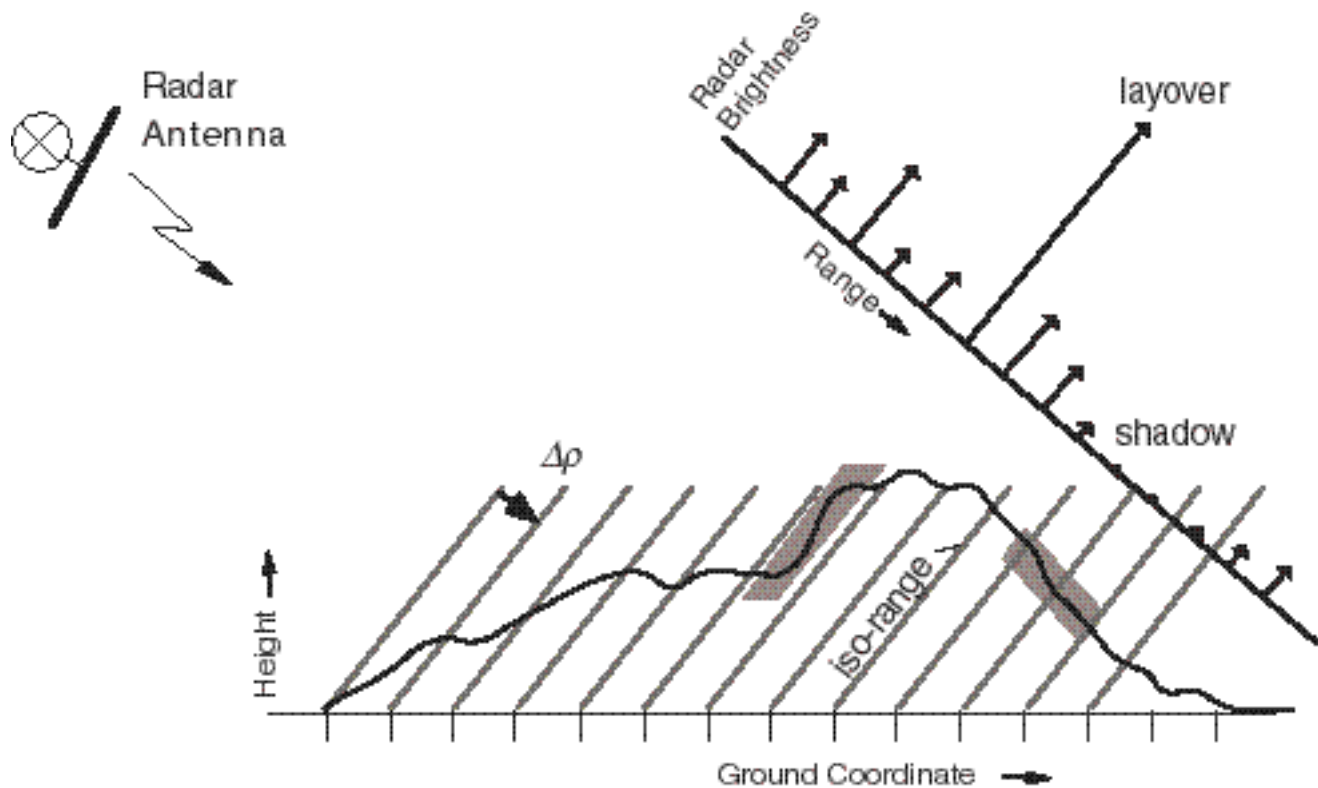


Figure 2: The three-dimensional world is collapsed to two dimensions in conventional SAR imaging. After image formation, the radar return is resolved into an image in range-azimuth coordinates. This figure shows a profile of the terrain at constant azimuth, with the radar flight track into the page. The profile is cut by curves of constant range, spaced by the range resolution of radar, defined as $\Delta\rho = c/2\Delta f_{BW}$, where c is the speed of light and Δf_{BW} is the range bandwidth of the radar. The backscattered energy from all surface scatterers within a range resolution element contribute to the radar return for that element.

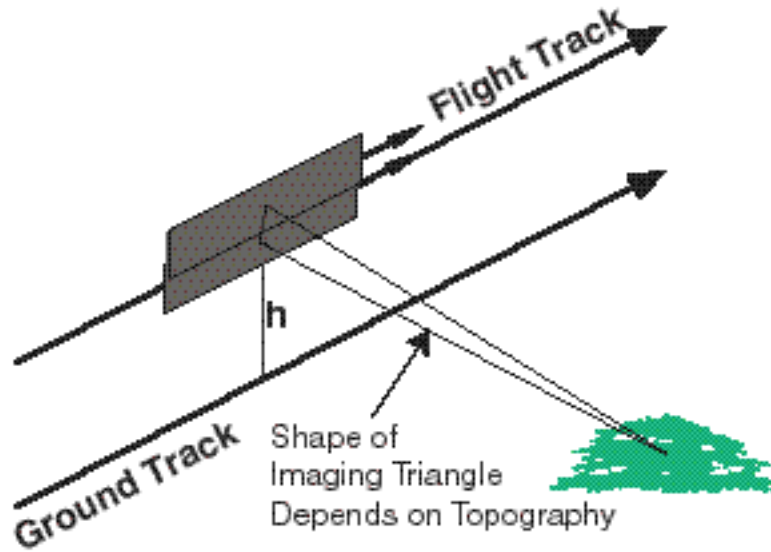


Figure 3: Interferometric SAR for topographic mapping uses two apertures separated by a “baseline” to image the surface. The phase difference between the apertures for each image point, along with the range and knowledge of the baseline, can be used to infer the precise shape of the imaging triangle to derive the topographic height of the image point.

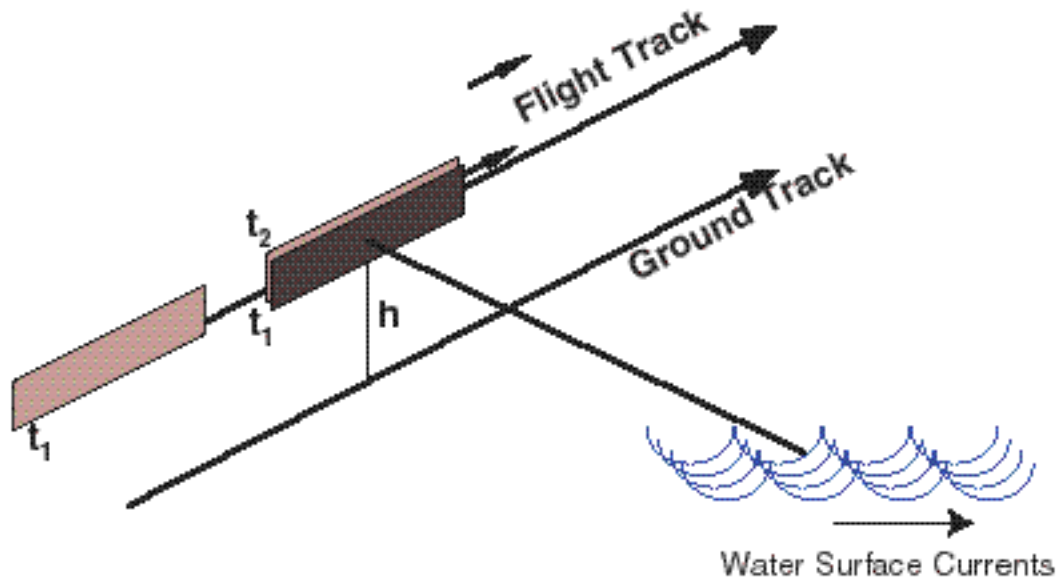


Figure 4: An along track interferometer maintains a baseline separated along the flight track such that surface points are imaged by each aperture within one second. Motion of the surface over the elapsed time is recorded in the phase difference of the pixels.

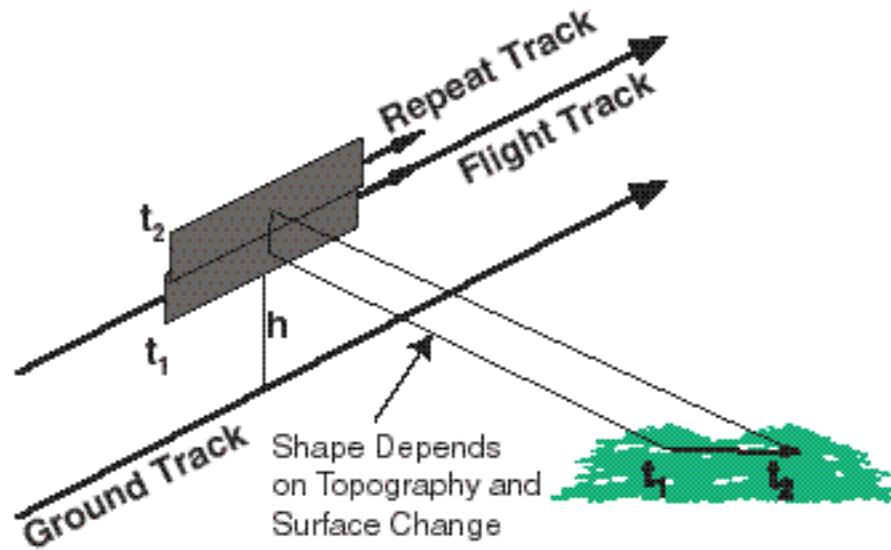


Figure 5: A repeat track interferometer is similar to an along track interferometer. An aperture repeats its track and precisely measures motion of the surface between observations in the image phase difference. If the track does not repeat at exactly the same location, some topographic phase will also be present, which must be removed by the methods of differential interferometry to isolate the motion.

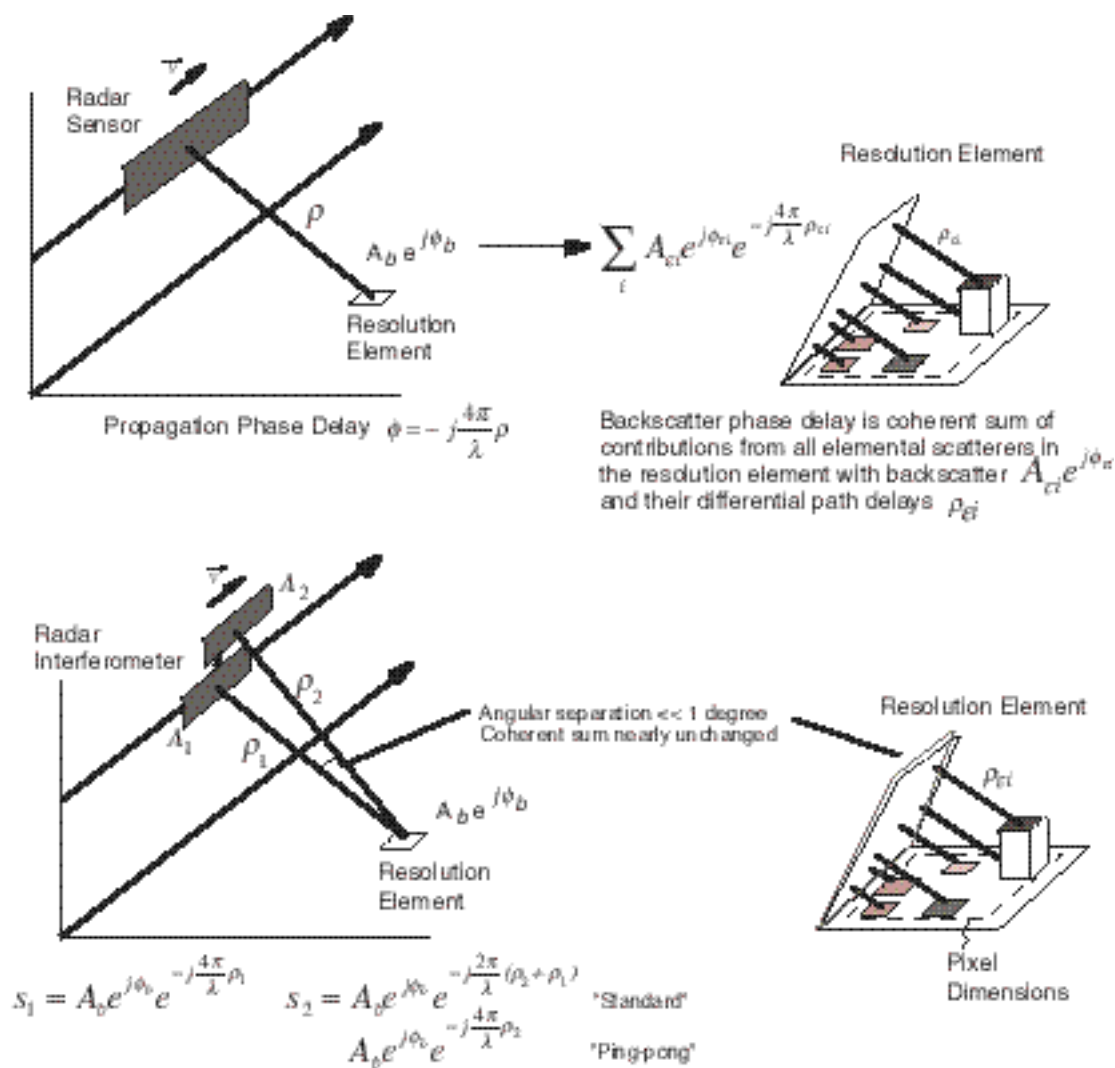


Figure 7: The interferometric phase difference is mostly due to the propagation delay difference. The (nearly) identical coherent phase from the different scatterers inside a resolution cell (mostly) cancels out during interferogram formation.

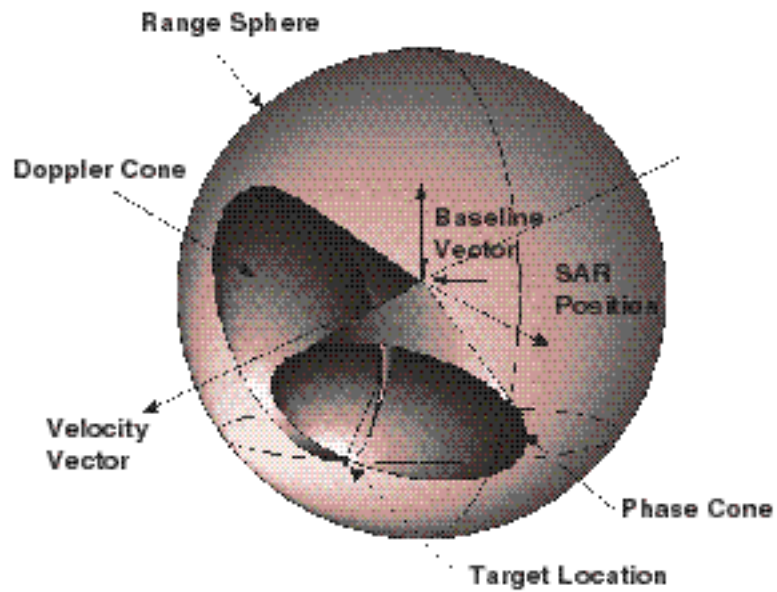


Figure 6: Target location in an InSAR image is precisely determined by noting that the target location is the intersection of the range sphere, doppler cone and phase cone.

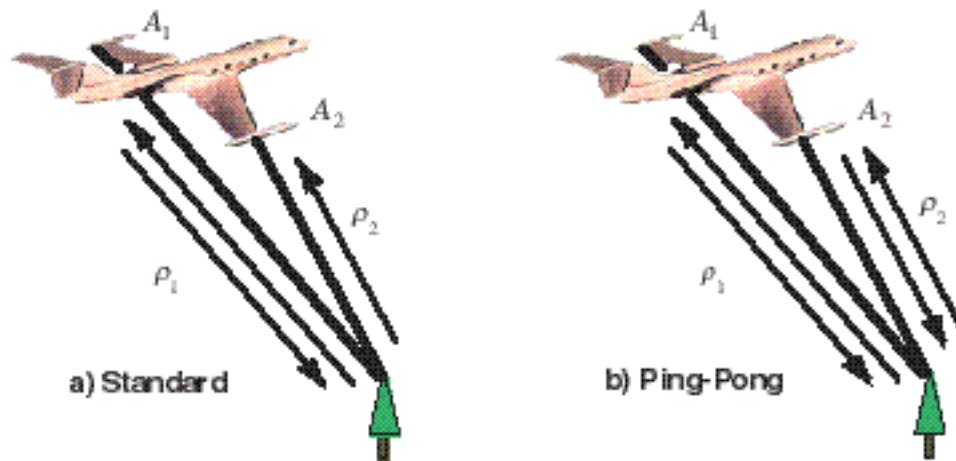


Figure 8: Illustration of standard *vs.* ping-pong mode of data collection. In standard mode, the radar transmits a signal out of one of the interferometric antennas only, and receives the echoes through both antennas A_1 and A_2 simultaneously. In “ping-pong” mode, the radar transmits alternatively out of the top and bottom antennas and receives the radar echo only through the same antenna. Repeat-track interferometers are inherently in ping-pong mode.

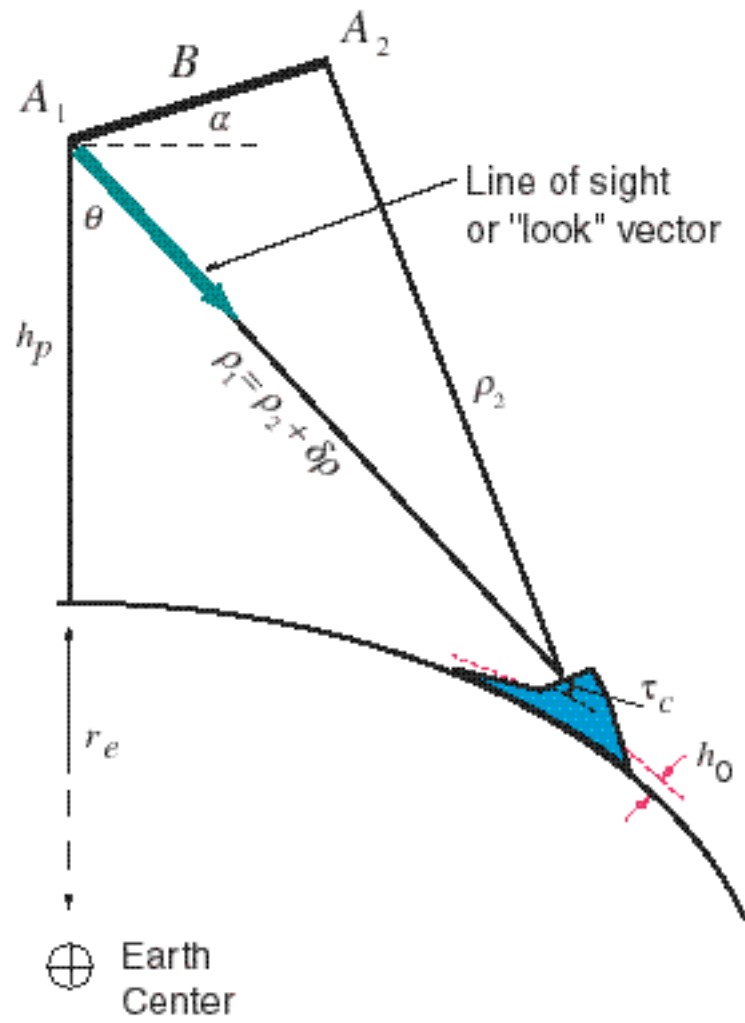


Figure 9: SAR interferometry imaging geometry in the plane normal to the flight direction.

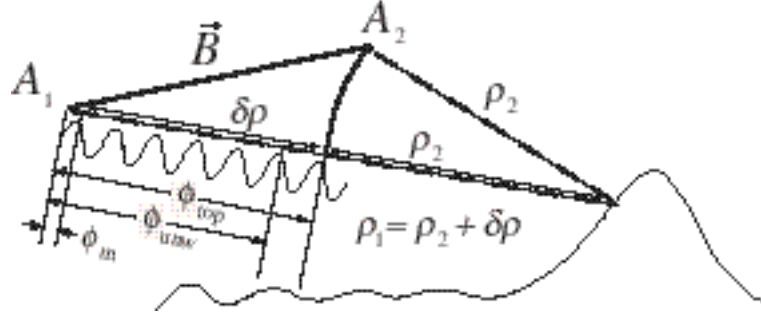


Figure 10: Phase in interferogram depicted as cycles of electromagnetic wave propagating a differential distance $\delta\rho$ for the case $p = 1$. Phase in the interferogram is initially known modulo 2π : $\phi_m = W(\phi_{\text{top}})$, where ϕ_{top} is the topographically induced phase and $W()$ is an operator that wraps phase values into the range $-\pi < \phi \leq \pi$. After unwrapping, relative phase measurements between all pixels in the interferogram are determined up to a constant multiple of 2π : $\phi_{\text{unw}} = \phi_m + 2\pi k_{\text{unw}}(\rho_{1,ij}, s_{1,ij})$, where k_{unw} is a spatially variable integer and $\rho_{1,ij}$ and $s_{1,ij}$ are pixel coordinates corresponding to the range and azimuth location of the pixels in the reference image, from A_1 in this case. Absolute phase determination is the process to determine the overall multiple of $2\pi k_{\text{abs}}$ that must be added to the phase measurements so that it is proportional to the range difference. The reconstructed phase is then $\phi_{\text{top}} = \phi_m + 2\pi k_{\text{unw}} + 2\pi k_{\text{abs}}$.

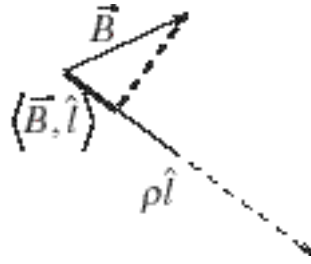


Figure 11: When the plane wave approximation is valid the range difference is approximately the projection of the baseline vector onto a unit vector in the line of sight direction.

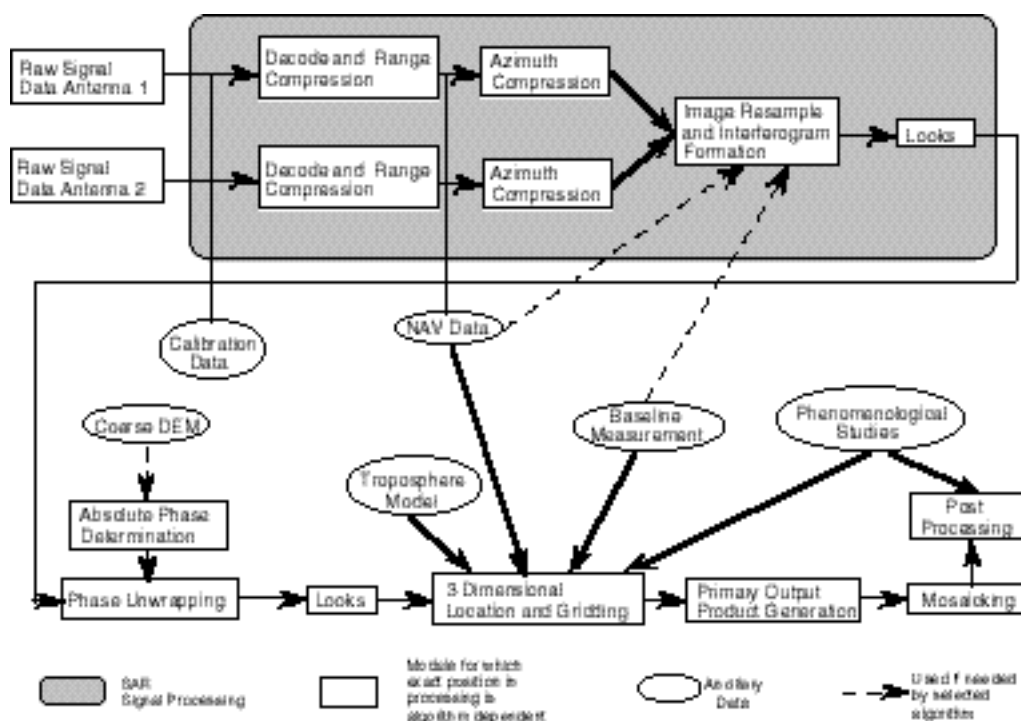


Figure 13: Block diagram showing the major steps in interferometric processing to generate topographic maps. Data for each interferometric channel are processed to full resolution images using the platform motion information to compensate the data for perturbations from a straight line path. One of the complex images is resampled to overlay the other, and an interferogram is formed by cross-multiplying images, one of which is conjugated. The resulting interferogram is averaged to reduce noise. Then, the principal value of the phase for each complex sample is computed. To generate a continuous height map, the two-dimensional phase field must be unwrapped. After the unwrapping process, an absolute phase constant is determined. Subsequently, the three dimensional target location is performed with corrections applied to account for tropospheric effects. A relief map is generated in a natural coordinate system aligned with the flight path. Gridded products may include the target heights, the SAR image, a correlation map, and a height error map.

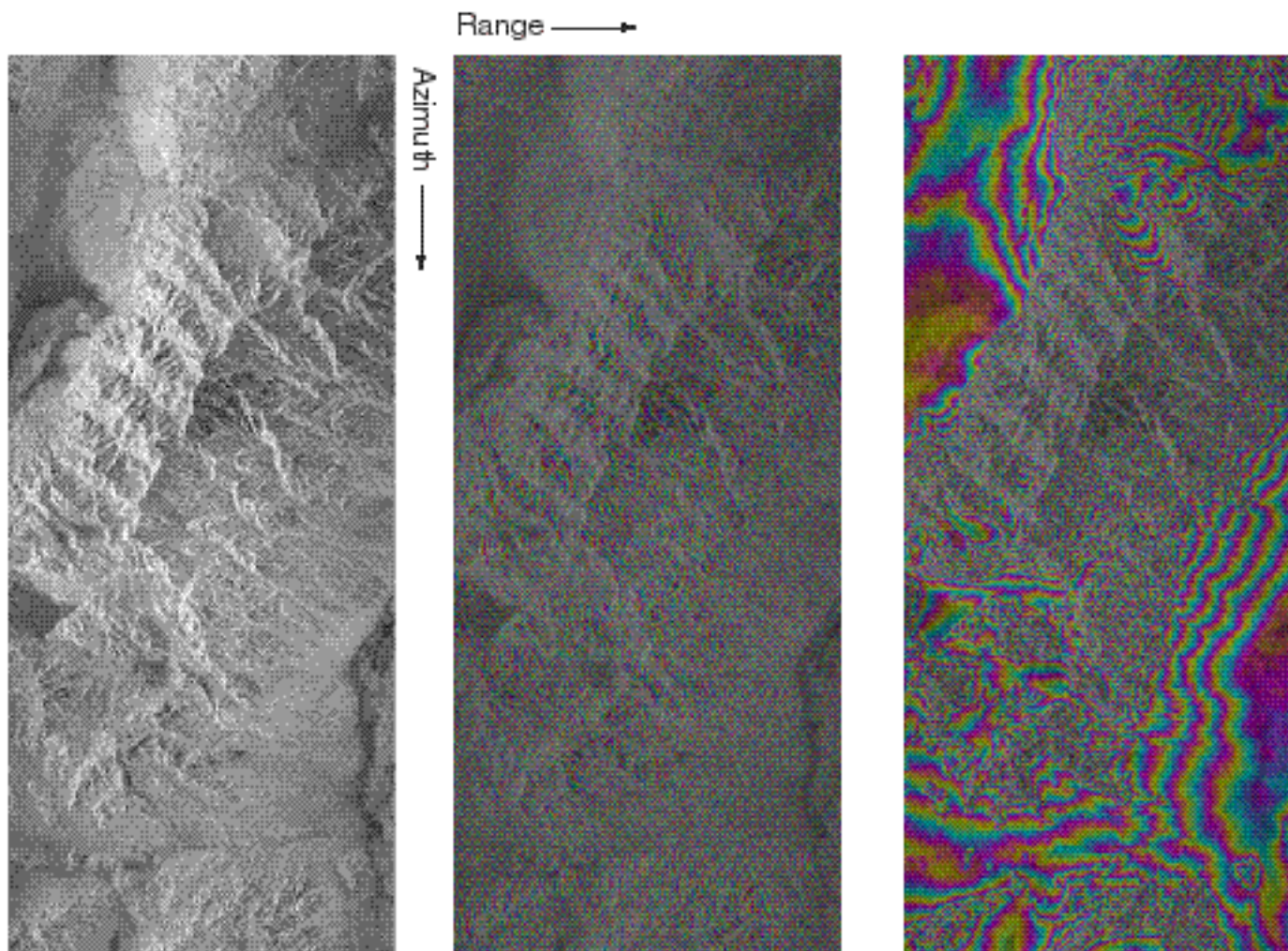


Figure 12: (a) Radar brightness image of Mojave desert near Fort Irwin, California derived from SIR-C C-band (5.6 cm wavelength) repeat-track data. The image extends about 20 km in range and 50 km in azimuth. (b) Phase of the interferogram of the area showing intrinsic fringe variability. The spatial baseline of the observations is about 70 m perpendicular to the line-of-sight direction. (c) Flattened interferometric phase assuming a reference surface at zero elevation above a spherical earth.

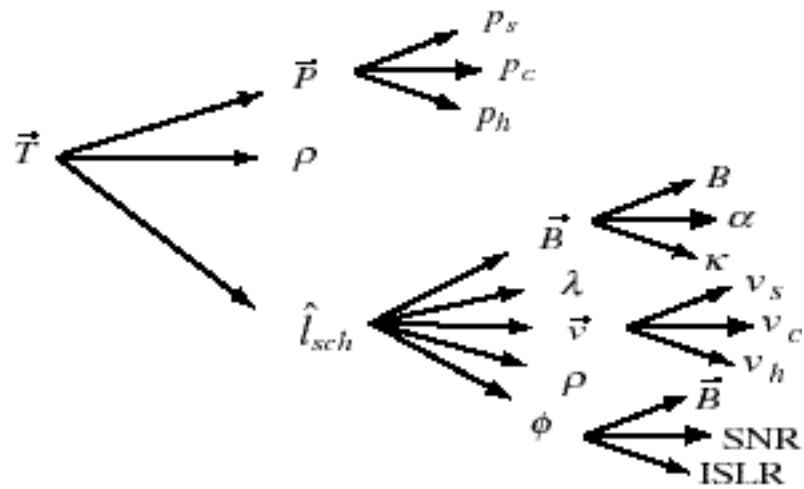


Figure 14: Sensitivity tree showing the sensitivity of target location to various parameters used in interferometric height reconstruction. See Fig. 15 for definitions of angles.

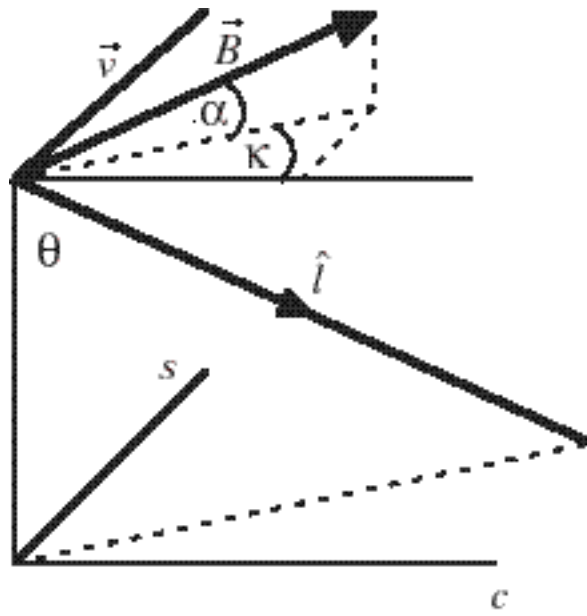


Figure 15: Baseline and look angle geometry as used in sensitivity formulas.

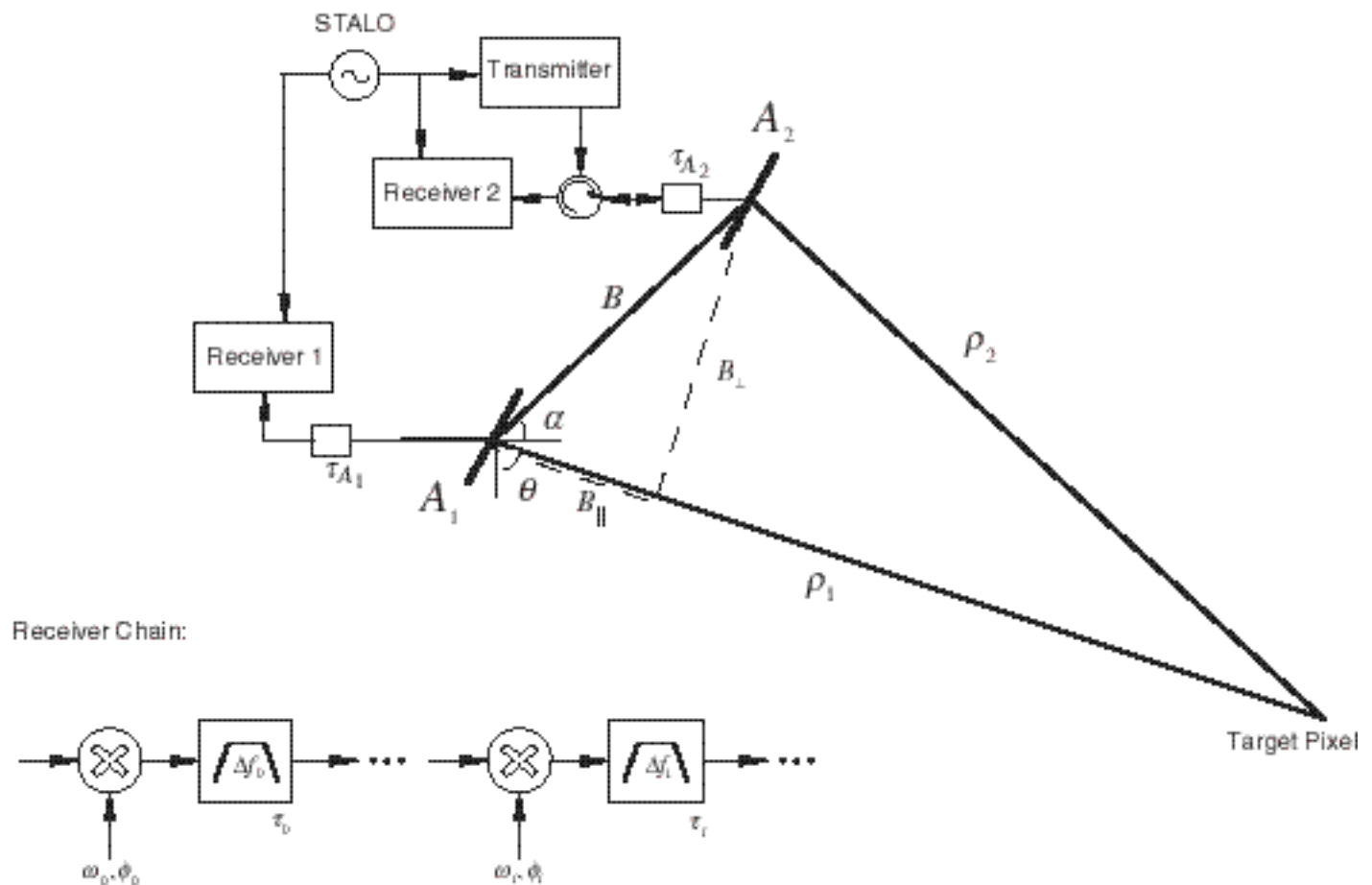


Figure 16: Definitions of interferometric parameters relating to a possible radar interferometer configuration. In this example, the transmitter path is common to both roundtrip signal paths. Therefore the transmitter phase and time delays cancel in the channel difference. The total delay is the sum of the antenna delay and the various receiver delays.

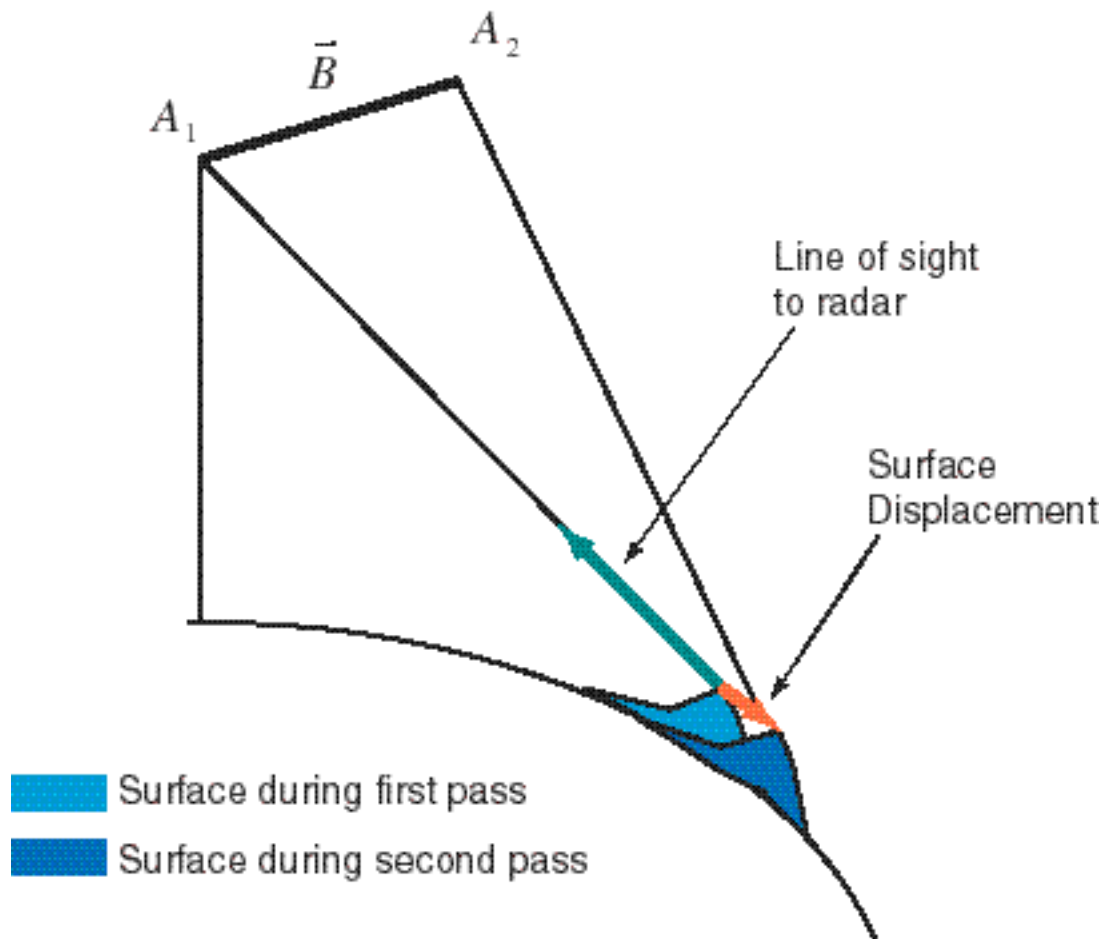


Figure 17: Geometry of displacement interferometry. Surface element has moved in a coherent fashion between the observation made at time t_1 and the observation made at time t_2 . The displacement can be of any sort - continuous or instantaneous, steady or variable - but the detailed scatterer arrangement must be preserved in the interval for coherent observation.

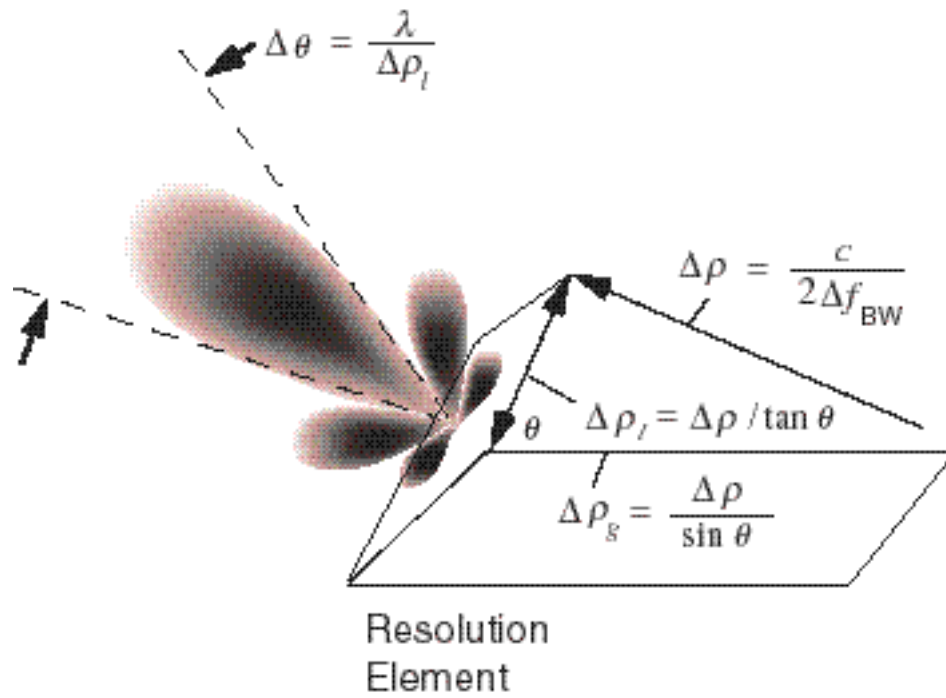


Figure 20: A view of baseline decorrelation showing the effective beam pattern of a ground resolution element “radiating” to space. The mutual coherence field propagates with radiation beamwidth in elevation of $\Delta\theta \approx \lambda/\Delta\rho_l$. These quantities are defined in the figure.

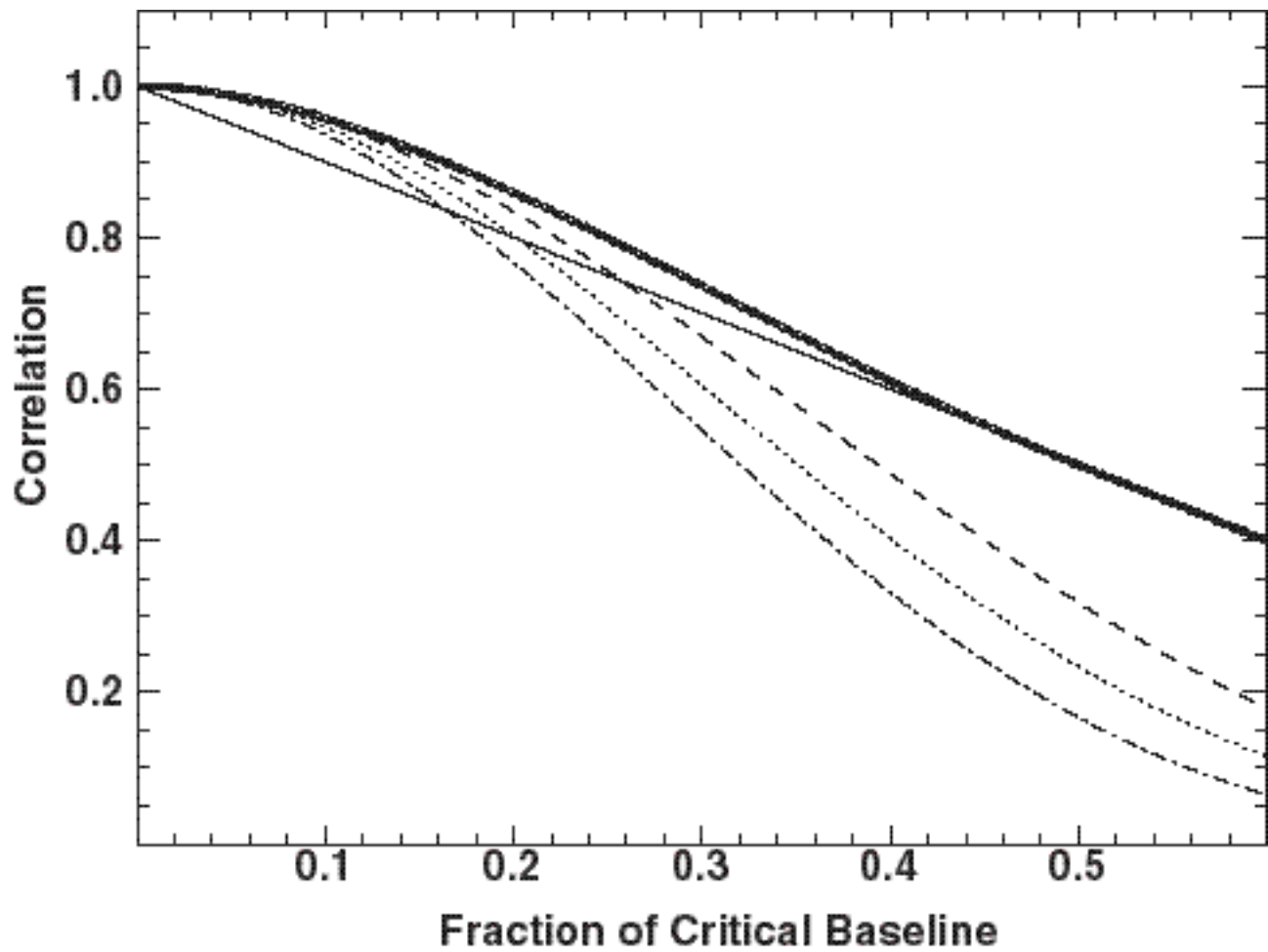


Figure 21: Baseline decorrelation for various point target response functions. The solid line is for standard sinc response with no weighting. The dashed, dot-dashed, dotted, and triangled lines are weightings of half-cosine, Hanning, Hamming, and optimized cosine, respectively.

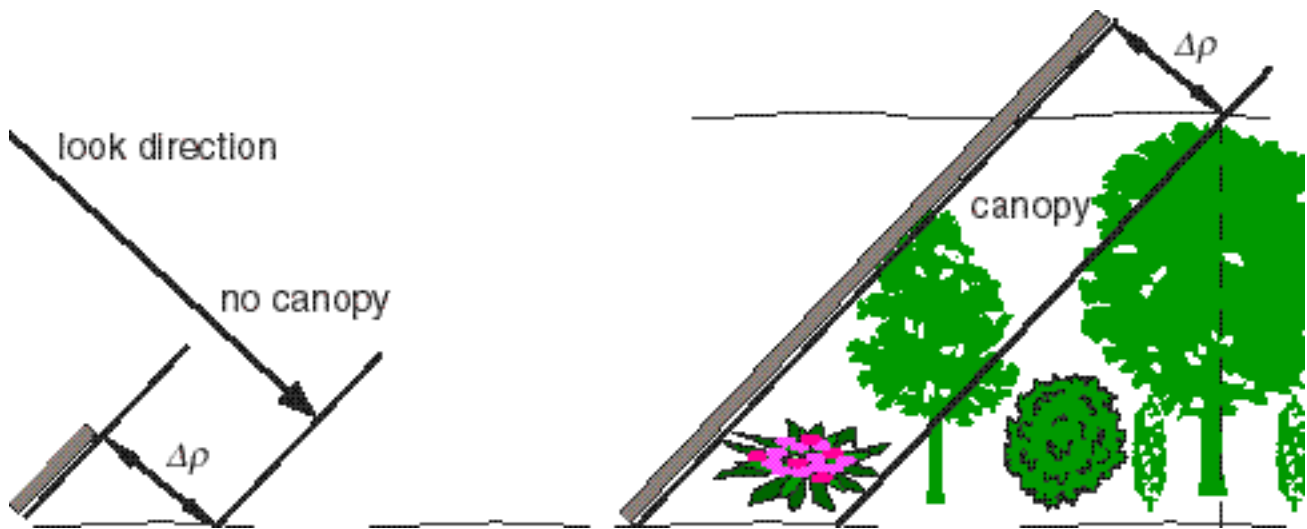


Figure 22: A view of volumetric decorrelation in terms of the effective radiating ground resolution element, showing the increase in the size of the projected range resolution cell $\Delta\rho_l$ (shaded boxes) as scattering from the volume contributes within a resolution cell.

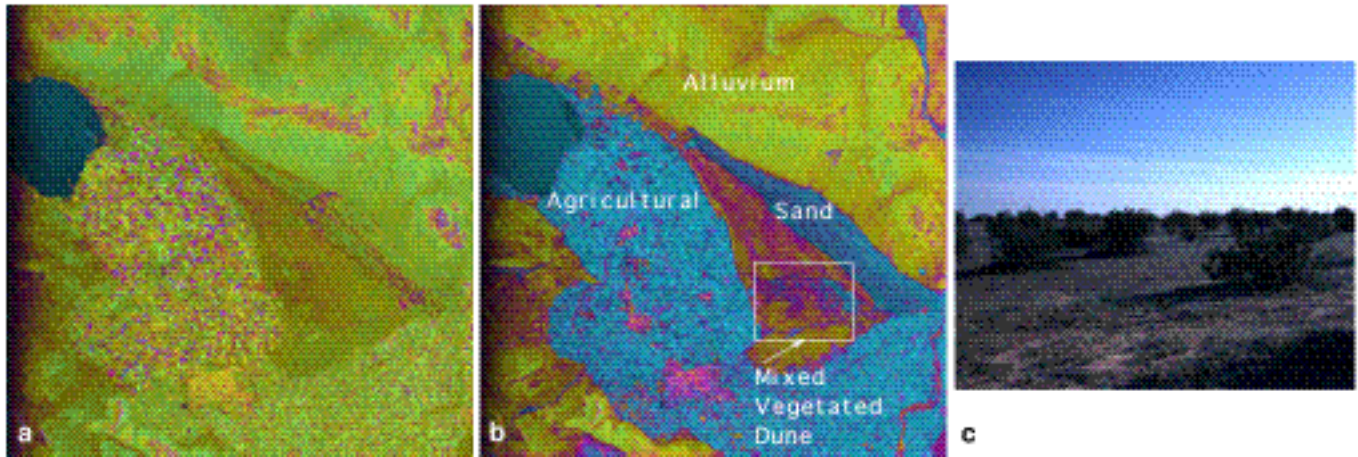


Figure 23: (a) Correlation image in radar coordinates of Algodones Dunefield, CA, measuring the sameness of the two images acquired one day apart used to form a radar interferogram. Blue color denotes low correlation, purple moderate correlation, and yellow-green high correlation. Salton Sea decorrelates because water changes from one second to the next. Some agricultural fields and dune areas decorrelate from over the one day period. Mountains decorrelate from baseline decorrelation effects on high slopes rather than temporal effects. Dunes remain well correlated in general over one day. (b) five month correlation map showing large decorrelation in the unvegetated Algodones dunes but significantly less in much of the vegetated area to the west (in box) (c) Ground photo of vegetated dune area in box.

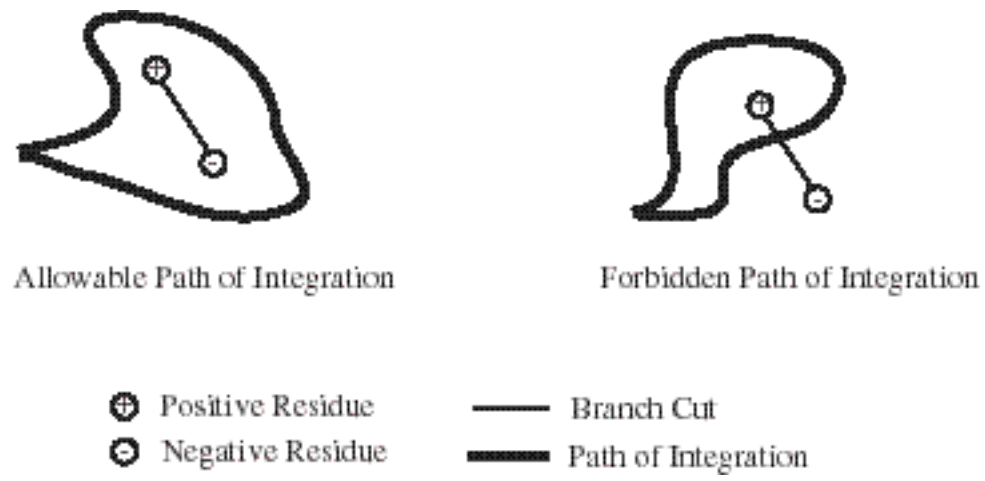


Figure 18: An example of a branch cut and allowable and forbidden paths of integration.

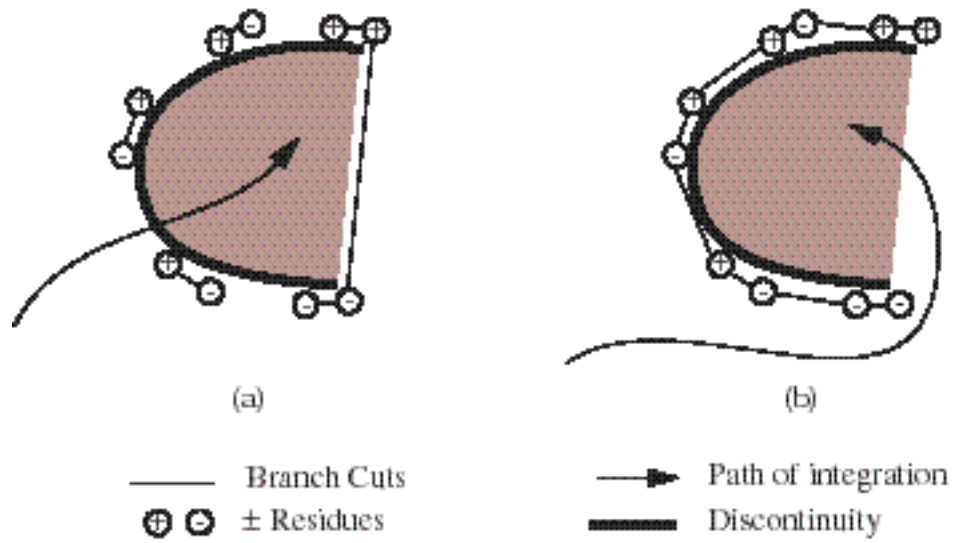


Figure 19: Cut dependencies of unwrapped phase. a) shortest path cuts b) better choice of cuts.

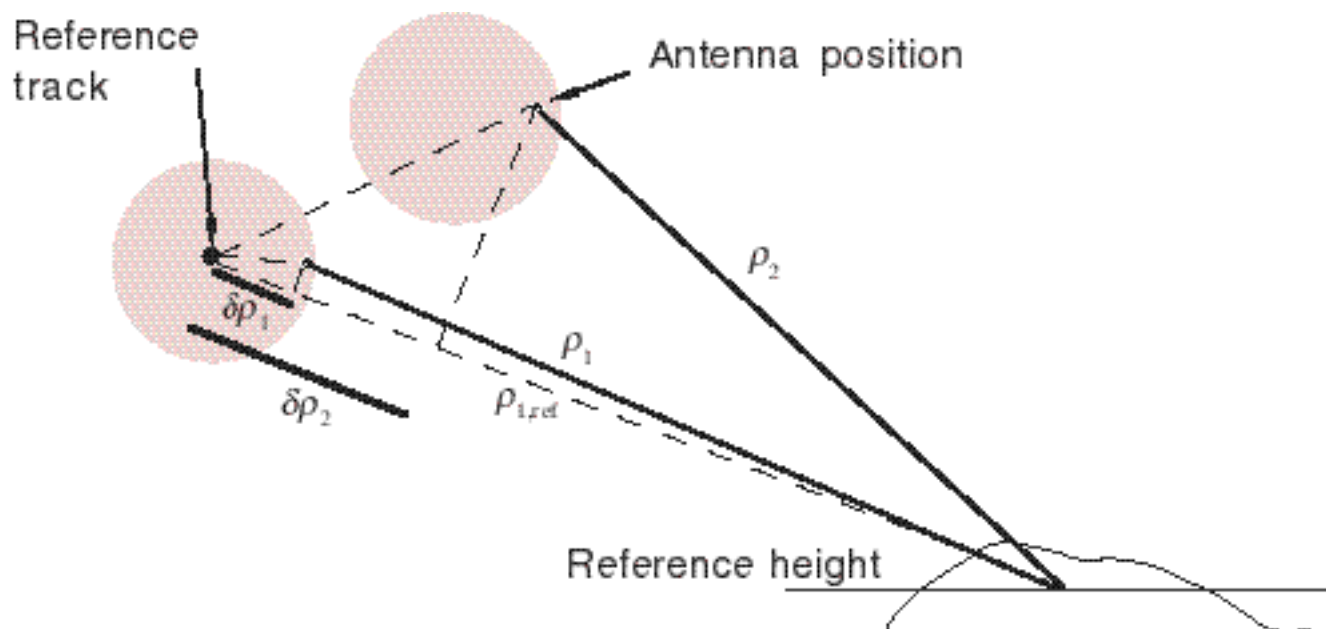


Figure 24: Single reference track motion compensation geometry illustrated for interferometry. Two wandering flight paths with motion into the paper are depicted schematically as shaded circles of possible antenna positions, with the antennas at a particular instant shown as small white circles. In the single reference track approach, an idealized reference track, chosen here as the centroid of the possible positions of Antenna 1 (but not restricted so), is defined. For an assumed reference height, a range correction for each antenna can be assigned as in the figure at each time instant to compensate for the motion.

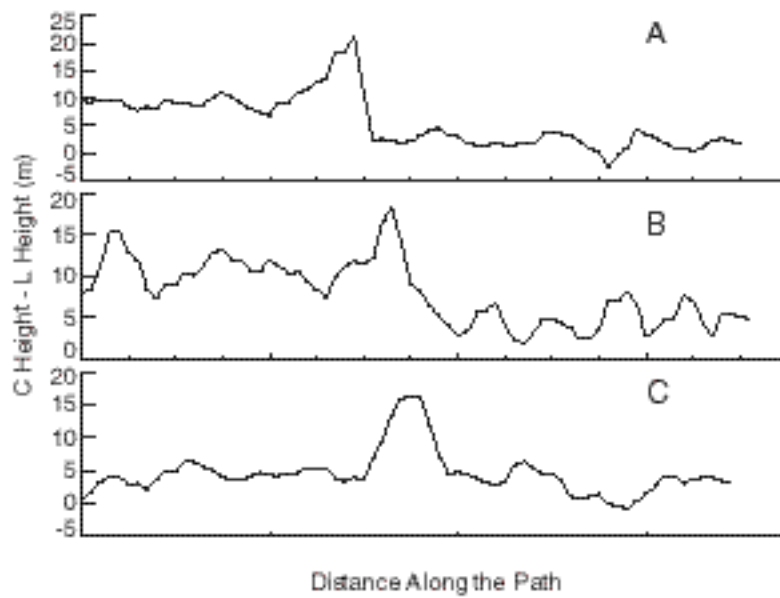
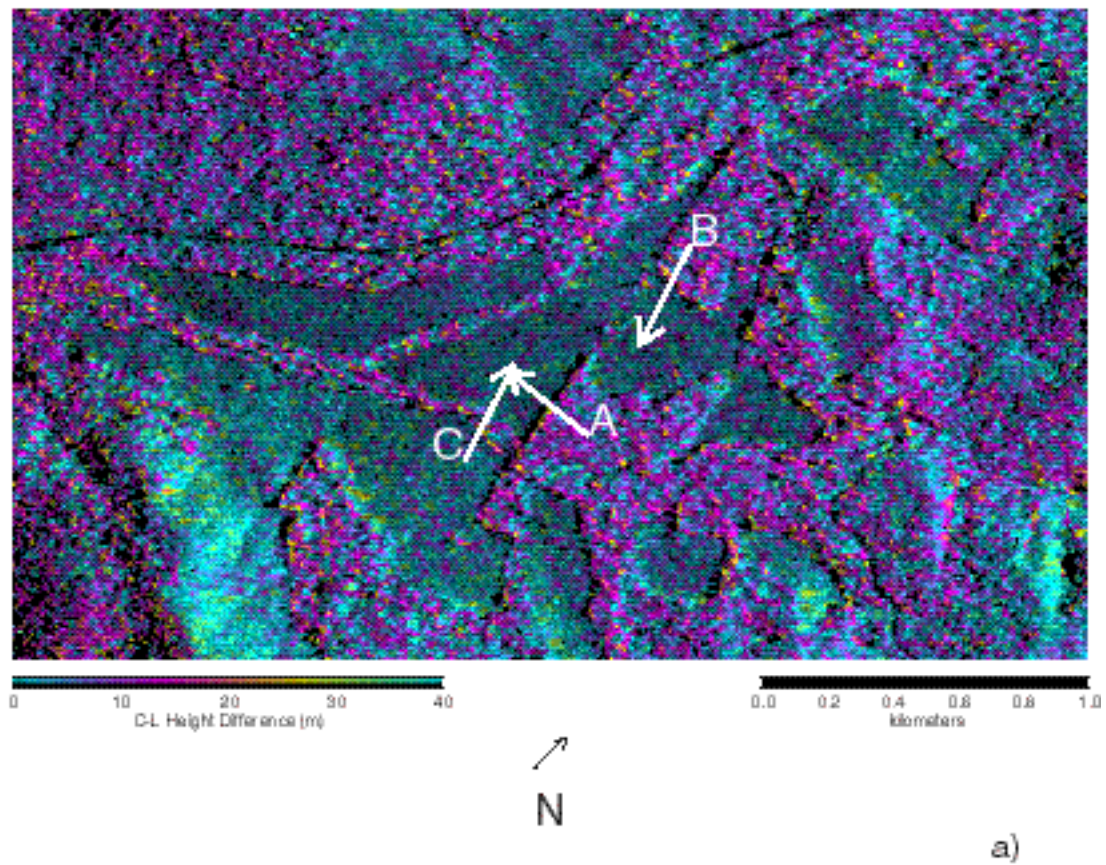


Figure 25: a) Image of height difference between C- and L-band in Iron Mountain, California. b) Profiles as indicated going from bare fields to forested regions.

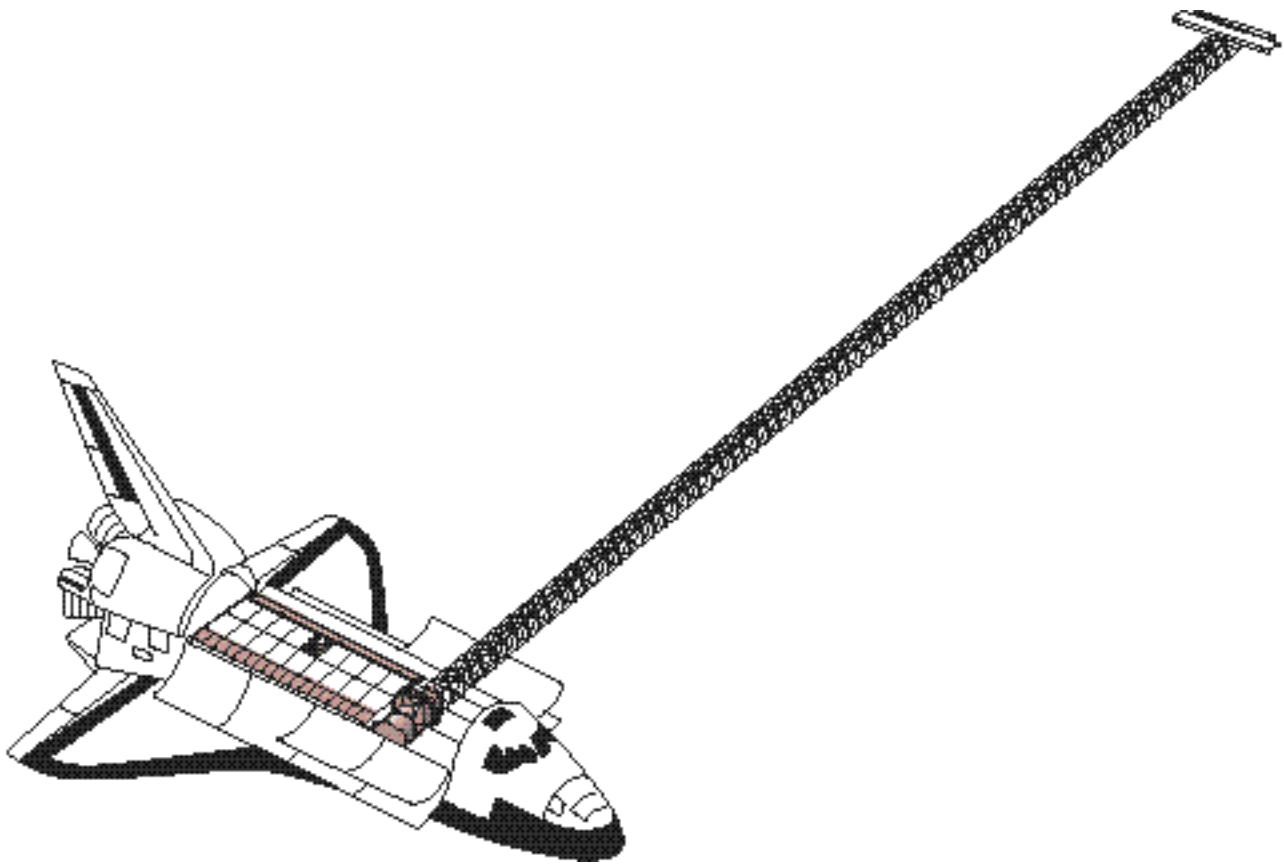


Figure 26: The Shuttle Radar Topography Mission flight system configuration. The SIR-C/X-SAR L, C, and X-band antennas reside in the shuttle's cargo bay. The C and X band radar systems are augmented by receive-only antennas deployed at the end of a 60 m long boom. Interferometric baseline length and attitude measurement devices are mounted on a plate attached to the main L-band antenna structure. During mapping operations, the shuttle is oriented to that the boom is 45 degrees from the horizontal.

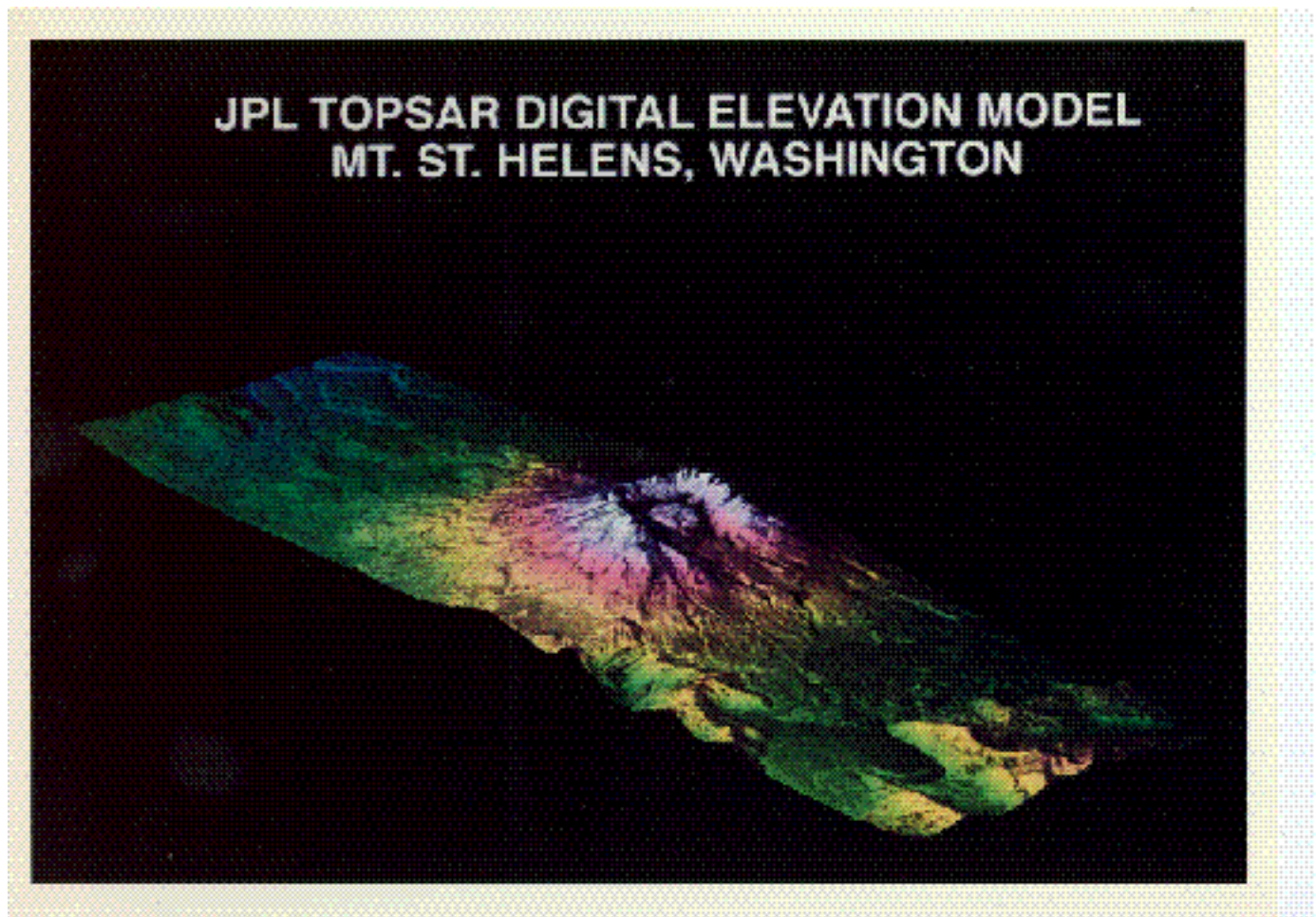


Figure 27: DEM of Mount Saint Helens generated in 1992 with the TOPSAR C-band interferometer. Area covered is roughly 6 km across track by 20 km along track.

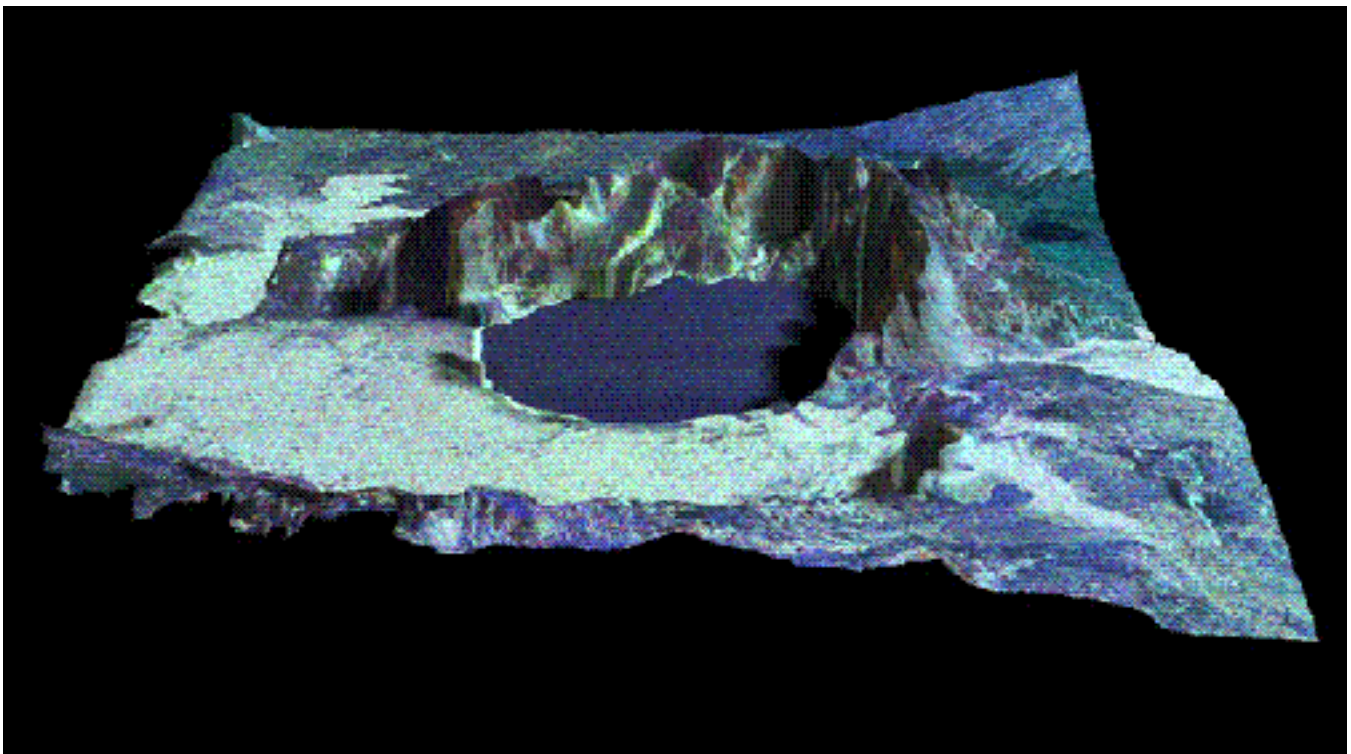


Figure 28: DEM of Askja, Northern volcanic zone, Iceland derived from the C-band EMISAR topographic mapping system. The color variation in the image is derived from L-band EMISAR polarimetry.

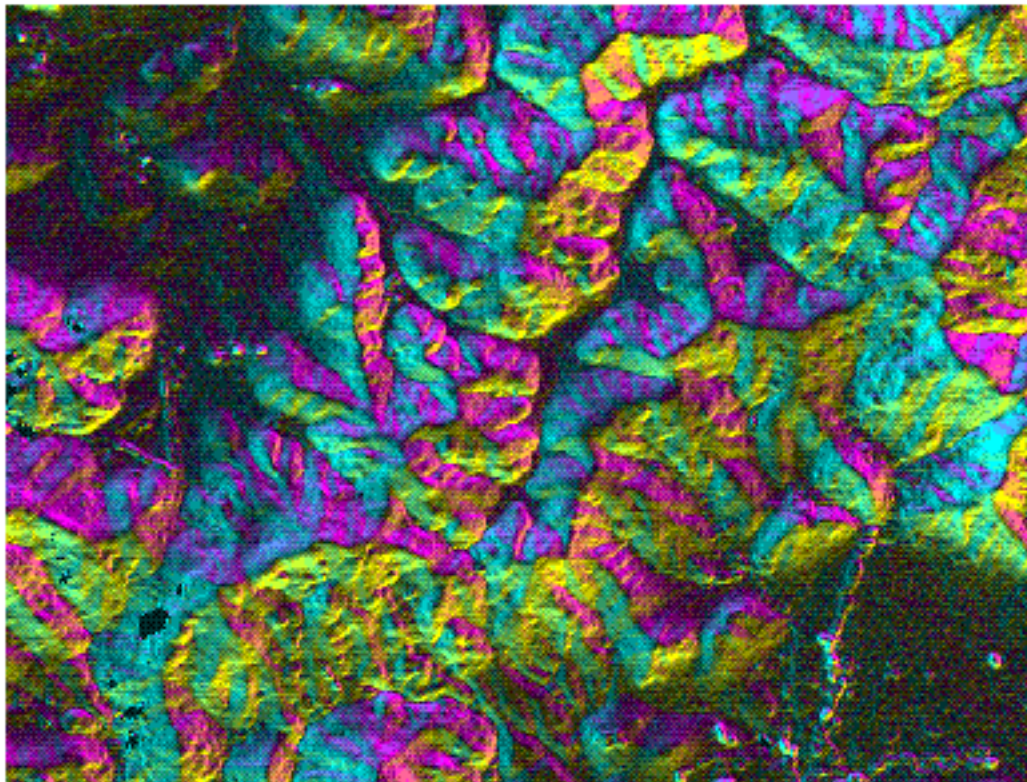
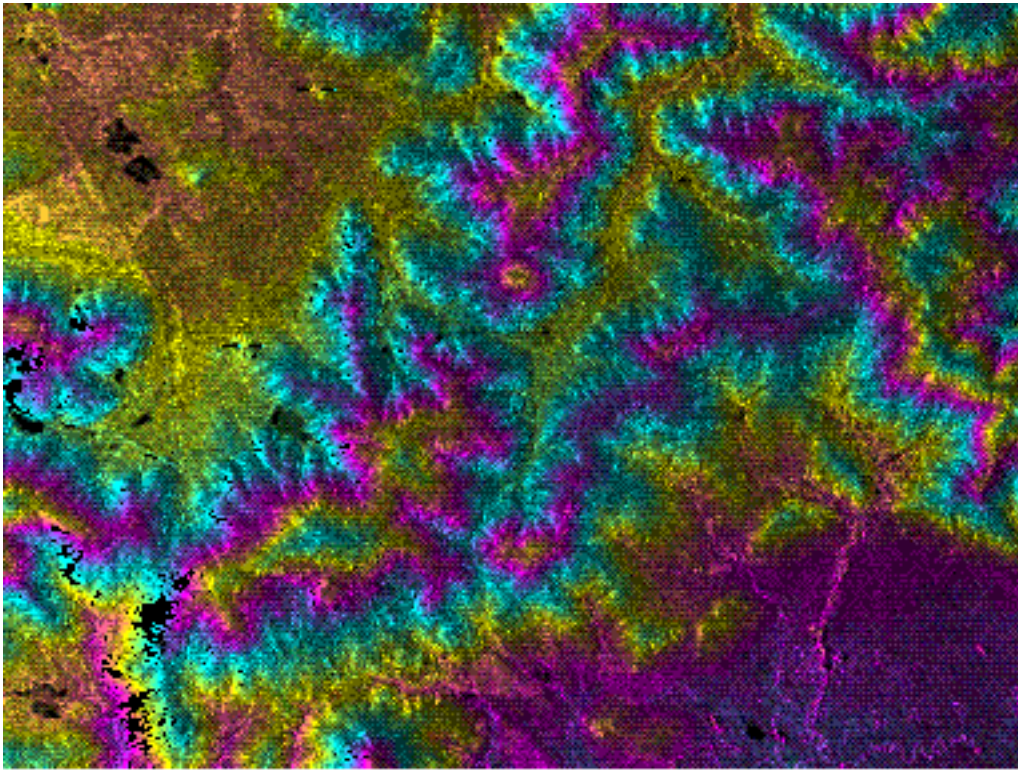


Figure 29: Height (above) and slope (below) maps of Mount Sonoma, CA. This information has been used to assess the risk of earthquake damage induced by landslides. Processing courtesy E. Chapin, JPL.

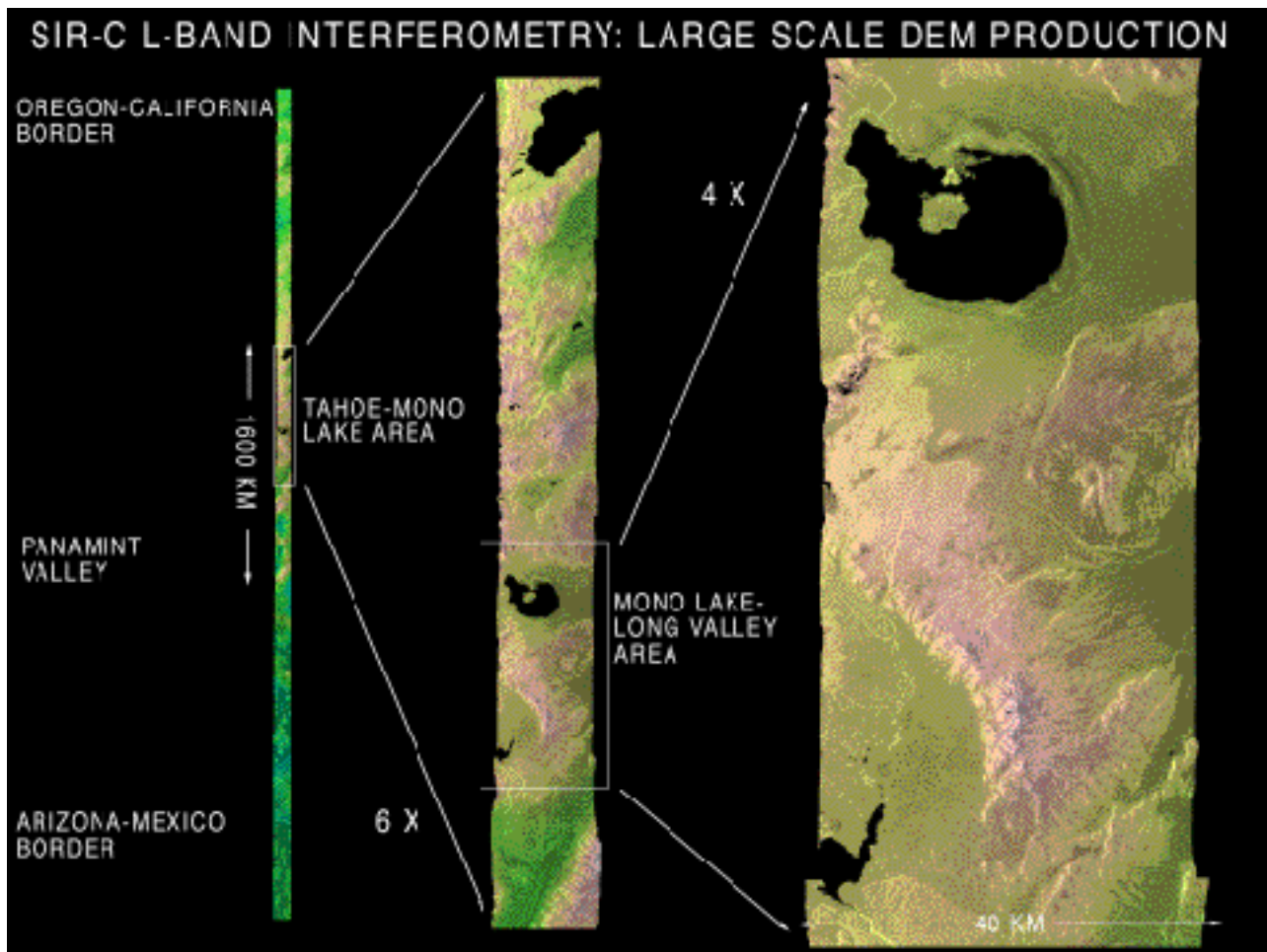


Figure 30: Strip of Topography generated from the SIR-C L-band radar data by repeat track interferometry. The DEM extends from the Oregon/California border through California to Mexico, roughly 1600 km.

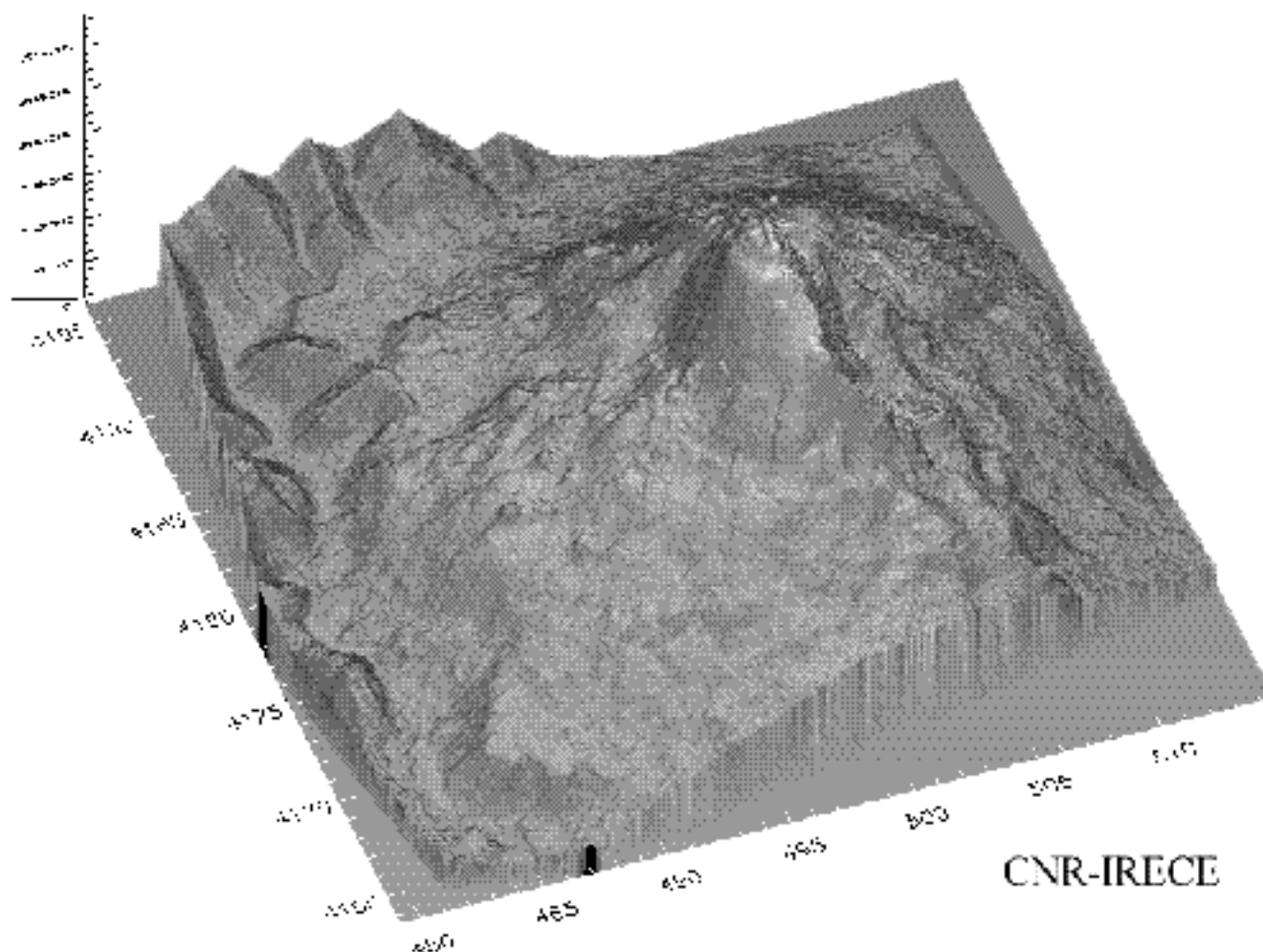


Figure 31: DEM of Mount Etna, Italy generated by ERS repeat track interferometry. Actually 10 images were combined to make this DEM.

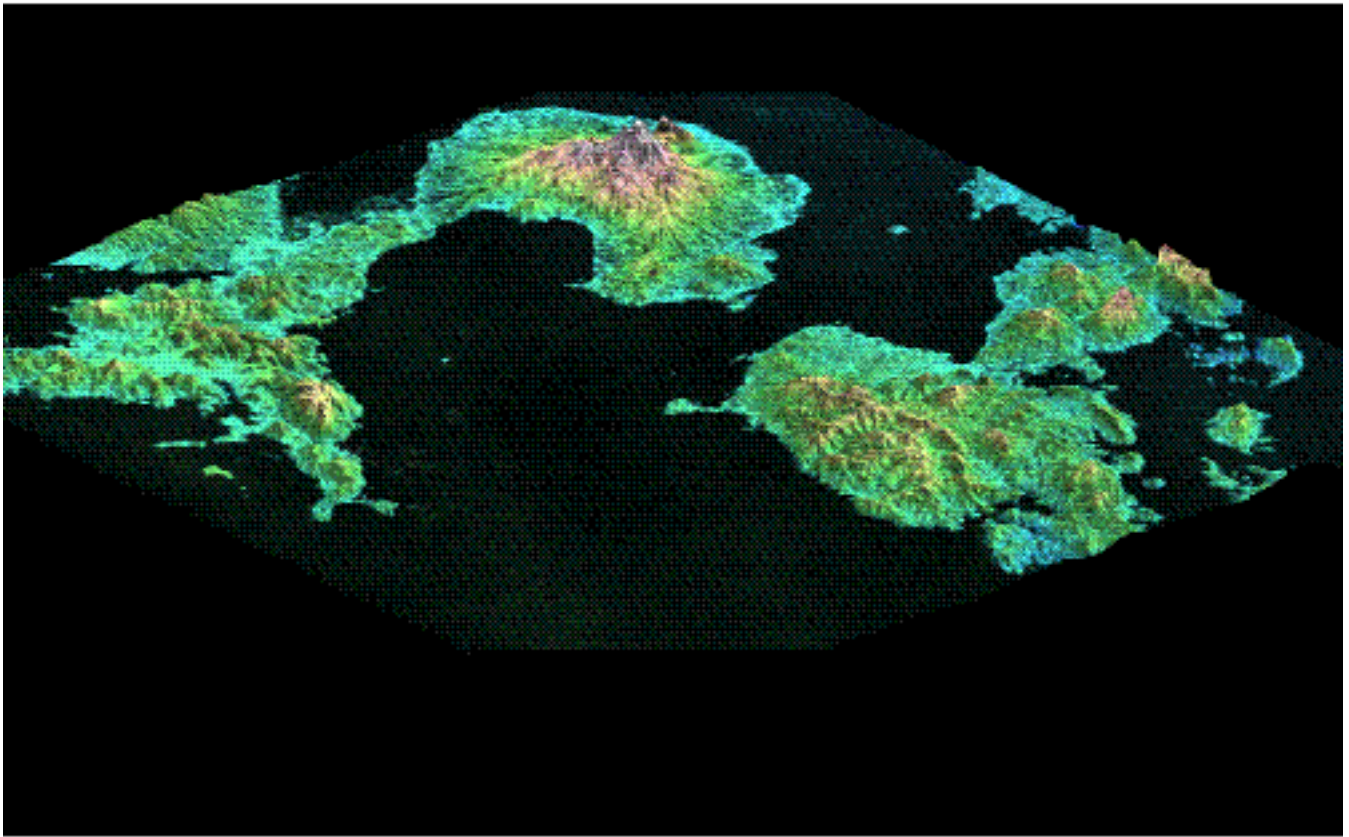


Figure 32: DEM of Mount Unzen, Japan generated by JERS repeat track interferometry.

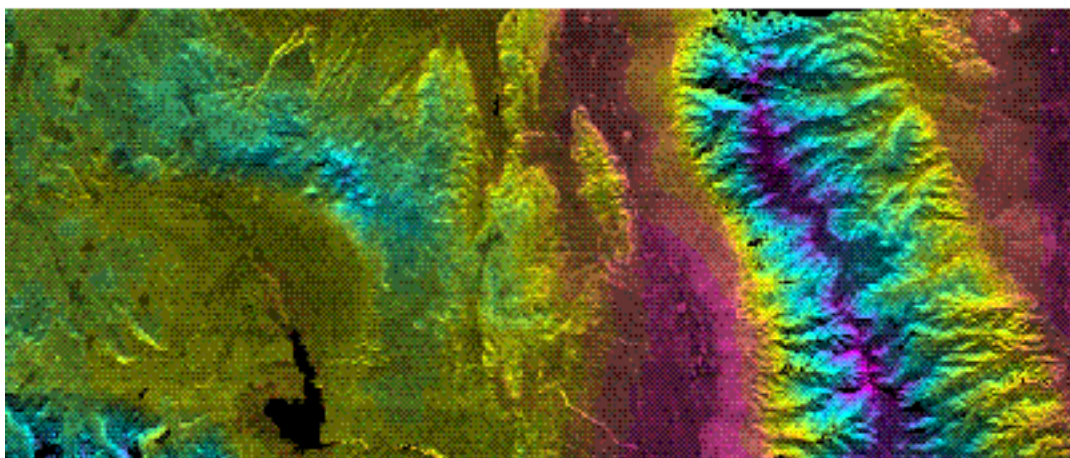


Figure 33: Long Valley mosaic of TOPSAR C-band interferometric data. Processing courtesy E. Chapin, JPL.

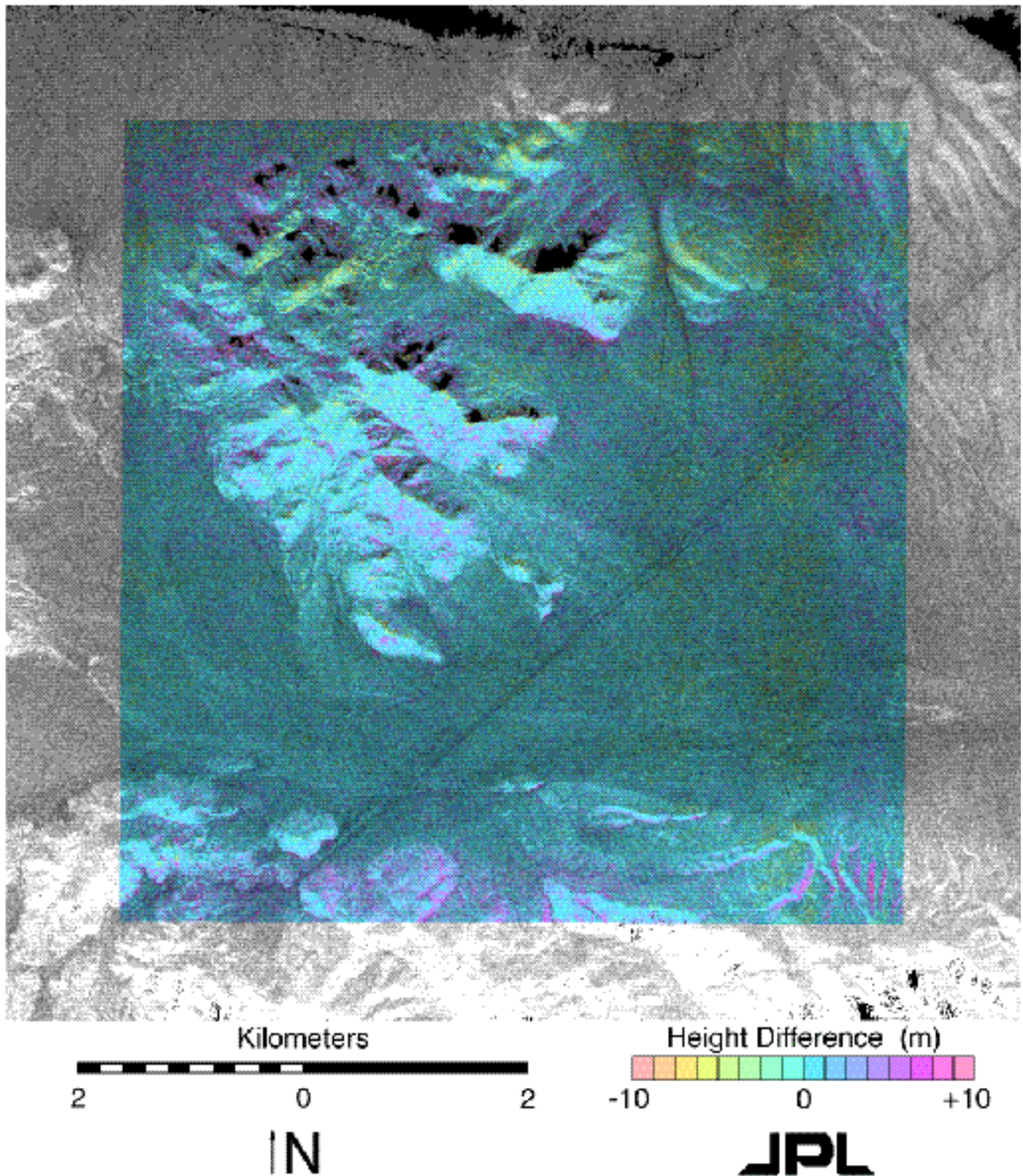


Figure 34: Difference image between TOPSAR C-band derived DEM and a TEC photogrammetrically-generated reference DEM.

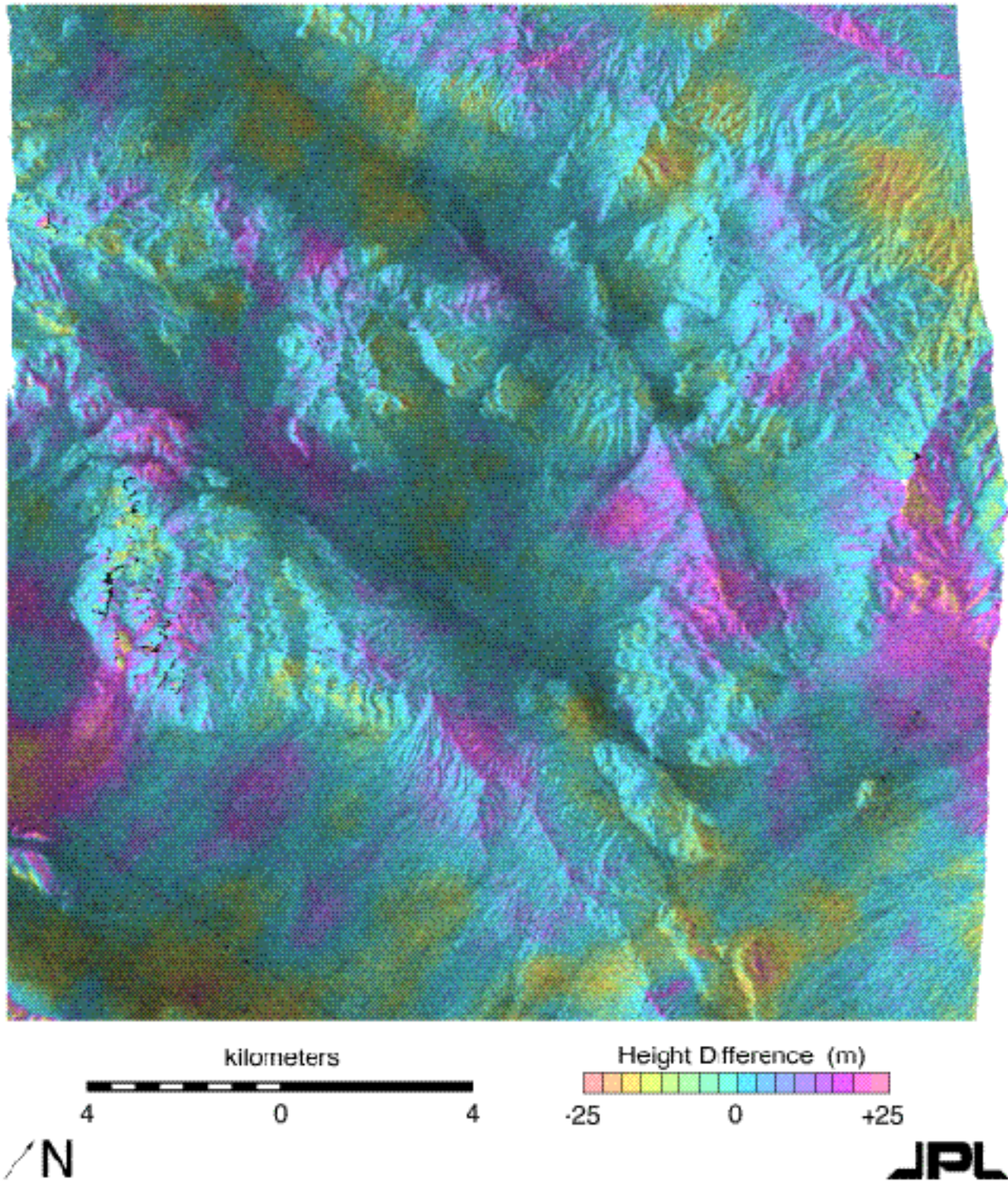


Figure 35: Difference image between SIR-C C-band derived DEM and a TOPSAR C-band mosaic used as a reference DEM.

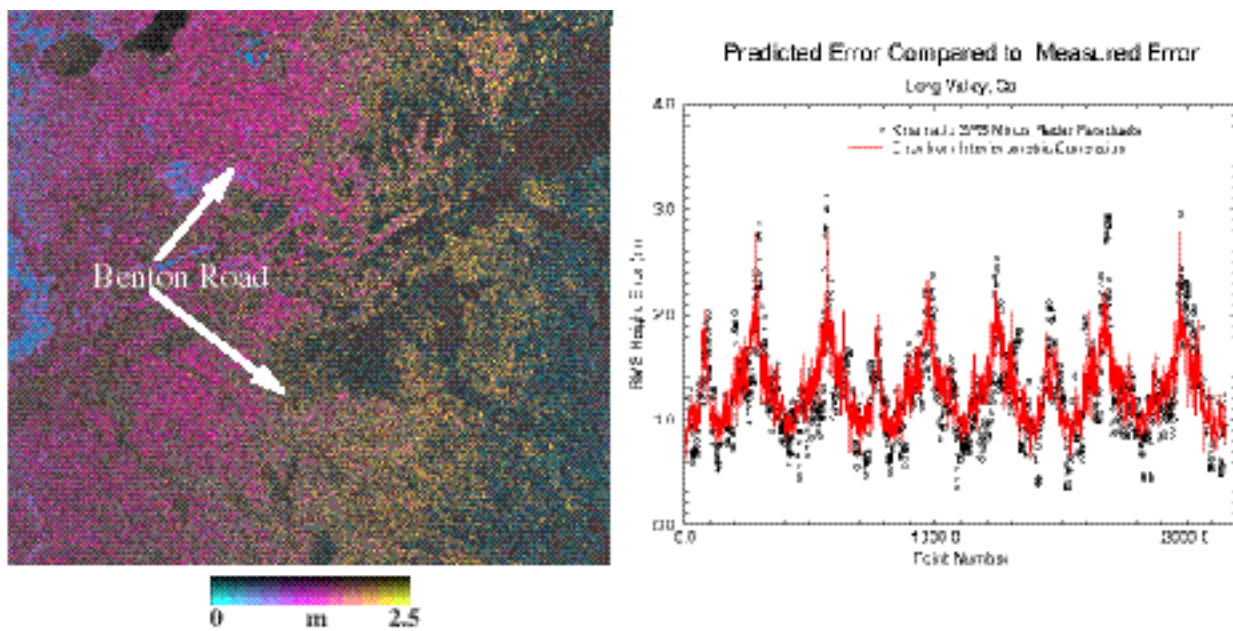


Figure 36: Illustration of the use of kinematic GPS surveys in determining the absolute and relative error of a radar-derived DEM. Curve shows the standard deviation of the radar height relative to the GPS, and its predicted value. Statistical height error estimates derived from the correlation track the measured local statistical height errors extremely well [81].

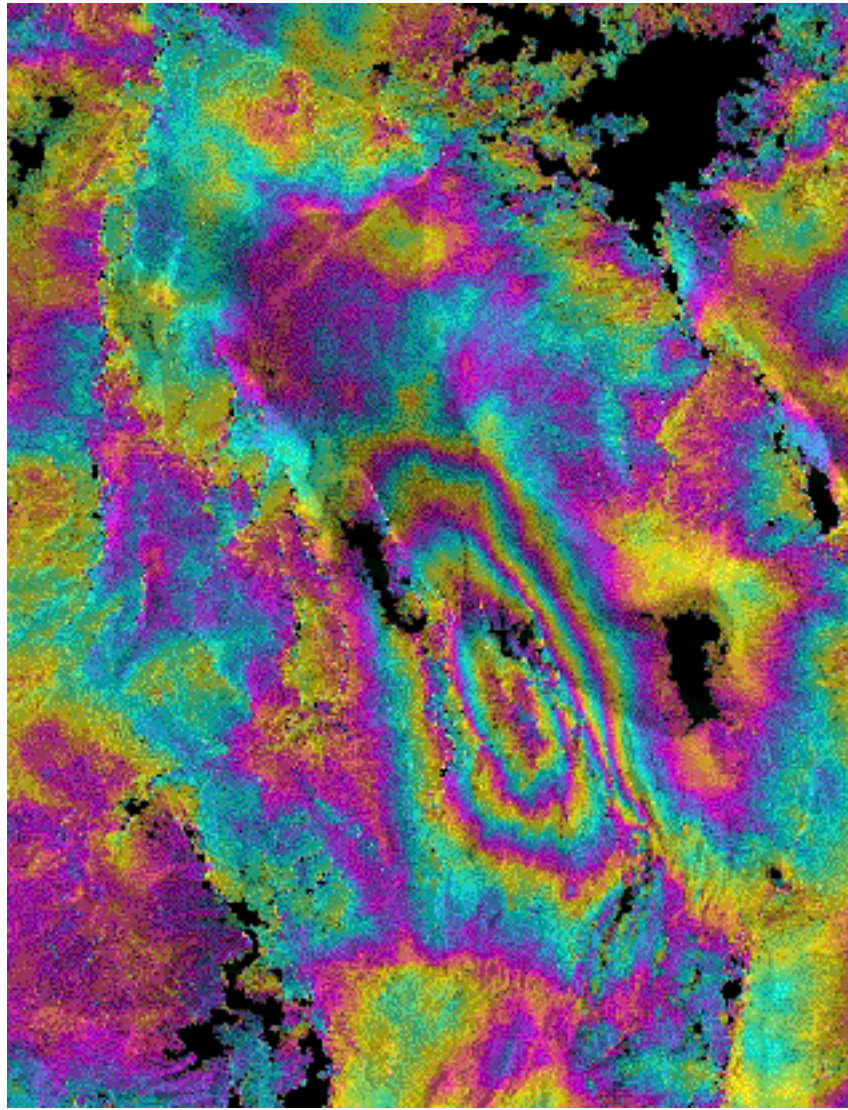


Figure 37: Subsidence caused to an $M=6.3$ earthquake along a normal fault in Eureka Valley, California imaged interferometrically by ERS-1. The interferometric signature combined with the seismic record suggested an interpretation of variable slip along the fault. Figure courtesy of Gilles Peltzer, JPL.

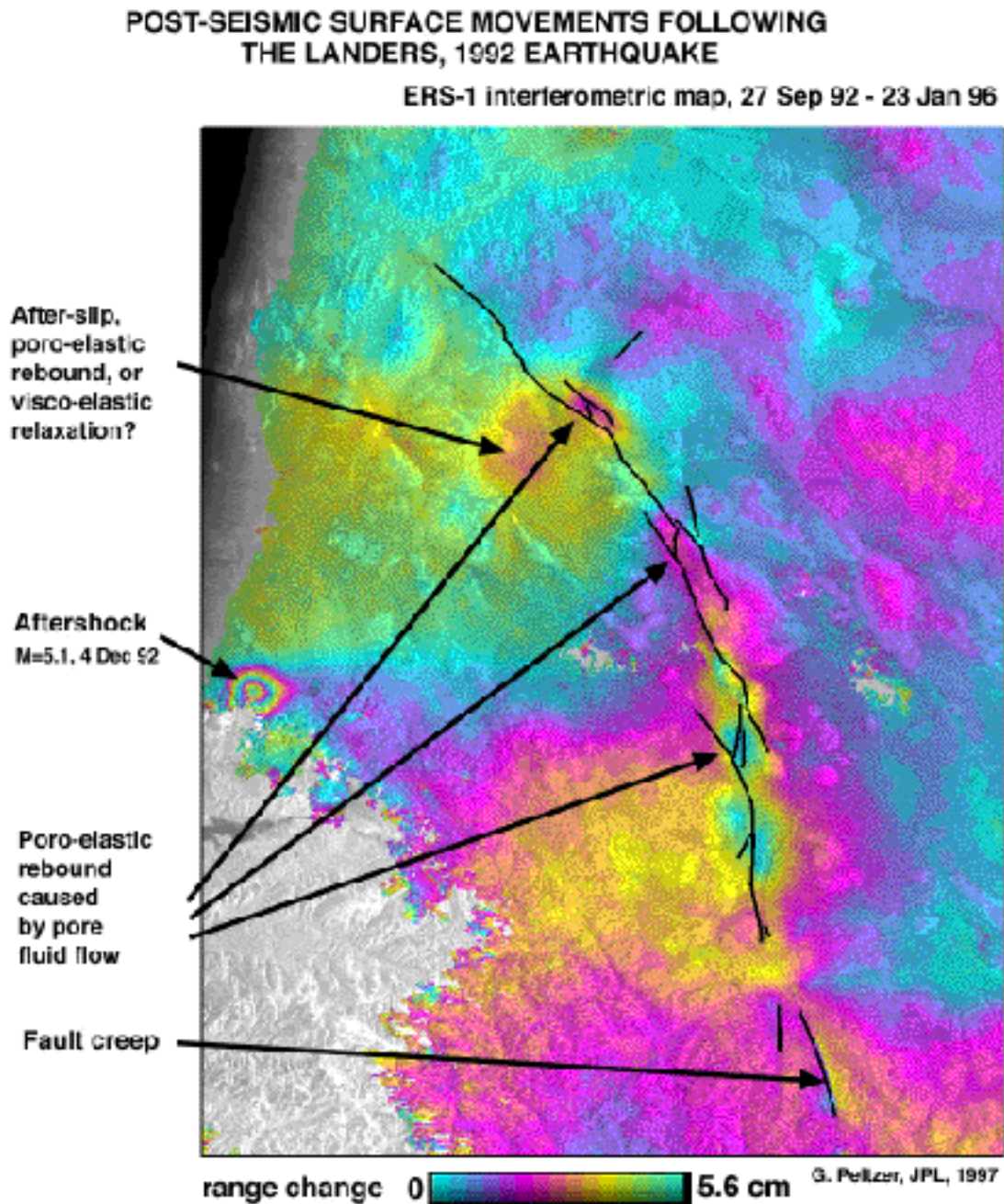


Figure 38: Illustration of post-seismic deformation following the M=7.2 Landers earthquake in 1992. In addition to the deformation features described in the text that are well-modeled by poro-elastic flow in the pull aparts, several other deformation processes can be seen. Figure courtesy of Gilles Peltzer, JPL.

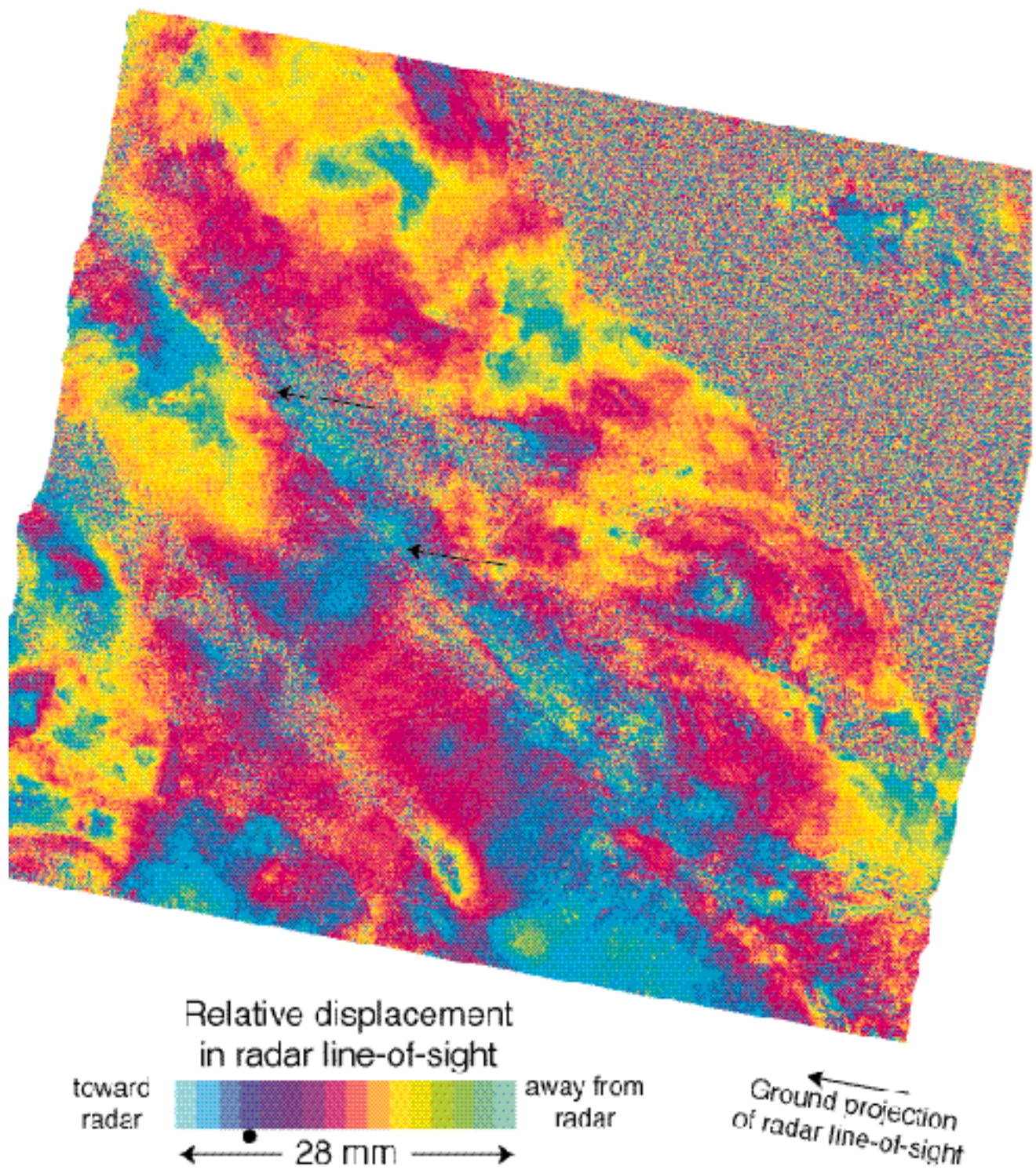


Figure 39: Aseismic slip along the San Andreas Fault near Parkfield, California, imaged interferometrically by ERS-1.

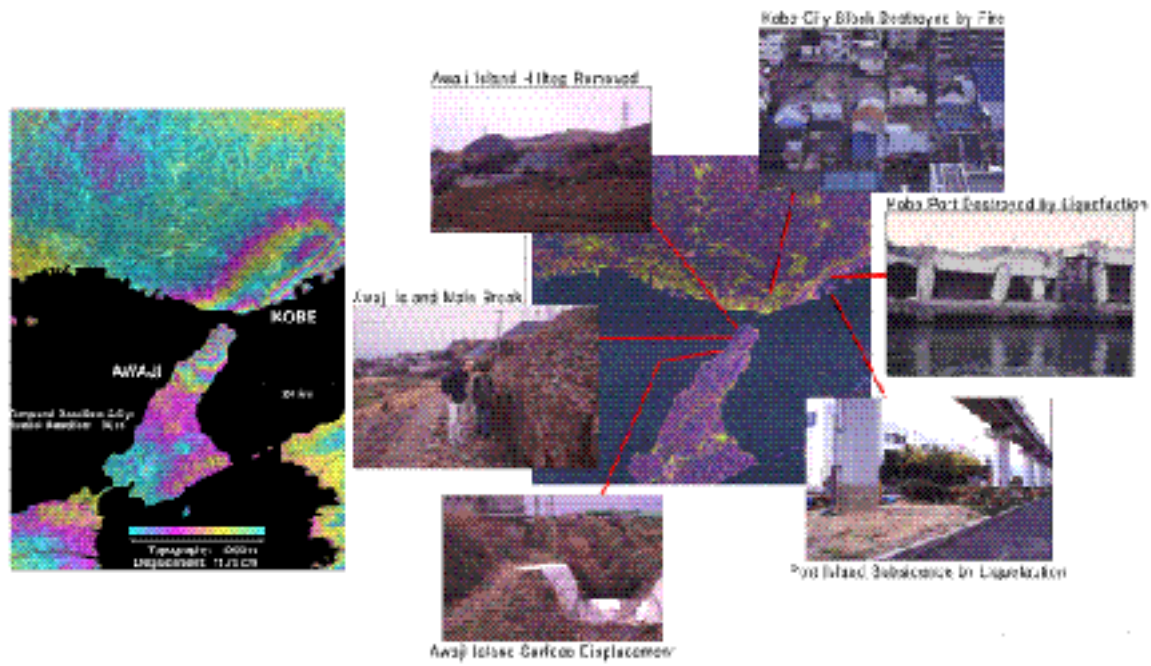


Figure 40: Decorrelation in the destroyed areas of Kobe city due to the 1995 M=6.8 earthquake. Areas where structures were firmly connected to bedrock remained correlated, while structures on sandy areas of liquefaction were destroyed and decorrelated in the imagery.

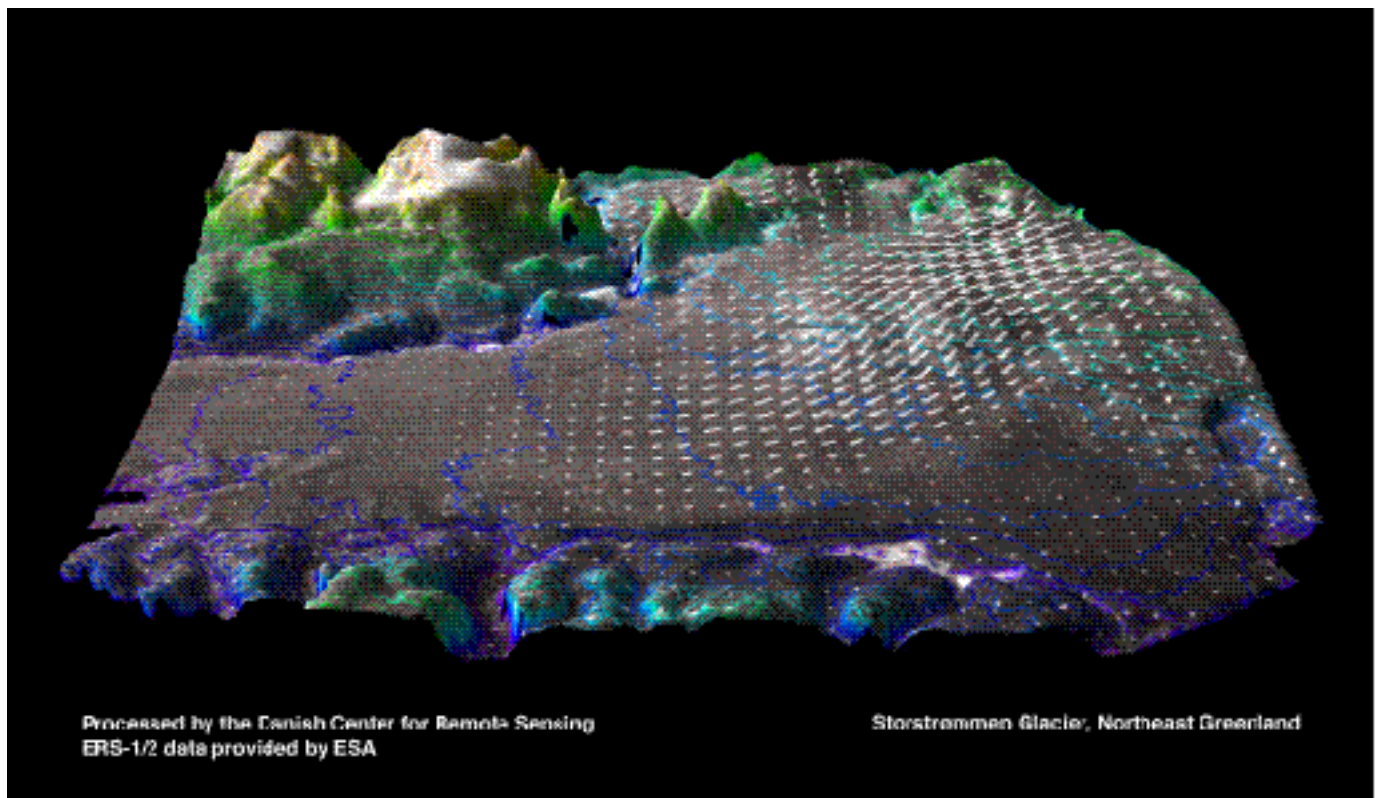


Figure 41: Ice velocity map draped on topography of Storstrømmen Glacier in Greenland. Both velocity and topography were generated by ERS interferometry. Ice velocity vectors show that the outlet of the glacier is blocked from flow [126]. In addition to aiding visualization of the ice flow, topographic maps such as this are an important measurement constraint on the mass balance, as changes in topographic height relate to the flow rate of ice from the glacier to the sea.

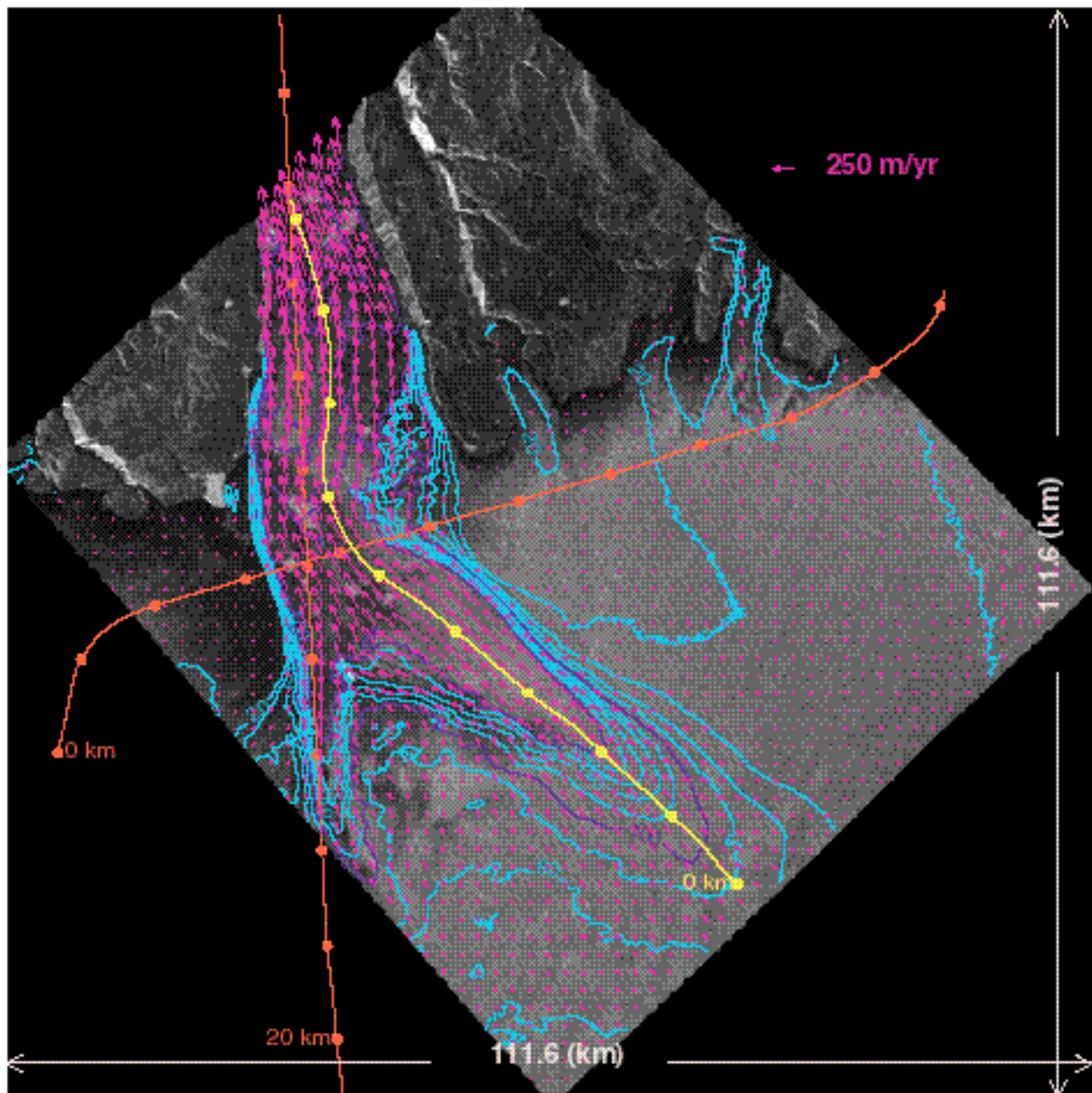


Figure 42: Horizontal velocity field plotted over the SAR amplitude image of the Ryder Glacier. Contour interval is 20 m/yr (cyan) for velocity less than 200 m/yr and is 100 m/yr (blue) for values greater than 200 m/yr. Red arrows indicate flow direction and have length proportional to speed.

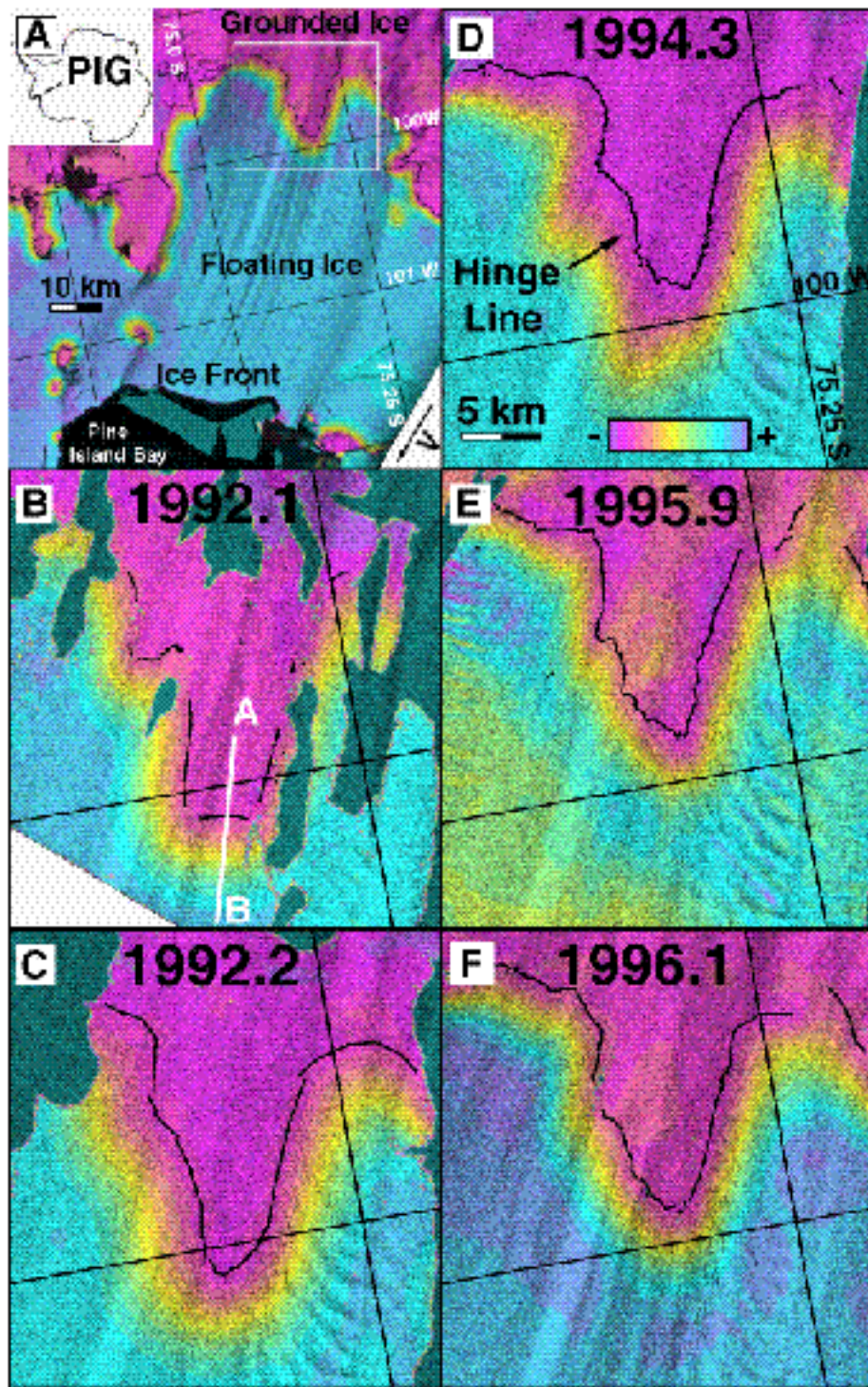


Figure 43: Grounding line time series (Courtesy: E. Rignot; Copyright *Science*), illustrating the retreat of Pine Island Glacier.

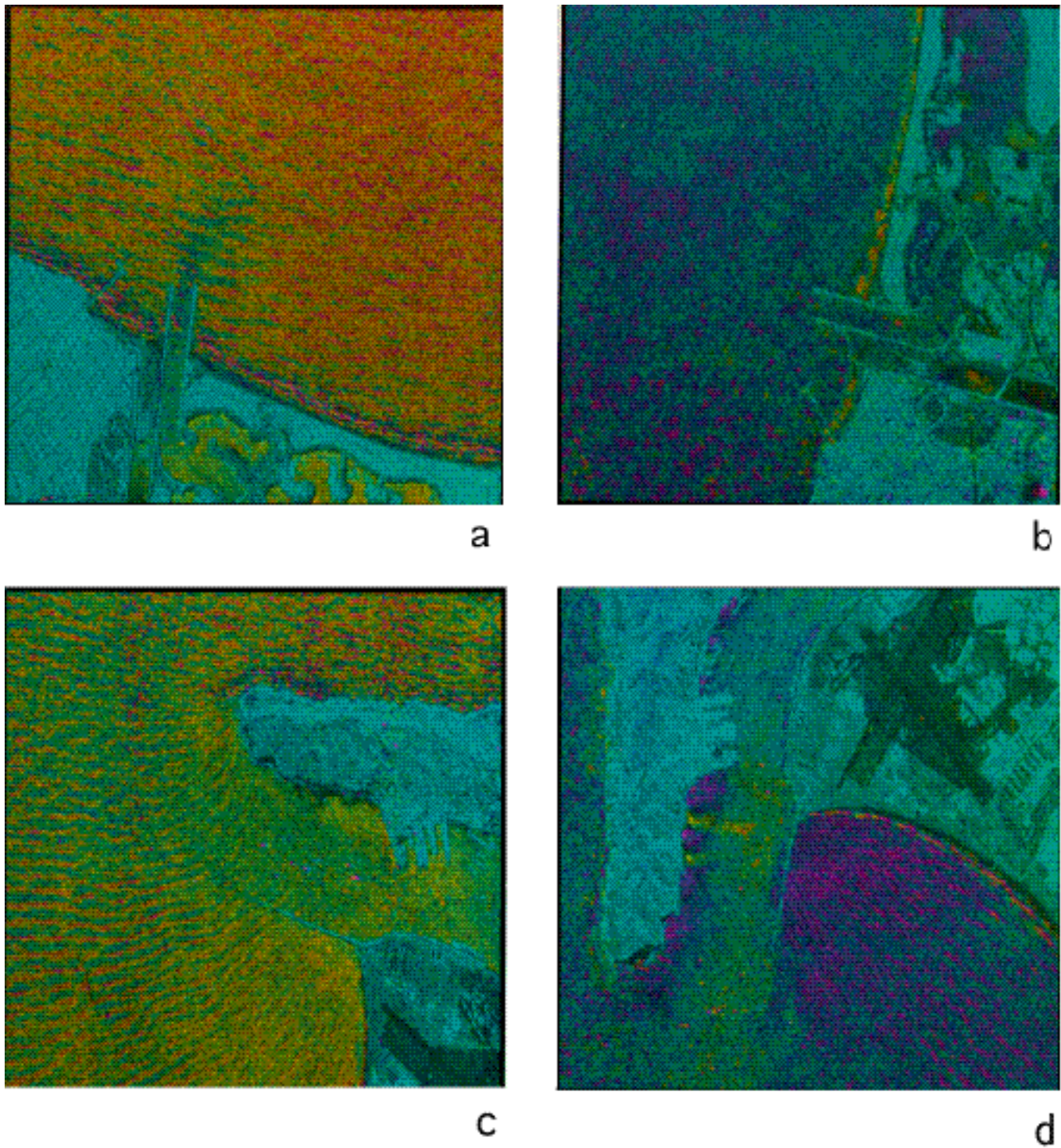


Figure 44: Example of ocean currents measured by along-track SAR interferometry at Mission Bay, San Diego, CA. Flight direction of the radar is from left to right in each image, so panels a-d show different look aspects of the wave patterns propagating to shore.

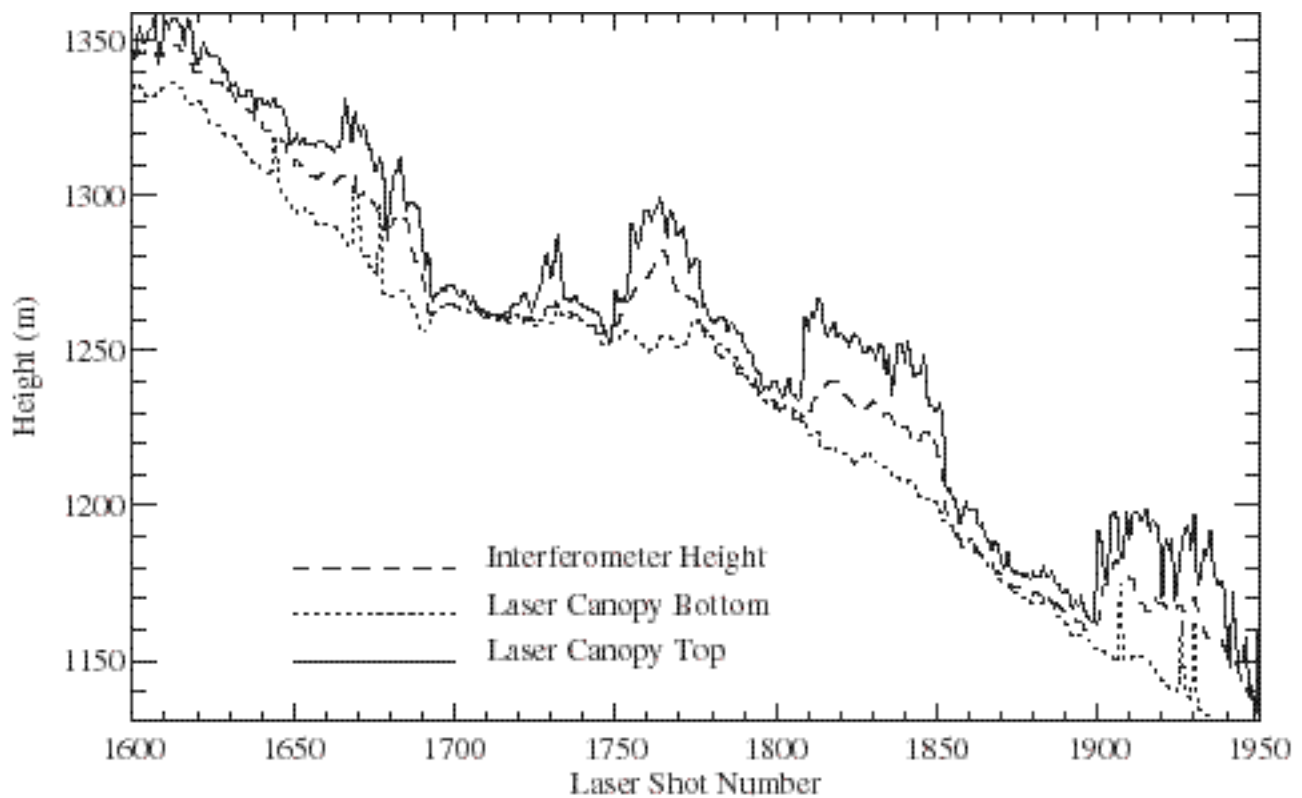


Figure 45: Profiles of canopy extent as measured by the Goddard Space Flight Center Airborne Laser Altimeter, compared with JPL TOPSAR (C-band) elevation estimates along the same profiles. A clear distinction is seen between the laser-derived canopy extents and the interferometer height, which generally lies midway in the canopy, but varies depending on canopy thickness and gap structure.

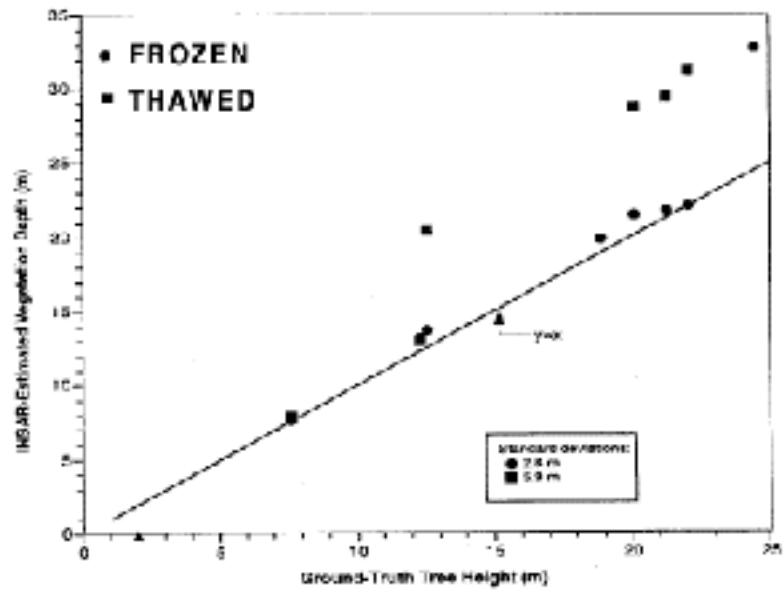


Figure 46: Inversion of interferometric data from JPL TOPSAR for tree height. After Treuhaft, 1997.

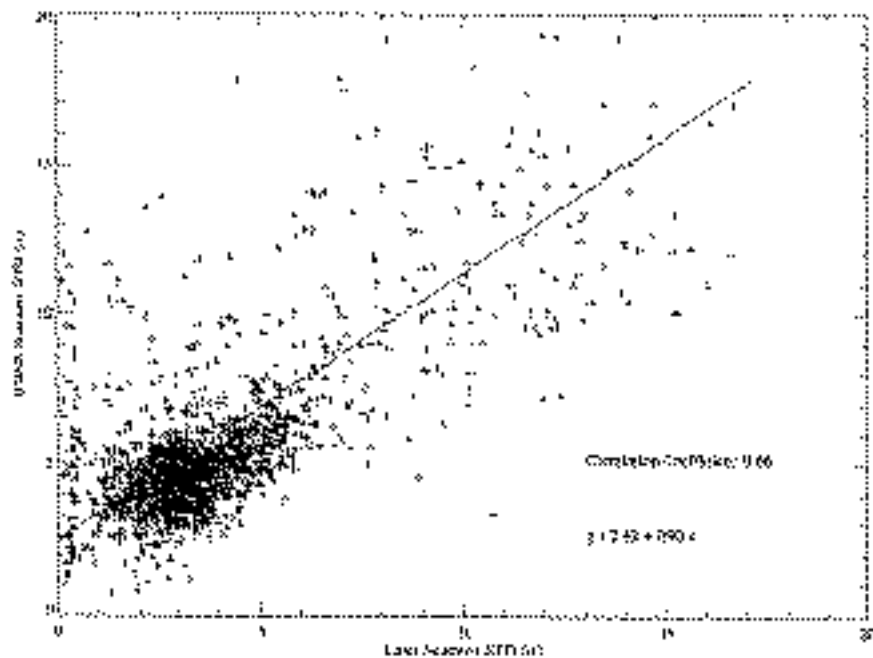


Figure 47: Estimated scatterer standard deviation compared to tree height deviation derived by laser altimeter. Scatter plot shows relatively modest correlation, an indication of the limited ability to discriminate the volumetric decorrelation term from other decorrelation effects, such as thermal, processor, and ambiguity noise. Many of these limitations can be controlled by proper system design.

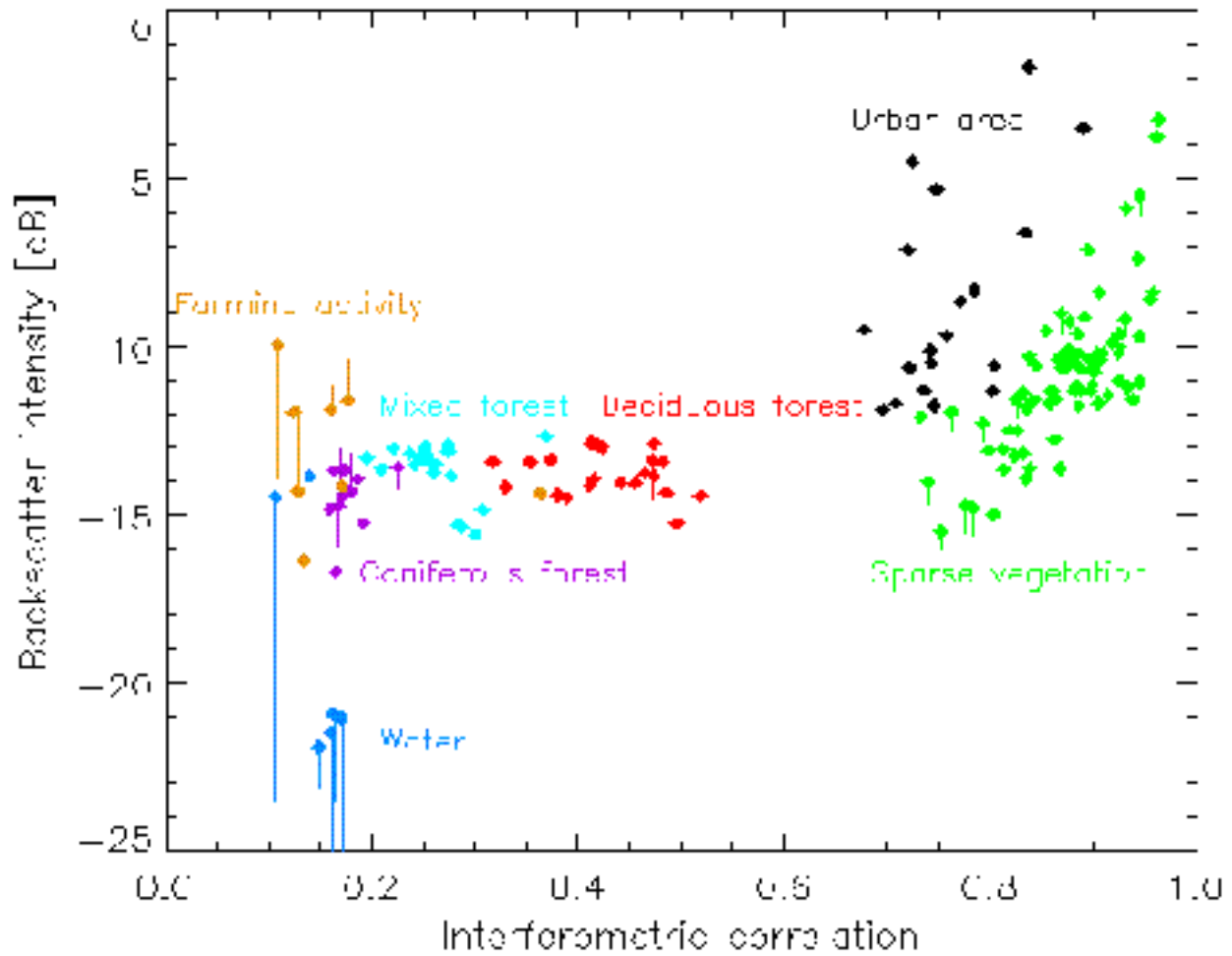


Figure 48: Classification space showing image brightness vs. interferometric correlation. Terrain types cluster as indicated.

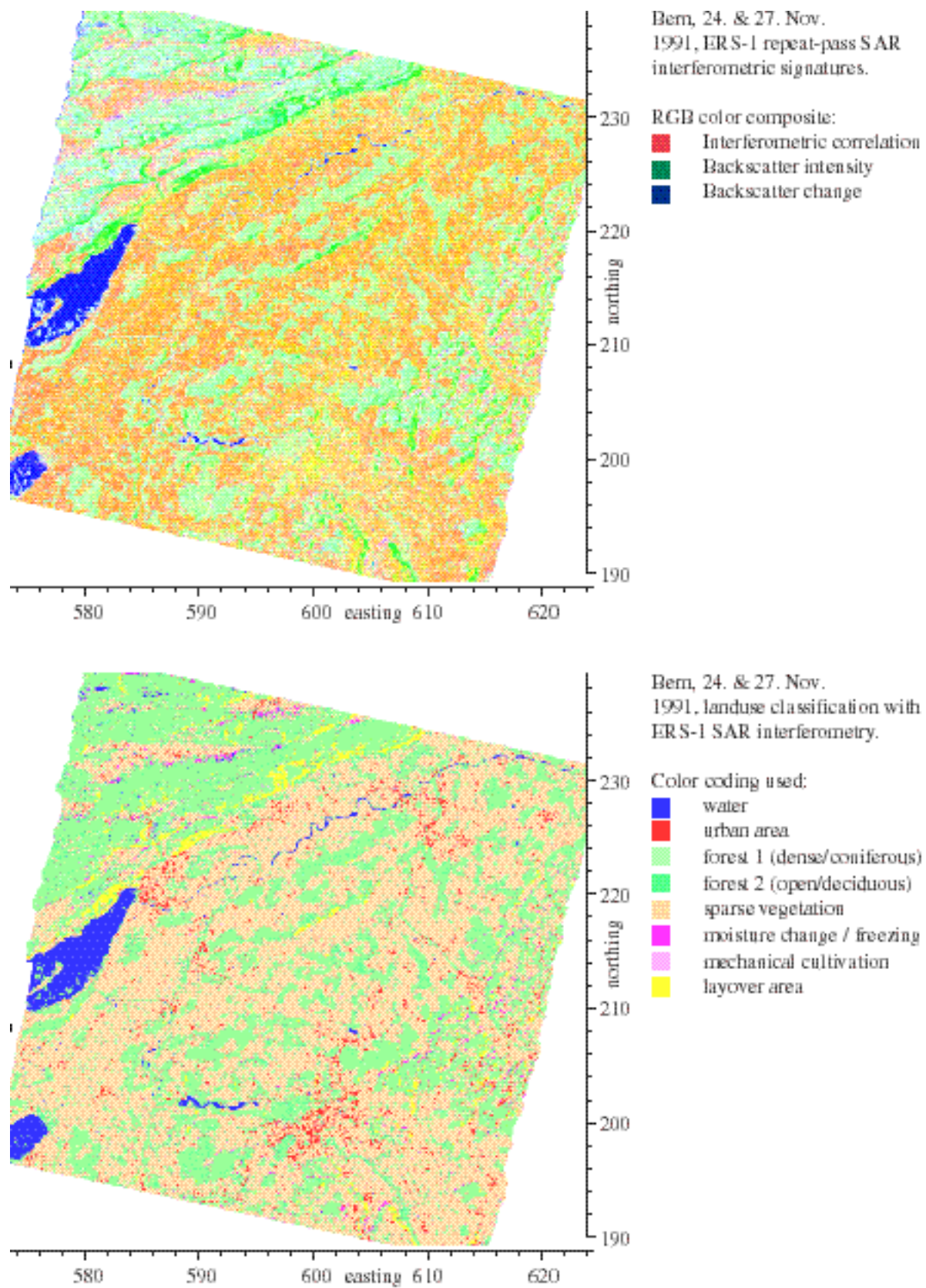


Figure 49: Classification of Bern, Switzerland using ERS interferometric time series data to distinguish features.

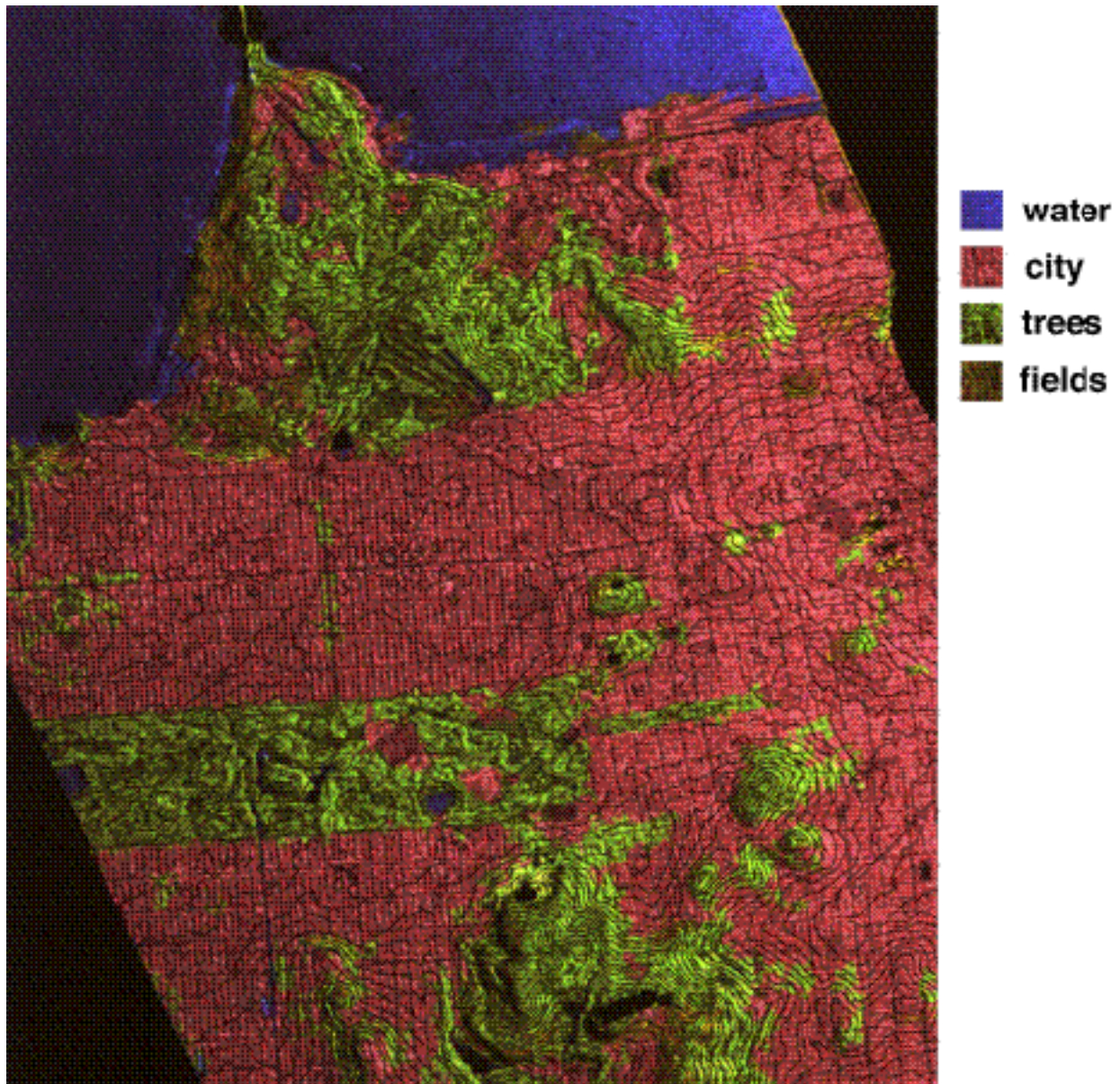


Figure 50: Classification of San Francisco using JPL TOPSAR (C-band) image brightness, interferometric correlation, and topographic height and slope.

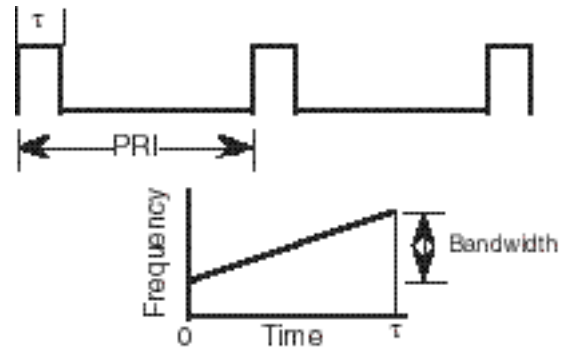


Figure 51: The radar emits a sequence of pulses separated in time. The time duration between pulses is called the inter pulse period (IPP) and the associated pulse frequency is called the pulse repetition frequency ($\text{PRF}=1/\text{IPP}$). The pulse duration is denoted τ .

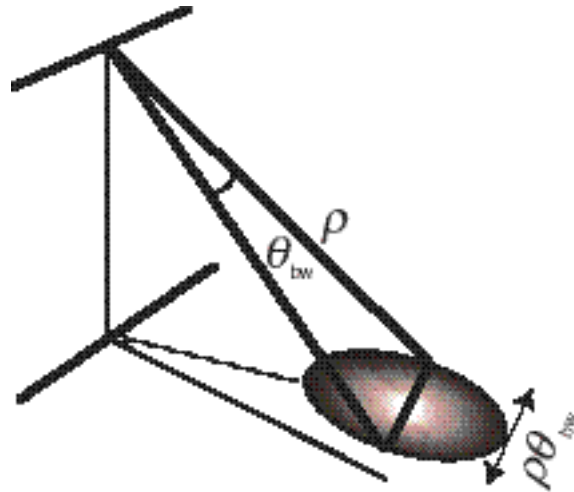


Figure 52: The antenna footprint size in the azimuth direction depends on the range and the antenna beamwidth in the azimuth direction. Figure shows forward-squinted beam footprint.

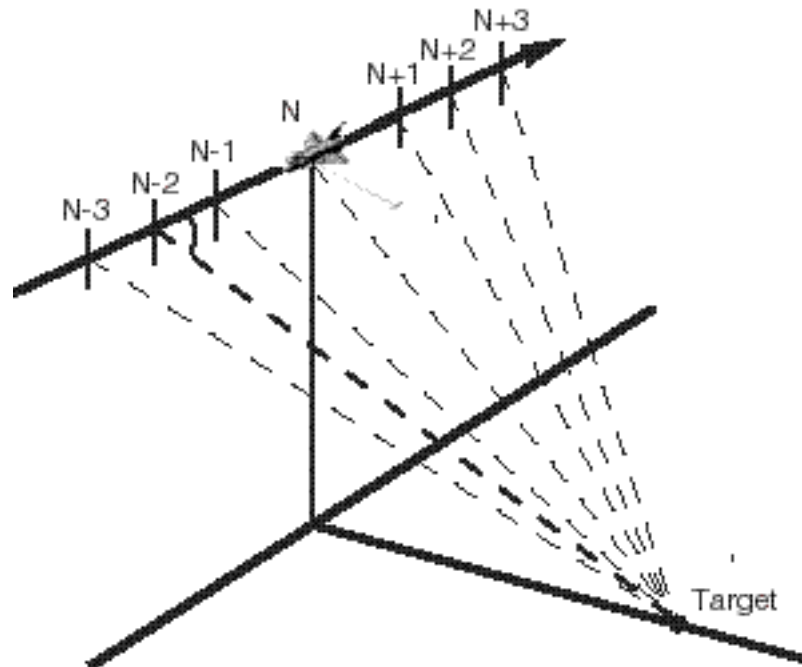


Figure 53: A sensor imaging a fixed point on the ground from a number of pulses in a synthetic aperture. The range at which a target appears in an synthetic aperture image depends on the processing parameters and algorithm used to generate the image. For standard range/Doppler processing the range is fixed by choosing the pulse which has a user defined fixed angle between the velocity vector and the line-of-sight vector to the target. This is equivalent to picking the Doppler frequency.